The Galactic Population of Low Mass X-ray Binaries in the Era of Large Sky Surveys

Yuankun Wang

A dissertation
submitted in partial fulfillment of the
requirements for the degree of

Doctor of Philosophy

University of Washington

2026

Reading Committee:

Eric Bellm, Chair

James Davenport

Zeljko Ivezić

Program Authorized to Offer Degree:
Astronomy

University of Washington

Abstract

The Galactic Population of Low Mass X-ray Binaries in the Era of Large Sky Surveys

Yuankun Wang

Chair of the Supervisory Committee:
Professor Eric Bellm
Astronomy

Low mass X-ray binaries (LMXBs) are systems where a star with mass $< 2M_\odot$ orbits either a neutron star (NS) or black hole (BH) so closely that mass transfer occurs due to Roche lobe overflow (RLOF). Many of these systems exhibit recurring phases of extremely bright outbursts that peak at X-ray wavelengths, followed by long periods of quiescence. While our current known population of these objects totals only a few hundred, explaining the observed features of the population of LMXBs requires understanding of binary stellar evolution, compact object formation, and accretion physics. Therefore increasing this population, potentially by complementary discovery pathways that have different biases than current X-ray driven methods, could have a significant impact on our understanding of these disparate areas of astrophysics.

In this dissertation, I describe my study of LMXBs from both an observational and theoretical perspective, and look ahead to a new era when the Vera Rubin Observatory's Legacy Survey of Space and Time (LSST) will transform optical time domain astronomy. In Chapter 2, I describe a search for optical outbursts of LMXBs in the Zwicky Transient Facility (ZTF) alert stream and use a small sample of discovered outbursts to make inferences about the galactic LMXB population, as well as future prospects for a similar search in LSST. In Chapter 3, I use `cogsworth` to simulate a population of LMXBs and compare their observable properties to our currently known population to learn about binary stellar evolution models. In Chapter 4, I present an exploratory crossmatch between the Rubin Data Preview 1 (DP1),

the first publicly available data released by the Vera Rubin Observatory, and describe some challenges for making the multiwavelength associations that are crucial for classifying X-ray emitting sources like LMXBs. In Chapter 5, I summarize the work completed and its place in the context of the start of LSST.

DEDICATION

To my wife Caroline: thank you for your support and for your unwavering belief in me. To dad, who also dedicated his thesis to me, and mom, who gave up her studies to bring me into this country. To my brother John, so he doesn't feel left out.

ACKNOWLEDGMENTS

While this document is the product of my 6 years of research at the University of Washington, it is also the culmination of the efforts of countless people who have supported, assisted, and otherwise influenced me along my entire educational journey. I am deeply grateful to many people, a subset of whom are named below.

I want to thank my advisor Eric Bellm for his mentorship and guidance in all of my projects, for being patient as each project evolved away from our initial expectations, and for securing grants so that I never had to spend any time or resources worrying about funding. I'd like to additionally thank my committee Jim Davenport and Zeljko Ivezic: Jim for always being open to talking time-domain astronomy, and Zeljko for his enthusiastic support every time I see him. I also extend my thanks to Tom Wagg for being my primary mentor for Chapter 3 of my thesis, and whose leftover funding covered two quarters in my final year, and also to Erin Howard for single handedly teaching me how to run and navigate the Rubin data pipelines.

During my time at the University of Washington, I had the privilege of serving in many non-academic roles. I am particularly grateful to have had the opportunity to teach PreMAP, and to the students in cohort 19, whose excitement and earnestness to learn was an inspiration, and I appreciate Jess Werk and Rudy Garcia for taking time to share their thoughts and expertise in teaching, which made me a much better instructor. I also want to express my gratitude to Elisa Quintana and Paula Newcomer for their indispensable help when planning the grad visits, and to Liza Young and Tyneshia Valdez for all the time they spent making things easier for the grad students. Thanks also to all the administrative staff in the Department of Astronomy for all their essential work, which makes the academic work possible.

I'm also grateful to all my scientific and academic mentors and role models who shaped my path on the way to a graduate degree, including Mr. Plunkett, Ms. Duncan, and Mr. Wandell who encouraged my interests in math, science, and the humanities. This also includes my undergraduate advisors and instructors, in particular Gregg Hallinan, Marin Anderson, Scott Ransom, and Frank Rice.

Rewinding back to the very beginning, I'd like to thank my parents Shaopeng and Chinghong, who managed to both pursue PhDs while also raising a child, me. Thank you for instilling the value of education in me, and also for their reminders that academic success is only one aspect of a fulfilling life. I also thank you for your love and support, even for the decisions I made for my academic career that we did not see eye to eye on.

Thank you to my wife Caroline, who has been my constant partner companion and whose outside perspective has helped me contextualize my problems in grad school many times. Your unwavering support and belief in me means so much and I could not have done this without you. I would also like to thank the faith based communities we are part of for their support and prayers over the years.

The Eaton Fire, which burned through Altadena in January 2025 was hugely disruptive to my studies and I'm forever indebted to the people who reached out, supported, and were otherwise patient with me in the months following. Eric, Lupita, Gabby, Emmett, Anish, Sarthak, Shin, Frank, Cole, Evan, Amanda, Anand, Kai, and Rudy, I am eternally grateful for your support and assistance in getting though this very difficult time. A massive dis-acknowledgment to SoCal Edison for burning down my neighborhood.

Finally, I could not have gotten to this point without my friends and fellow graduate students, and I apologize for not naming everyone who has supported me with words or actions over the last 6 years. I want to thank the members of Eric's research group: Tom, Francisca, and especially Andy for their help and encouragement. Thanks also to Rudy, Jess, Andy, Gabby, v, and Tobin for their advice, kindness, and willingness to do things and go places with very short notice. Special thanks to my only cohort-mate Gabby for being there every step of the way and I regret I can't stay another year and graduate together!

This dissertation was completed on the lands of the Coast Salish people and the Duwamish Tribe. Parts of this work were also completed on the ancestral lands of the Gabrielino/Tongva peoples.

CONTENTS

CHAPTER 1

INTRODUCTION

1 Why LMXBs Matter?

Low mass X-ray binaries (LMXBs) are interacting binary systems in which a compact object, either a neutron star or a stellar mass black hole, accretes matter from a low mass companion star via Roche lobe overflow (Shakura & Sunyaev, 1973). As material is transferred onto an accretion disk around and ultimately onto the compact object, gravitational potential energy is released in the form of high energy radiation, often peaking at X-ray energies, making LMXBs among the brightest X-ray sources in the Galaxy (Remillard & McClintock, 2006). While they are a rare outcome of stellar evolution, understanding the formation and observational signature of LMXBs combines several areas of astrophysics, including compact object formation, binary stellar evolution, and accretion physics.

LMXBs are especially important for understanding the galactic population of compact objects, and in particular stellar mass black holes. Almost all of the stellar mass black holes that have been discovered in Milky Way were dynamically confirmed via observations of the donor star radial velocity measurements in quiescent LMXBs (Casares & Jonker, 2014; Corral-Santana et al., 2016). At the same time, this observed sample is subject to selection effects as it contains interacting systems that were bright enough to be discovered, usually during bright transient outbursts, and likely comprises a biased view of the full galactic black hole X-ray binary population. Our current known population of galactic black holes is only on the order of 100 objects, while the full predicted population using population synthesis is thought to total around $\sim 10^8$ objects (Wiktorowicz et al., 2019). As a result, while LMXBs serve as our best window into the population of galactic stellar mass black holes, the undetected population may be far larger and more diverse than the currently known sample suggests (Farr et al., 2011). Since the distributions of black holes (and neutron stars) inform our models for supernova remnant models and the late stage interior evolution of the progenitor, it is important to have an accurate understanding of the full population.

LMXBs are also essential to our observed neutron star population because they provide the canonical pathway for the formation of millisecond pulsars (MSPs) (Papitto & de Martino, 2022). In the standard recycling scenario, prolonged accretion from a low mass companion transfers angular momentum to an old neutron star, spinning it up to millisecond periods, which produces rapidly rotating MSPs (Bhattacharya & van den Heuvel, 1991). There is direct observational evidence for transitional millisecond pulsars (tMSPs) that switch between accretion powered and rotation powered states, highlighting LMXBs as a crucial link between accreting neutron stars and radio pulsars (Archibald et al., 2009; Papitto et al., 2013; Stappers et al., 2014).

LMXBs are also laboratories for studying and observing accretion physics. Many LMXB systems are transients that undergo dramatic outbursts where the luminosity can increase by orders of magnitude, separated by long intervals of quiescence. These state transitions provide some of the clearest observational tests of the disk instability model (Hameury, 2020, and references therein) and of the possible roles played by irradiation (Tetarenko et al., 2018), winds, (Neilsen & Degenaar, 2023; Tetarenko et al., 2018), viscosity (Hameury, 2020), disk truncation (Dubus et al., 2001), and mass-transfer variability in outburst behavior. Because LMXBs can be monitored in X-rays, optical light, and increasingly in the infrared (John et al., 2024), they offer a rich view of how accretion flows evolve in real time, including how disks brighten, how the heating front propagates, and how they sometimes fail to produce full outbursts (Alabarta et al., 2021).

Finally, LMXBs are valuable as tracers of binary stellar evolution and of galactic stellar populations. Their spatial distribution reflects the underlying old stellar population from which most low mass binaries arise, while their numbers, scale heights, and concentration toward the bulge or plane carry information about star-formation history, binary evolution, and compact object kicks (Repetto et al., 2017). As a result, LMXBs are not only interesting as individual systems, but also as a population that can be used to study the physics of how massive stars evolve in conjunction with companions This population perspective is becoming even more important in the era of wide-field time-domain surveys, which promise to uncover many more quiescent counterparts and optical outbursts, turning LMXBs into a tool for connecting compact binaries to binary stellar evolution. As these systems are also the progenitors to compact binary systems that are gravitation wave sources in LIGO and LISA (Wagg et al., 2022), X-ray binaries are useful for understanding the lifecycles needed to form double compact binaries (Postnov & Yungelson, 2014).

Studies of LMXBs can approach from an observational or theoretical framework, although each is not of course not exclusive of the other. From the observational side, we can discover and characterize systems, primarily through multiwavelength and time domain observations of their accretion driven outbursts, from which we can measure properties of the system such as compact object mass, orbital period, and time evolution of color/energy and luminosity, and aim to understand the underlying theory and physics of accretion. From the theoretical approach, we can use our understanding of binary stellar evolution to synthesize populations of LMXBs and compare them to our observed galactic population. We will study both approaches in the remainder of this manuscript.

2 LMXB Formation and Evolution

The standard formation channel for a low mass X-ray binary (LMXB) begins with an isolated binary system containing a massive primary and a much lower mass secondary. Because the more massive star evolves off the main sequence earlier, it initiates mass transfer onto the lower mass companion first. For the mass ratios present in LMXB progenitors, this transfer is often unstable, and so the system evolves into a common-envelope (CE) phase Ivanova et al. (2013); Kalogera & Webbink (1998). During CE evolution, the secondary spirals inward inside the primary's envelope, and the orbital energy ejects the common envelope. If the envelope is successfully ejected before the stars merge, the post-CE binary is left in a much tighter orbit containing the stripped core of the original primary and the main sequence low mass companion. This orbital shrinkage is essential, because without it the system would likely remain too wide to become an interacting X-ray binary.

The core of the primary then continues its evolution until it explodes as a core-collapse supernova (CCSN) and forms a neutron star or black hole. To form an LMXB, the binary must survive any natal kick imparted at compact object birth. This post supernova survival requirement is one of the most restrictive bottlenecks in the standard channel, because a system that survives CE can still be disrupted when the compact object forms Kalogera & Webbink (1998); Tauris & van den Heuvel (2006). Thus the canonical picture contains a strict sequence of stringent filters where the progenitor binary must not merge during CE evolution, must emerge at the right separation, and then must remain bound after the supernova with orbital parameters that still permit later interaction.

If the post SN binary remains closely bound, the final step is the onset of Roche lobe overflow (RLOF) from the low mass companion following angular momentum loss driven by magnetic braking or gravitation radiation (Tauris & van den Heuvel, 2006). Magnetic braking is especially important for donors with convective envelopes at relatively longer periods, while gravitational wave radiation dominants at the shortest periods. Together these processes shrink the orbit until the companion fills its Roche lobe and transfers mass to an accretion disk and eventually onto the compact object. Once this mass transfer phase begins, the system is observed as an LMXB, and its subsequent evolution can produce a persistent source, a transient source, and sometimes a recycled millisecond-pulsar system (Podsiadlowski et al., 2003).

3 LMXB Outbursting and Transient Behavior

3.1 Observational Features of Transient LMXBs

X-ray binaries are most readily recognized through their outbursts and variability. In transient systems, the light curve of the canonical accretion disk outburst shows a comparatively fast rise followed by a longer plateau and an exponential (radiative) decay back toward quiescence (Chen et al., 1997). This morphology, known as FRED, is predicted by the disk instability model (DIM), in which the outburst begins when a thermal-viscous instability triggers a heating front that rapidly ionizes the disc, while the subsequent decline is governed by viscous evolution, irradiation from the compact object, radiative cooling of the disk, and, at later times, by the propagation of cooling fronts as irradiation weakens (Dubus et al., 2001; Hameury, 2020; Lasota, 2001). Real outbursts are frequently more complicated, particularly after the rise where the lightcurve can show plateaus, secondary maxima, reflaring events, and rebrightenings, indicating that irradiation, disk truncation, mass-transfer variations, and outflows all shape the observed light curve in ways that are not yet fully captured by the modifications to DIM. The characteristic outburst durations likewise span a wide range, from weeks to months and in some cases much longer, which is one reason that long-term continuous monitoring is so important for discovering and characterizing LMXBs.

A key challenge to discovery of these systems is that both the recurrence time and the outburst duration of X-ray binary outbursts are highly variable from source to source. Some transients recur on timescales of only a few years, whereas others may remain quiescent for decades between major outbursts, and even within a given source different outbursts can have different durations, amplitudes, and morphologies (Tetarenko et al., 2016). The WATCHDOG catalog of galactic black hole X-ray binaries by Tetarenko et al. (2016) shows the great variation in outburst duty cycles and recurrence time across the known population of BH-LMXBs, and that our cataloged population therefore may oversample systems that are bright, long-lived, or recently active during the era of all-sky monitoring. This matters physically as well as observationally: recurrence times correlate to how quickly mass is supplied and stored in the disk before the next outburst, while bright times depend on how the disk is drained, irradiated, and perhaps depleted by winds or jets during the outburst itself (Dubus et al., 2001; Tetarenko et al., 2018).

In addition to brightness changes, X-ray binaries are characterized by correlated evolution in spectral hardness and luminosity, usually summarized in terms of accretion states. In black hole transients, outbursts commonly begin in a hard state dominated by a hard Comptonized spectrum (HCS) and strong aperiodic variability, then soften to the intermediate state (IMS), and in many cases reach a soft, thermally dominated state (SDS) in which the disk contributes most of the luminosity and the rapid variability is much weaker (Done et al., 2007; Remillard & McClintock, 2006). In hardness–intensity diagrams, this standard evolution traces a counterclockwise, q-shaped hysteresis pattern, with the return transition from the soft to the hard state occurring at a lower luminosity than the original hard-to-soft transition (Maccarone et al., 2003), meaning that state transitions are not dependent on instantaneous accretion rate or temperature alone. Additionally, a substantial fraction of LMXB outbursts are now recognized as failed transition outbursts, in which the source remains in the hard state throughout and never reaches the fully soft, disc-dominated phase Alabarta et al. (2021).

3.2 Accretion Disk Outbursts and the Disk Instability Model

As briefly discussed in the previous section 3.1, the standard framework for interpreting the outbursts of transient low mass X-ray binaries is the disk instability model (DIM), in which the accretion disk cycles between a cool, netural state and a hot, fully ionized state because the disk opacity changes abruptly when hydrogen ionizes (Hameury, 2020). In quiescence, matter transferred from the donor accumulates in the disk until the local surface density exceeds a critical threshold on the cool branch of the thermal equilibrium curve. At that point a thermal-viscous runaway is triggered, a heating front propagates through the disc, and the system enters outburst; later, once the disk has been sufficiently drained and can no longer remain fully ionized, cooling fronts propagate inward and return the system to quiescence. DIM provides the basic physical model for why many LMXBs are transients rather than persistent accretors.

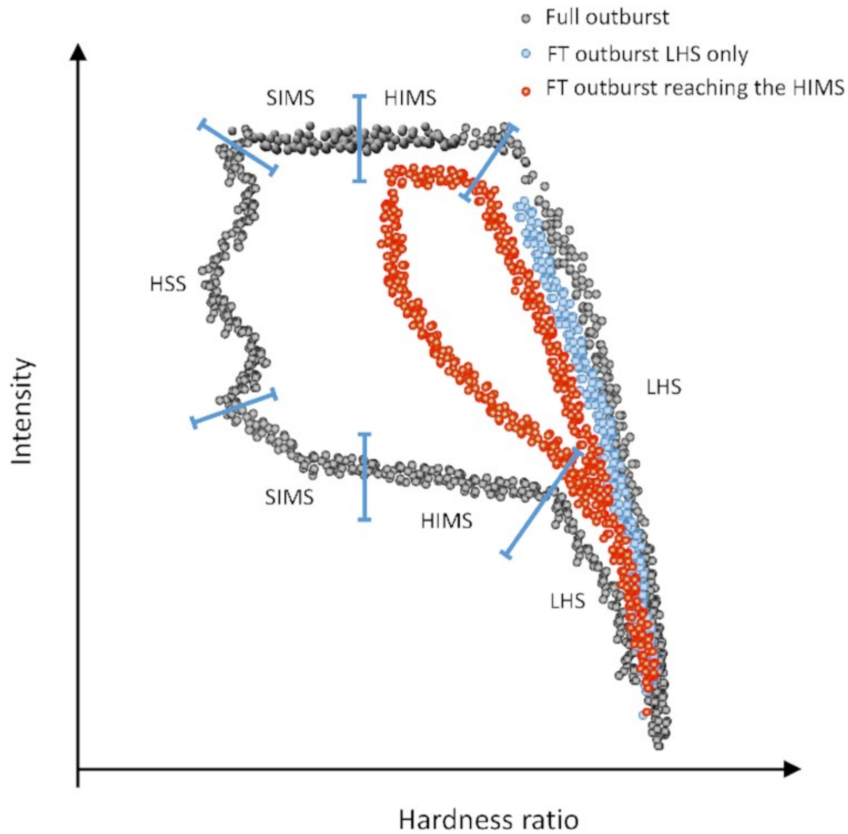

Figure 1.1: The hardness vs intensity diagram of a canonical full outburst, as well as two hard-only or failed transition outbursts, taken from Alabarta et al. (2021).

For LMXBs, however, the standard DIM must be modified in several important ways to reproduce the observed outburst behavior. The most important addition is X-ray irradiation of the disk by the central source, since irradiation can keep a much larger fraction of the disk in the hot state than would otherwise be possible, prolonging the outburst and producing the long bright states and slow decays typical of X-ray transients (Dubus et al., 1999; King, 1998) This also explains why the lightcurve in the soft X-ray state decays at either an exponential or linear rate under different irradiation conditions, and why LMXB outbursts are generally longer and more luminous than dwarf-nova outbursts in cataclysmic variables. Inner-disk truncation/evaporation in quiescence helps explain low quiescent luminosities and long recurrence times by preventing the thin disk from extending all the way to the compact object at all times and increasing inner disk stability (Menou et al., 2000). More recent reviews also emphasize that irradiation of the donor, mass-transfer variations, and possibly winds and outflows that exert a torque on the disk can materially alter the light curve morphology, recurrence cycle, and decay profile, especially in systems that show plateaus, reflaring, or unusually complex outbursts (Hameury, 2020; Lasota, 2001). While the DIM remains the base model of the theory, a modified version accounting for a irradiated, truncated, and wind-modified disk reproduces LMXB outbursts more accurately compared to the simple thin-disk model.

A central issue to all variations of DIM is that accretion onto the compact object requires the transport of angular momentum outward. Without this transport, gas cannot spiral inward and release gravitational energy. The classical Shakura-Sunyaev (α)-prescription parameterizes this transport in terms of a viscosity, but it does not identify the underlying physical mechanism. A breakthrough came with the discovery by Balbus & Hawley (1991) of the magnetorotational instability (MRI), where magnetic fields in a differentially rotating disk produces the viscosity needed for angular momentum loss and accretion of matter onto the compact object (Balbus & Hawley, 1998). For hot, ionized accretion disks, the MRI is therefore an explanation for the high mass transfer rate. However, quiescent disks in LMXBs are expected to be largely neutral, so MRI should be inefficient or absent there, implying that some other transport channel such as magnetically driven wind may be needed in the low state, where the accretion rate is low but nonzero (Lasota, 2023).

Despite its success, the DIM still leaves open the question of what triggers an outburst in a given source and at a given time. The theory predicts the onset of an outburst when one part of disk locally crosses the critical surface density/temperature for thermal instability, but the parameters that determine when this happens are much less certain. Also unknown is whether this occurs near the compact object and propagates outwards (i.e. inside-out), or whether the reverse (outside-in) is true. The relevant ingredients likely include the secular mass-transfer rate from the donor, fluctuations in that transfer rate, the degree of inner-disk truncation during quiescence, the efficiency of irradiation, and the role of winds or other non-local torques in redistributing mass and angular momentum (Hameury, 2020).

A second set of open problems surrounds failed outbursts and recurrence times. Observationally, many black hole LMXB outbursts do not execute the full canonical hard-to-soft cycle. Instead, they brighten and then fade while remaining in the hard state, resulting in a failed transition outburst. Alabarta et al. (2021) showed that these failed transition outbursts comprise roughly one-third of all outbursts in their sample of black hole LMXBs. Their existence implies that launching a heating front and increasing the accretion rate does not guarantee a full outburst that progresses to the soft state. Likewise, the enormous range in recurrence times from years to decades shows that we still do not understand how quickly discs refill, how much mass is left behind after an outburst, or how truncation, irradiation, winds, and donor behavior combine to set the next cycle (Lasota, 2023). Although the typical light curves of X-ray transients can often be approximated via DIM, their decay phases in particular are not simple exponentials, and many observed light curves are far more complex than the canonical model suggests. DIM therefore remains a useful starting point for LMXB outbursts, but there remains work to be done to find a theoretical framework that explains all aspects of LMXB outburst morphology.

3.3 X-ray Driven Discovery

Low mass X-ray binaries (LMXBs) are most often discovered through their accretion-powered X-ray emission. Because a neutron star or black hole accreting from a low mass donor radiate from quiescent luminosities of roughly $10^{30} - 10^{34}\,\mathrm{erg\,s^{-1}}$ up to outburst luminosities approaching $10^{40}\,\mathrm{erg\,s^{-1}}$ from such a small region, the radiation from these objects generally peaks in the X-ray and are often some of the brightest sources in the X-ray sky. Early catalogs of galactic LMXBs (Liu et al., 2007; Ritter & Kolb, 2003a) were therefore assembled from X-ray detections.

X-ray all-sky monitors (ASM) have been especially important (Priedhorsky & Holt, 1987) because their wide FOV means they are likely to catch LMXB outbursts as long as their flux exceeds the all-sky monitor threshold (i.e. during outburst). The first ASM dedicated to astronomical observations was launched aboard the Ariel-5 satellite in 1975 Holt et al. (1979), although earlier ASMs aboard the Vela satellites designed to monitor the Earth for nuclear detonations had serendipitously discovered a number of high energy transients of cosmic origin (Klebesadel et al., 1973). The Rossi X-ray Timing Explorer (RXTE) ASM launched in 1995 was much more sensitive than previous ASMS and repeatedly covered the entire in the 1.5–12 keV band roughly 5-10 times per day, making it the first tool for systematically tracking X-ray transient lightcurves at scale (Levine et al., 1996). MAXI scans the entire sky twice per 90 min orbit from the International Space Station, with two cameras covering energy ranges of 0.5-12 keV and 2-30 keV Matsuoka et al. (2009). At hard X-ray energies, the Swift/BAT transient monitor added complementary sensitivity to spectrally hard and absorbed systems, observing 88% of the sky every day in the 15-50 KeV energy range (Krimm et al., 2013). More recently, the Einstein Probe (Yuan et al., 2022) observes the entire sky several times per day at soft X-rays at a sensitively an order of magnitude fainter than MAXI.

All-sky monitors, however, are only one part of the discovery chain. Survey missions such as ROSAT, *XMM-Newton*, *Chandra*, *Swift*, and *eROSITA* have been important for building X-ray catalogs that capture sources at greater sensitivity than the all sky monitors. These instruments also provide better localizations and photometric measurements, which make it possible to connect the transients seen by monitors to persistent source catalogs and, ultimately, to counterparts at other wavelengths. Many of our known LMXBs were first discovered via a trigger by an all sky monitor, which prompted followup by one of these X-ray missions.

Despite these successes, X-ray selection alone has several limitations. X-ray monitors are intrinsically biased toward bright, long-duration, or frequently recurring outbursts, so the observed sample over-represents systems with high duty cycles and and short recurrence times that are bright enough to trigger an all sky monitor. The positional uncertainties of wide-field instruments are generally too large to identify a unique optical or infrared (OIR) counterpart in crowded regions of the galactic plane or bulge, which means that X-ray transients require deeper follow-up to localize and classify successfully (Jonker et al., 2011). Note that source catalogs do not contain classifications for most of their sources, as the nature of many sources remain unresolved until they can be combined with multiwavelength data from OIR observations. In other words, the X-ray-selected LMXB population is shaped not only by the underlying astrophysics, but also by the cadence, sensitivity, energy band, and localization precision of the instruments that discovered it.

As such, LMXBs are best found and classified based on a multiwavelength approach in which X-rays remain essential but are no longer sufficient on their own. The Galactic Bulge Survey (GBS, Jonker et al., 2011) by the *Chandra* observatory was designed explicitly around this logic, first using X-ray observations to find compact accretors, and then combining them with optical follow-up to enlarge the sample of neutron star and black hole LMXBs suitable for dynamical study and population inference. Likewise, catalogs such as WATCHDOG and BlackCAT have made clear that the X-ray selected population of LMXBs is only a subset of the full galactic population (Corral-Santana et al., 2016).

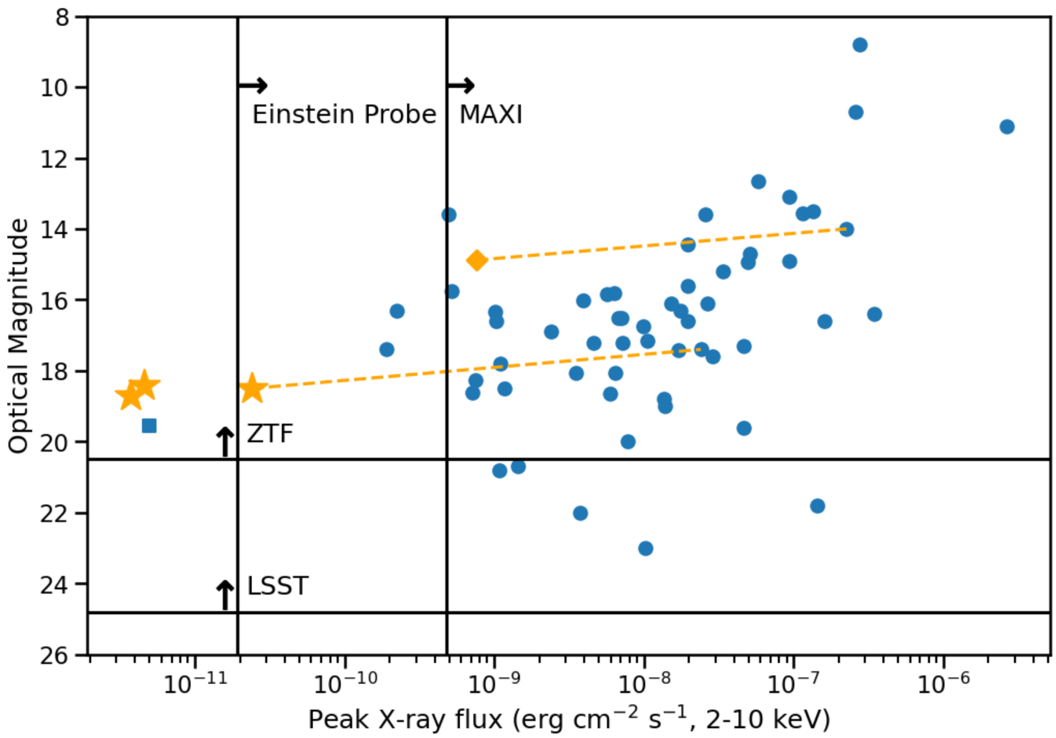

Figure 1.2: LMXBs in outburst can be optically discoverable before their X-ray flux exceeds the sensitivity of X-ray all-sky monitors. Optically discovered outbursts by ZTF (stars) abd ASAS-SN (diamonds) are plotted in gold: : Swift J1943.4+0228 (Wang & Bellm, 2022), XTE J1859+226 (Bellm, 2021a), AT2019wey (Yao et al., 2021), and ASASSN-18y/MAXI J1820+070 (Tucker et al., 2018). The initial discovery and peak brightness are connected with dotted lines for AT2019wey and MAXI J1820+070, demonstrating that the optical flux nears peak levels much earlier than X-ray flux. LSST will observe outbursts too faint for X-ray monitors. Blue points show peak optical magnitude and X-ray flux for known BH LMXBs (Corral-Santana et al., 2016). Figure taken from Bellm (Priv. Communication)

3.4 Optical Signatures of LMXBs

Optical observations are important for the study of LMXBs because they provide information complementary to the X-ray data. Once an X-ray source has been localized to a few arcsecond error circle, optical imaging and spectroscopy are often taken to determine which object is the true counterpart, especially in crowded galactic fields where multiple stars may fall inside the X-ray positional uncertainty (Jonker et al., 2011; Wevers et al., 2016). Optical data also probe physical regions of the disk that are complementary to the X-ray emitting inner flow. The optical band is sensitive to the donor star, the outer accretion disk, and irradiation of the binary on larger scales than those traced directly by X-rays (Charles & Coe, 2003; van Paradijs & McClintock, 1995). Just as importantly, optical monitoring can provide denser and longer-baseline time-domain coverage than is typically available from X-ray all-sky monitors, allowing one to follow quiescent variability and the earliest phases of outburst development in systems that remain below X-ray survey thresholds for most of their lifetimes (Goodwin et al., 2020; Russell et al., 2019).

The optical signature from LMXBs contains contributions from several physically distinct emission components whose relative importance changes with accretion state (Charles & Coe, 2003). In quiescence, the donor star can dominate the optical and near infrared emission, but even then the accretion flow can contribute flickering and line emission. During active states, the thermal emission from the accretion disk makes up a substantial portion of the optical light, while reprocessed X-ray irradiation of the disk and the inner face of the companion can boost the optical luminosity and imprint correlations between optical and X-ray brightness (Ducci et al., 2019; Russell et al., 2006). In black hole systems, compact jets can also make an important contribution, especially in the hard state and particularly at redder optical and near infrared wavelengths, where synchrotron emission may dominate over the thermal disk emission (Russell et al., 2006). In some systems such as Swift J1357.2-0933, synchrotron emission may remain dominant even in quiescence (Shahbaz et al., 2013). Because these components respond differently to changes in accretion rate and spectral state, optical colors, spectra, and variability provide a powerful diagnostic of which physical channel is dominating at a given time.

In quiescence, optical observations are especially valuable because they can reveal the underlying binary geometry needed for dynamical studies. Many quiescent LMXBs show the double-humped ellipsoidal modulation expected from a donor star overflowing its Roche lobe, and modeling that modulation is a standard route to constraining the binary inclination and the relative contribution of the donor and disk light (Casares & Jonker, 2014; Shahbaz et al., 2013). Optical colors and spectra further constrain the donor type and the amount of obscuration by the accretion flow, both of which are required to interpret radial velocity curves and derive robust compact object mass limits (Casares & Jonker, 2014).

During outburst, the optical phenomenology becomes even richer and may offer a window into the evolving accretion flow, particularly during the disk state change. LMXBs typically brighten by up to 6 magnitudes in the optical during outburst (Charles & Coe, 2006), often showing characteristic rise and decay morphologies that broadly track changes in the accretion disk and irradiation geometry. Optical colors evolve during outburst as the effective disk temperature changes and as the relative contribution of the disk, reprocessed emission, and any jet component shifts with luminosity and accretion state (Russell et al., 2006;

Tetarenko et al., 2021). In some systems, the optical emission can begin rising before the X-rays become detectable, making optical monitoring a sensitive probe of outburst triggering in the outer or truncated disk. For example, V404 Cyg brightened by 0.1–0.3 mags compared to the quiescent orbital modulation roughly a week before the Swift/BAT trigger (Bernardini et al., 2016), while SAX J1808.4-3658 showed enhanced optical activity starting 12 days before the first X-ray detection and a 4-day delay relative to the optical in the X-ray rise delay during the 2019 outburst (Goodwin et al., 2020). Observations taken by the XBNews group (Russell et al., 2019) also found optical outbrusting preceeding the X-ray outburst in several systems. These results show that optical observations can be a distinct discovery and diagnostic channel for the earliest stages of LMXB outbursts, and may allow for earlier detection of outbursts.

Additionally, Alabarta et al. (2021) found that prior to full outbursts of GX 339-4, the optical and infrared flux was generally fainter than prior to a failed transition outburst. By contrast, analysis of a sample of 128 outbursts from 56 black hole LMXBs found that full and failed transition outbursts were indistinguishable from their X-ray lightcurves, hardness intensity diagrams, or X-ray variability during the initial outburst onset. Assuming that the OIR emission was mostly from the outer accretion disk, this would imply that the outer part of the disk is more massive prior to a failed transition outburst than a full outburst.

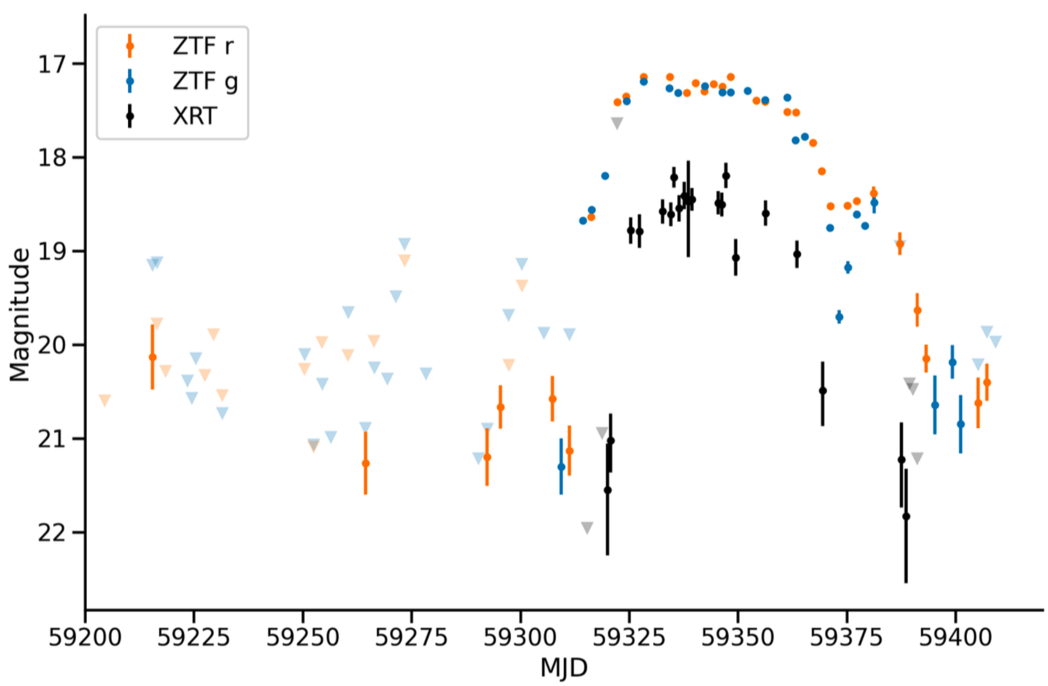

Figure 1.3: Optical and X-ray lightcurve of the optically discovered outburst of the BH XRB Swift J1357.2-0933 in 2021 (Bellm, 2021b, Priv. Communication)

.

4 The Observed Galactic Population

The presently known galactic LMXB population numbers of order a few hundred systems, although the exact total depends on how candidate systems are treated. The recent XRBcats catalog lists 349 galactic LMXBs (Avakyan et al., 2023), whereas the LMXBwebcat catalog lists 339 galactic LMXBs (Fortin et al., 2024). Both catalogs nearly double the number systems listed in the older Liu et al. (2007) and Ritter & Kolb (2003a) catalogs, illustrating both the continuing discovery and the progressive classification of previously uncertain systems over the past 15 years. The sky distribution of the known population are concentrated toward the inner Galaxy and bulge, and they have a broader vertical distribution than HMXBs, with a characteristic scale height of about 410 pc (Grimm et al., 2002a).

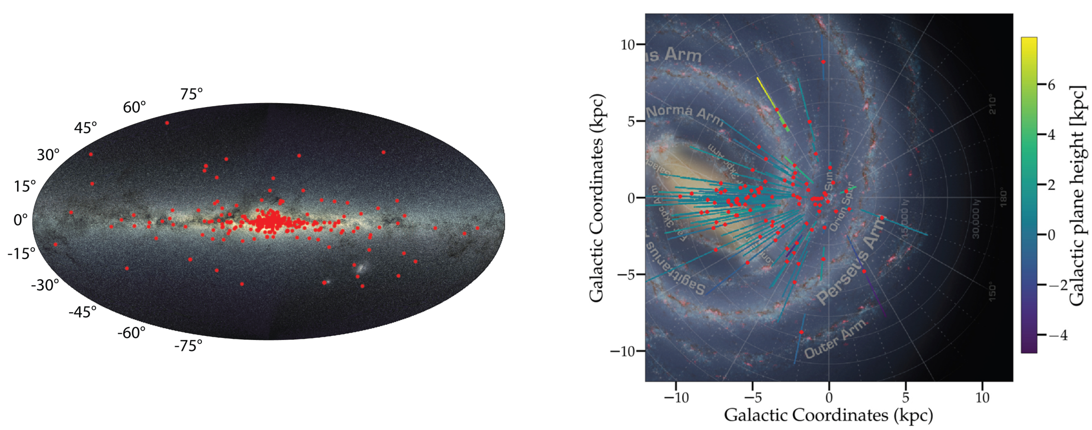

Figure 1.4: The distribution of LMXBs throughout the galaxy. Left: edge-on view of 339 LMXBs with emphasis on the galactic height and latitude. Right: face-on view of 98 LMXBs with Gaia parallaxes, with bars showing 1-σ distances. Taken from Fortin et al. (2024). Background image credits: ESA/Gaia/DPAC (left), NASA/JPL-Caltech/R. Hurt (SSC/Caltech) (right)

Recent catalogs also make a distinction between systems with verification and sources whose classification remains more indirect. The most secure black hole identifications are those with dynamical mass constraints, as reviewed by Casares & Jonker (2014) and cataloged by Corral-Santana et al. (2016), while many additional black hole LMXB systems are candidates identified from their X-ray properties or outburst behavior rather than from a dynamical mass measurement. By contrast, many neutron star LMXBs are securely identified through type I X-ray bursts or coherent pulsations. Fortin et al. (2024) attach reliability flags to compact object type in their catalog and the current galactic LMXB population should be taken as a combination of dynamically confirmed black holes, burst/pulsation-confirmed neutron stars, and a broader set of candidate LMXBs that are more indirectly classified via lightcurve morphology and other properties measured from the outbursts, such as changes in state in the X-ray hardness.

The outburst properties of the galactic LMXB population are also diverse. Transient LMXBs typically span X-ray luminosities from roughly $10^{36-40}\,\mathrm{erg\,s^{-1}}$ in outburst, while quiescent luminosities are many orders of magnitude lower. Persistent systems occupy the high end of the accretion-rate distribution, whereas transients spend most of their time in quiescence and are detected primarily during episodic activity (Grimm et al., 2002b). For black holes, the WATCHDOG database tracked activity from 47 transient and 10 persistent galactic black hole X-ray binaries and identified 132 transient outbursts between 1996 and 2015, demonstrating that outburst duty cycles, bright times, and recurrence properties vary substantially from source to source (Tetarenko et al., 2016). For neutron star LMXBs, Heinke et al. (2025) catalog outbursts from 85 confirmed NS LMXBs and show that 40 of these 85 systems had zero or one recorded outburst between 1996 and 2023, implying long recurrence times and likely incompleteness below all-sky monitor detection limits. They further argue that since outburst detection has been relatively efficient since 1996 for events brighter than about $F_{2-10}\,\mathrm{keV} \approx 3 \times 10^{-10}$ $\mathrm{erg\,s^{-1}\,cm^{-2}}$ the observed transient population is still shaped strongly by X-ray monitoring thresholds.

A further important aspect of the currently known population is that a substantial fraction of outbursts fail to undergo a full transition into the soft X-ray state. In a sample of 56 black hole LMXBs undergoing 128 outbursts, 36% of systems experienced at least one failed-transition outburst and these events accounted for about 33% of the outbursts of the sample (Alabarta et al., 2021). This is consistent with an earlier result using the WATCHDOG database that a substantial fraction of galactic black hole outbursts are hard only events rather than full state transition outbursts (Tetarenko et al., 2016). Because many of these failed transition outbursts are much shorter in duration or fainter in luminosity than full transitions, our currently X-ray monitoring may be missing these outbursts due to lack of sensitivity for wide-field instruments and coverage for more sensitive missions. Long term optical monitoring of known LMXB systems are already discovering failed transition outbursts that do not register with X-ray monitors (Baglio et al., 2022; Bellm et al., 2023), demonstrating the utility of optical observations.

Recent catalogs show an improvement in counterpart completeness, but not every LMXB has a known optical or infrared (OIR) counterpart. Both recent LMXB catalogs include OIR counterparts from Gaia, 2MASS and WISE. Even so, both efforts underline the fact that many systems still lack well-constrained counterparts or basic binary parameters, especially in crowded or highly extincted regions of the inner Galaxy, where cross-identification and follow-up remain difficult (Avakyan et al., 2023; Fortin et al., 2024).

Taken together, current catalogs and outburst databases show the known galactic LMXB population contains roughly 340–350 systems, is concentrated toward the bulge and inner Galaxy, contains a mixture of securely identified and candidate neutron star and black hole accretors, and remains strongly shaped by the selection effects of X-ray monitoring and the incompleteness of optical/infrared follow-up (Arur & Maccarone, 2017).

5 LMXBs in the Time-Domain Era

5.1 The Landscape of Optical Time Domain Surveys

Large sky surveys have repeatedly reshaped our understanding of astrophysics by converting rare classes into statistical populations. The Catalina Real Time Transient Survey (CRTS; Drake et al., 2009) imaged over 30,000$^{\circ 2}$ of the sky and was the first survey to send out real time information on sources that change in brightness within minutes of discovery. CRTS substantially increased our known populations of many transient and variable objects, such as cataclysmic variables, active galactic nuclei, and supernovae, and discovered some rare transients such as super luminous and long duration supernovae. Subsequent surveys, like the Palomar Transient Factory (PTF; Law et al., 2009; Rau et al., 2009), Pan-STARRS (Chambers et al., 2016), the All-Sky Automated Survey for Supernovae (ASAS-SN; Kochanek et al., 2017), the Zwicky Transient Facility (ZTF Bellm et al., 2019a), and the Asteroid Terrestrial-impact Last Alert System (ATLAS; Tonry et al., 2018), have provided greater coverage of the optical transient phase space via increased sensitivity, cadence, or followup capabilities.

In the coming decade, Rubin Observatory's Legacy Survey of Space and Time (LSST, Ivezić et al., 2019) will observe the sky at an unprecedented combination of cadence, depth, and coverage at optical wavelengths. The Nancy Grace Roman Space Telescope (Spergel et al., 2015) will survey the near infrared sky, providing a window into the heavily reddened environments in the galactic bulge. Wide area coverage of the sky at X-ray wavelengths also provides a complementary high-energy discovery space (e.g. the Einstein Probe, Yuan et al., 2015). This combination is especially promising for studying low mass X-ray binaries (LMXBs), which require multi-wavelength observations to fully characterize, and are high variable and frequently discovered as transients.

5.2 Rubin Observatory and LSST

The Vera C. Rubin Observatory's Legacy Survey of Space and Time (LSST) is a 10 year, wide-field synoptic survey of the southern sky, with a survey area of 18,000$^{\circ 2}$ in six bands,(*ugrizy*), with 5-σ single-exposure point-source depths of u=23.9, g=25.0, r=24.7, i=24.0, z=23.3, and y=22.1 mag, while the ideal 10-year coadded depths reach u=26.1, g=27.4, r=27.5, i=26.8, z=26.1, and y=24.9 mag (Ivezić et al., 2019, Table 1).

For transient science, the power of LSST lies in this combination of coverage, depth, and cadence and makes it an order of magnitude more powerful than any other synoptic survey (Bellm, 2016). Rare events require large sky coverage, transient events require regular revisits, and intrinsically faint or distant events require substantial photometric depth. LSST is unique in that it provides all three simultaneously. LSST will measure not just the existence of a transient source, but its rise, color evolution, and decay across a very large dynamic range in brightness and timescale. For galactic transients, this is especially important because many classes of variable and eruptive systems evolve on day-to-week timescales, so a survey that is both deep and high cadence can recover events that would be missed by shallower or more sparsely sampled optical programs.

A second major advantage for transient work is Rubin's real-time alert infrastructure. Rubin's prompt pipelines perform image differencing on new exposures and distribute alerts within about 60 seconds of shutter close, with roughly $\sim$ 10,000 alerts per visit and about $\sim$ 7–10 million alerts per night (Ivezić et al., 2019). These alerts will be distributed to brokers, where users can then set up their own filters or search criteria to narrow the alert stream to a list of candidates.

For galactic transient science, the most important consequence of the LSST survey design is that it enables time-domain studies at both large scale and substantial depth. This is especially relevant for low mass X-ray binaries, whose duty cycles are often low, whose outbursts can evolve on day-to-week timescales, and whose quiescent counterparts are frequently too faint for previous wide-area surveys to characterize uniformly. The Rubin Observatory will therefore expand the observational parameter space in which these systems can be studied by increasing the accessible volume for optical outburst discovery, improving the census of faint and quiescent counterparts, and providing multi-band light curves for population-level analyses. These capabilities motivate the use of LSST not only as a discovery instrument for compact binaries, but also as a tool for constraining the galactic population and evolutionary history of LMXBs.

LSST should enlarge our sample of quiescent optical counterparts. Monitoring counterparts in quiescence is important because ellipsoidal modulations in the light curve constrains the geometry of the Roche-lobe-filling donor, broadband colors and spectroscopy can give the donor type and the proportion of disk contamination, and together these measurements underpin dynamical mass estimates for compact objects (Casares & Jonker, 2014; Charles & Coe, 2006). The logic of surveys such as the galactic Bulge Survey was already that enlarging the sample of quiescent accreting binaries is necessary for constraining black hole masses and binary evolution (Jonker et al., 2011). LSST extends that strategy to a much deeper, wider, and more uniform time domain dataset, with repeated (*ugrizy*) imaging over the southern sky, and should therefore recover counterparts that were too faint, too weakly variable, or too poorly sampled in previous wide-area optical surveys (Ivezić et al., 2019).

Another major impact is that LSST should discover new outbursting LMXBs directly through their optical variability, rather than only through triggers from X-ray all-sky monitors. This is important because the known galactic transient population is strongly shaped by discovery bias, as WATCHDOG showed that the observed black hole X-ray binary sample is dominated by systems caught during bright X-ray activity between 1996 and 2015 (Tetarenko et al., 2016), and BlackCAT emphasized that only a small fraction of the total galactic black hole transient population has likely been found so far (Corral-Santana et al., 2016). Optical monitoring also provides a complementary discovery channel because outbursts also brighten substantially at optical wavelengths, and failed transition outbursts may only substantially brighten in the optical. Prior to the failed outburst in 2020, the LMXB Centaurus X-4 had not undergone outburst since 1979 (Baglio et al., 2022), and we may be missing other infrequent LMXB outbursts if we do not discover them in the optical. Finally, at least some systems, the optical rise precedes the X-ray trigger (Russell et al., 2019), which may allow us to probe the physics surrounding the initial onset of the state change.

6 The Structure and Outline of this Thesis

In this introduction we have outlined the current state of the field of low mass X-ray binary (LMXB) theory and observation, and describe the transformative capabilities of the Vera Rubin Observatory and the upcoming Legacy Survey of Space and Time. We cover the historical and ongoing X-ray driven discovery and observation, as well as an emerging field of not only optical followup of LMXB outbursts, but optical discovery and monitoring as well. We address our current understanding of the physics of LMXB outbursts and remaining questions surrounding the initiation of outbursts, and the presence of failed transition

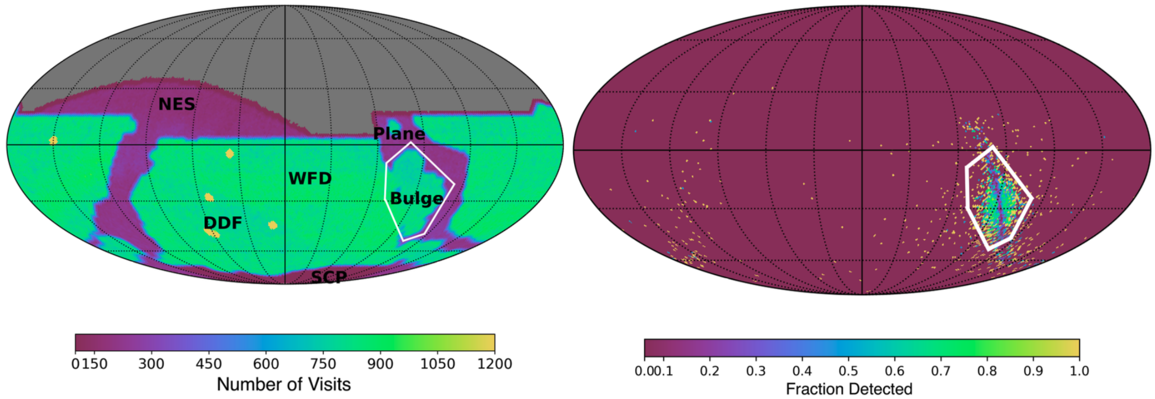

Figure 1.5: Left: The number of visits by the Vera Rubin Observatory over the full 10 year survey. (v3.3 baseline). Many known LMXBs are located in the Galactic Bulge, outlined in white. This region will be visited over 1000 times. Right: Fraction of XRB outbursts detected by using simulations of LSST observations. The vast majority of detected XRBs are in the Galactic Bulge. Figure from Bellm (Priv. Communication).

outbursting. We also discuss how LMXBs are thought to form via binary stellar evolution, and that our current models have many parameters that are not yet fully constrained.

The subsequent chapters, I describe my study of LMXBs both via observations and via simulations and theory. I cover the use of sky surveys and alert streams, tools that entered the mainstream in the previous decade. Then I take a digression to discuss the kinds of questions a larger population of LMXBs could help answer. Lastly, I look ahead to a new era when the Vera Rubin Observatory's Legacy Survey of Space and Time (LSST) will transform optical time domain astronomy.

In Chapter 2, I cover my search for optical outbursts of LMXBs in the Zwicky Transient Facility (ZTF) alert stream. I describe my methods of pulling in existing X-ray data and prior observations to select candidates for further using the X-ray telescopes and optical spectroscopy. I then use a small sample of discovered outbursts to make inferences about the galactic LMXB population and look ahead to how Rubin's increased sensitivity and 10 year baseline could lead to more optical discoveries of LMXBs. This work was originally published in ApJ (Wang et al., 2024).

In Chapter 3, I use `cogsworth` to simulate a population of LMXBs and compare their observable properties to our currently known population. I then vary the configurations of the simulations to learn how different binary stellar evolution models can impact the number of LMXBs synthesized, as well as their observable properties, with special focus on properties that include positional information.

In Chapter 4, I present an exploratory crossmatch between the Rubin Data Preview 1 (DP1), the first publicly available data taken by the Vera Rubin Observatory, and describe some challenges for making the multiwavelength associations that are crucial for classifying X-ray emitting sources like LMXBs. This work was originally published in ApJS (Wang et al., 2026).

Finally, Chapter 5, I summarize the work completed and its place in the context of the start of LSST.

CHAPTER 2

AN OPTICAL SEARCH FOR NEW OUTBURSTING LOW MASS X-RAY BINARIES

1 Introduction

X-ray binaries (XRBs) are interacting binary systems containing a neutron star or black hole and a stellar companion. In Low Mass X-ray Binaries (LMXBs), matter from a low mass stellar companion is transferred into an accretion disk via Roche Lobe overflow. The accretion of matter onto the compact object does not happen uniformly, which leads the LMXB to undergo outbursts (King & Ritter, 1998; Shakura & Sunyaev, 1973). The most widely discussed mechanism for these outbursts is the Disk Instability Model (DIM; for a detailed review, see Hameury, 2020). In this model, the luminosity of these systems can increase by many orders of magnitude when an instability (perhaps the Magnetorotational Instability; Balbus & Hawley, 1998) causes the accretion disk to become ionized, leading the mass transfer rate onto the compact binary to dramatically increase and causing a transient outburst event. High Mass X-ray Binaries (HMXBs) are mostly persistent, wind-fed systems. Many, but not all, of these objects lack accretion disks and prominent optical outbursts (Reig & Fabregat, 2015).

Accretion outbursts of LMXBs typically exhibit a characteristic fast rise, exponential decay temporal profile (Chen et al., 1997). The initial rise of several days to weeks corresponds to complete ionization of the accretion disk and increase in mass transfer onto the compact object, followed by a long decay as energy is radiated, cooling the ionized disk. The decay portion of the outburst can last for hundreds of days or even years, as irradiation from the compact object can sustain ionization of the inner disk (Dubus et al., 2001; King & Ritter, 1998). The end of the outburst can transition to a linear decay (King & Ritter, 1998; Tetarenko et al., 2018) as the disk changes back to its neutral state. While the narrative provided by the disk instability model (DIM) matches the overall observed behavior of outbursts, many key details of the process remain uncertain, including the mechanism that triggers the outburst onset. The location where this instability originates and the process by which it propagates throughout the disk are also not well understood. Also uncertain are why some outbursts fail to progress to the disk-dominated high-soft state, resulting in a smaller and shorter "failed transition" outbursts (Alabarta et al., 2021).

Many modifications to the model have been proposed to account for observations, including irradiation of the disk (King, 1998; Niwano et al., 2023), tidal forces (e.g., Priedhorsky & Verbunt, 1988), and disk winds (e.g., Neilsen & Degenaar, 2023, and references therein). Discoveries of both new XRBs and new XRB outbursts may help answer these questions and clarify the underlying physical processes that necessitate these modifications.

The discovery of X-ray Binaries has largely been driven by X-ray all-sky monitors, such as the All-Sky Monitor (ASM) on the Rossi X-ray Timing Explorer (RXTE). However, while the sensitivity of these instruments, around $10^{-8}\,\mathrm{ergs\,cm^{-2}\,s^{-1}}$ (about $10^{35} - 10^{36}\,\mathrm{ergs\,s^{-1}}$ at fiducial galactic distance (Krimm et al., 2013; Matsuoka et al., 2009)), can detect the intense radiation from outbursts, they miss X-ray Binaries in quiescence ($10^{29} - 10^{33.5}\,\mathrm{ergs\,s^{-1}}$), and can miss weak/low luminosity outbursts, such as outbursts from very faint x-ray transients (VFXTs; e.g., Armas Padilla et al., 2014; Heinke et al., 2015). Focusing X-ray telescopes such as Chandra, XMM-Newton, and Swift have the sensitivity to detect much fainter sources and their higher resolution also provides more precise spatial localization. However, their smaller field of view means that their combined sky coverage is much smaller than the all-sky monitors. Additionally, classification of detected X-ray radiation as an outbursting X-ray Binary can be difficult with both all sky monitors and the more sensitive X-ray source catalogs, particularly for fainter, shorter duration outbursts that are only observed serendipitously, meaning that a number of LMXBs may be catalogued but not classified.

Optical detection and monitoring offers an alternate pathway to discovery and characterization of X-ray binaries. Empirically, the initial stages of the outburst can first be observed at optical wavelengths several days before the X-ray outburst (Russell et al., 2019). For example, the X-ray binary AT2019wey (Yao et al., 2021) was discovered first in the optical by ATLAS (Tonry et al., 2019) and was monitored by the Zwicky Transient Facility months before a detection of an X-ray outburst (Mereminskiy et al., 2020). Since the optical outburst can precede the X-ray brightening, this can enable earlier X-ray followup during the initial rise and the study of the mechanisms that trigger the outburst, which are not understood due to a relative rarity of observations during the earliest phases of outburst onset. However, an optical search requires a fast cadence to identify candidates in the short brightening phase, while also needing the depth to catch faint, extincted sources in the Galactic Plane. In addition, optical fields are much more crowded at typical outburst magnitudes compared to the X-ray sky and X-ray outbursts. As a result, additional contextual data, such as the lightcurve history, and prompt followup are needed to identify outbursts as LMXBs early in the outburst cycle.

The X-ray Binary New Early Warning System (XB-NEWS) collaboration (Russell et al., 2019) uses observations from the Las Cumbres Observatory to monitor known X-ray binaries and has made the first detection of several LMXB outbursts (Baglio et al., 2022; Pirbhoy et al., 2020; Saikia et al., 2023).

This dedicated program ensures consistent monitoring of known XRBs over long periods, but requires dedicated observations and data processing. Additionally, its narrow-field targeted observations are not able to discover outbursts from previously unknown XRBs.

Optical synoptic surveys provide an alternative means of discovering outburts from both known and new LMXBs. The Zwicky Transient Facility (ZTF; Bellm et al., 2019a; Dekany et al., 2020; Graham et al., 2019) images the northern sky down to $\sim$21 mag at a cadence of 1–3 days (Bellm et al., 2019b). The high cadence and depth of ZTF combined with its real-time alert system (Patterson et al., 2019), enables multiple detections of LMXBs during the fast rise phase of outburst and quick investigation of the candidate sources, and motivates this study to find optical outbursts of LMXBs. The easily accessible lightcurve history in ZTF also enables us to eliminate a large number of contaminant sources, such as cataclysmic variables (CVs), by examining the historical outburst behavior and duty cycle of candidate sources.

For identification of outbursts from known LMXBs in ZTF, we make use of a watchlist to notify us of any activity from positions of sources in the Ritter and Kolb Ritter & Kolb (2003b), BlackCAT (Corral-Santana et al., 2016), and WATCHDOG (Tetarenko et al., 2016) catalogs. This watchlist, implemented using the ANTARES broker (Matheson et al., 2021), led to the discovery of outbursts from XTE J1859+226 (Bellm, 2021a; Bellm et al., 2023) and Swift J1357.2−0933 (Bellm, 2021b).

In this work, we focus on searches for previously-unknown LMXBs using the ZTF alert stream. We describe a live nightly outburst search pipeline which crossmatches ZTF alerts with catalogs of X-ray sources to narrow down the number of candidates considered. We also perform this search over 4 years of archival alert data. In section 2, we describe our methodology for identifying candidates. In section 3, we present the results of our search, which includes recoveries of known LMXB outbursts over this timespan. In section 3, we estimate the percentage of galactic LMXBs are visible to our pipeline. In section 4, we conclude with a discussion of our pipeline, and the implications of our results for discovery of LMXBs in future surveys, such as the Vera C. Rubin Observatory's Legacy Survey of Space and Time (LSST; Ivezić et al., 2019).

2 Methods

2.1 The ZTF Alert Stream

The alert stream is a data product provided by the Zwicky Transient Facility. An automated pipeline detects transient and variable sources by differencing nightly images and coadded reference images and identifying any sources that appear in the difference images[1] above a SN > 5 (Masci et al., 2019). Candidates are packaged with metadata, detection history, and image cutouts into alerts. The ZTF alert distribution system (ZADS; Patterson et al., 2019) uses Kafka to stream these alerts out in near real time, enabling rapid followup after identification. The median number of ZTF alerts per observing night for all programs is 363,000, but is highly variable, and can exceed 1M in a single night when observing in the Galactic plane.

Galactic variables frequently appear in both reference and science images, so to find the total apparent magnitude we add the reference and difference fluxes. The apparent photometric magnitudes for each source are determined by adding (or subtracting, in the case of a negative source in the difference image) the PSF-fitted photometry to the reference image photometry. Sources that are too close in brightness to the reference image may not pass the 5-sigma threshold for triggering an alert and show up in the alert history as a nondetection. We determine the limit of nondetections by averaging the upper and lower bounds for the nondetection, which are found by adding and subtracting the difference image limiting magnitude from the reference magnitude. Adding nondetections to the lightcurve history gives greater temporal coverage to the outburst identification algorithm and provides a level of comparison between the outburst and quiescent states.

2.2 Live Search Pipeline

Consuming Alerts

The live search over all alerts in the alert stream covered in this paper begins on February 24th, 2021 and ends September 21st, 2022. ZTF provides access to alerts through a number of community brokers[2] which consume the public stream and enable users to filter, query, and otherwise interact with the alerts. However, we consume the alert stream directly from

[1] https://irsa.ipac.caltech.edu/data/ZTF/docs/ztf_explanatory_supplement.pdf

[2] e.g., ANTARES (Matheson et al., 2021); Lasair (Smith et al., 2019); ALeRCE (Förster et al., 2021); AMPEL (Nordin et al., 2019); Fink (Möller et al., 2021); Pitt/Google (http://pitt-broker.readthedocs.io)

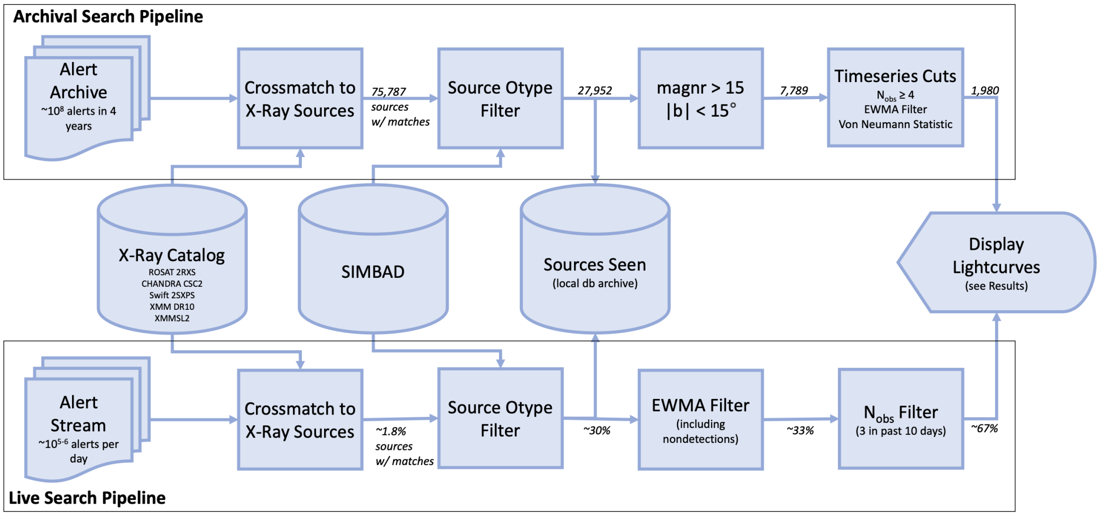

Figure 2.1: Flowchart showing how packets from the alert stream or alert archive are processed by our pipeline. We examine lightcurves of candidates passing all cuts by eye and further investigate their historical observations by ZTF and other surveys.

the ZADS system for greater flexibility and control over the filters and cuts in our search for LMXBs[3]. The filters and cuts on the alert stream are diagrammed in figure 2.1.

We eliminate sources with a deep real bogus score (Duev et al., 2019) under 0.8, as well as any packets with nearby known solar system objects. The sources passing this initial cut are then crossmatched to positions of known X-ray sources.

X-ray and SIMBAD Crossmatch

In order to narrow down the number of candidates considered, we first crossmatch all alerts with positions of previously catalogued X-ray sources using the given spatial uncertainties in the catalogs as the crossmatch radius. These sources are compiled from 5 X-ray surveys listed in table 2.1: ROSAT 2RXS (Boller et al., 2016), Chandra CSC2 (Evans et al., 2010), Swift 2SXPS (Evans et al., 2020), XMM DR10 (Webb et al., 2020a), and XMMSL2 (Warwick et al., 2012). We crossmatched the X-ray source positions to SIMBAD to remove known extra-galactic sources, such as AGN, as well as other previously-identified X-ray emitting sources that are not X-ray Binaries. We then created a unified X-ray dataset combining all 5 catalogs. The ROSAT 2RXS and XMMSL catalogs provide comprehensive sky coverage at the expense of poor localization, and roughly 15% of sources in these catalogs overlap with better localized sources in the Chandra and Swift catalogs. The total number of X-ray sources we crossmatch against is 848651.

ZTF alerts within the positional uncertainty of an X-ray source are flagged as matches and saved for further analysis. Since the positional uncertainty of candidates from ZTF is usually smaller than their matched X-ray counterparts, we again crossmatch to SIMBAD to

[3] https://github.com/dirac-institute/alert_stream_crossmatch

Observatory	Catalog	Energy Range	Median 1σ Localization	Sky Coverage	Number of Sources
Rosat	2RXS	0.1–2.4 keV	15.7 arcsec	100%	135,118
XMM	XMMSL2	0.2–12 keV	4.2 arcsec	84%	29,393
Swift-XRT	2SXPS	0.3–10 keV	2.7 arcsec	9.1%	146,768
XMM	4XMM-DR10	0.2–12 keV	1.5 arcsec	3.0%	575,158
Chandra	CSC 2.0	0.1–10 keV	0.6 arcsec	1.3%	317,167

Table 2.1: X-ray catalogs used for crossmatching in this work. Citations are as follows: 2RXS (Boller et al., 2016), XMMSL2 (Warwick et al., 2012), 2SXPS (Evans et al., 2020), 4XMM-DR10 (Webb et al., 2020a), CSC 2.0 (Evans et al., 2010)

eliminate any unwanted contaminants. Sources passing the SIMBAD cut are saved into a SQLite database along with photometric and nondetection data.

Time Series Metrics

We use photometric magnitudes to calculate our timeseries features. Objects with reference magnitudes brighter than 15 mag are eliminated, since these sources are near ZTF's saturation limit and are unlikely to be undiscovered LMXBs. Additionally, we eliminate the 0.5% most uncertain observations (photometric errors greater than 0.5 mag), which are usually the result of problems in the data quality. This eliminates a number of spurious observations.

We then calculate an 8-day ($\tau = 8$) exponentially weighted moving average (EMA) on the apparent magnitudes and nondetection limits:

$$\begin{gathered} EMA(t) = f * EMA(t_p) + (1 - f) * mag(t) \\ f = \exp\{-(t - t_p)/\tau\} \end{gathered} \tag{2.1}$$

Where t is the time of detection and tp is the time of the previous detection. The EMA is a trailing metric: during an outburst, the photometric magnitude will be brighter than the EMA at the same time, leading to a positive difference between the 8-day EMA and the photometric magnitude. For an outburst, we expect this difference to be positive for at least 8 days. We use a 4-day rolling average of this EMA difference as our metric for outburst, selecting all objects where this metric exceeds 0.25 for at least one observation. We then sort all candidates from the previous 10 days by the maximum value of this metric and visually inspect the lightcurves.

The EMA cut typically provides on order 100 lightcurves per day. We examine the complete ZTF photometric history of lightcurves passing the EMA cut. This allows us to eliminate a large number of cataclysmic variables, which are by far the most common contaminant. The recurrence time and outburst duration of CVs (Coppejans et al., 2016) are both generally much shorter than those for LMXBs (Tetarenko et al., 2016). Additionally, CV outbursts, which are much less luminous than LMXB outbursts, tend to be closer and therefore much less extincted (i.e red) than LMXB outbursts.

Candidates exhibiting a lack of outburst history or long-duration outbursts with long recurrence times are examined further using the ZTF forced photometry service. We also check for past observations in X-ray by *Swift* XRT and BAT, in SIMBAD for publications and references, and for observations and spectra by other surveys such as SDSS.

We follow up sources by triggering spectroscopic observations in the optical using the 3.5m telescope at Apache Point Observatory (APO), as well as in the X-ray using a *Swift* ToO. The spectroscopic followup enables us to identify the presence of double-peaked Balmer emission lines. While these lines are also present in the spectra of cataclysmic variables (CVs), black hole binaries have broader emission lines than CVs at a given orbital period (Casares & Torres, 2018). The full width half maximum (FWHM) of these emission lines can both serve as a diagnostic and be used to estimate the mass ratio of the compact object to the companion star (Casares, 2016).

2.3 Archival search

In addition, we also ran a search for outbursting LMXBs over 4 years of archived ZTF alert data. Similar to the live search, archived alerts were first crossmatched against our combined X-ray catalog, with matches then crossmatched to SIMBAD to eliminate extragalactic and other contaminant sources. We then implemented the same cuts on reference magnitude and observation uncertainty. We also required each candidate to have at least 4 observations in a single filter over a stretch of 28 days.

Candidates that passed these basic cuts were then subjected to cuts based on timeseries features. We again calculate the EMA metric described in 2.2, as well as the Von Neumann statistic:

$$\eta = \frac{1}{(N-1)\sigma^2} \sum_{i=1}^{N-1} (m_{i+1} - m_i)^2 \tag{2.2}$$

The Von-Neumann statistic assesses the smoothness and stability of the lightcurve by averaging the square differences of consecutive points and dividing by the variance. The least interesting candidates never undergo a significant outburst, leading to a very small value for the Von-Neumann statistic. We exclude sources where the Von-Neumann statistic is less than 0.004.

3 Results

3.1 Live Search Results

We identified two LMXB candidates in outburst using our live search pipeline. Figure 2.2 presents the lightcurves and outburst metrics associated with these two sources around the time of discovery. Table 2.2 summarizes these sources along with sources identified in an archival search (§3.2).

AMXP MAXI J1957+032

MAXI J1957+032 is an accreting milisecond puslsar (Sanna et al., 2022) that was identified in our live search pipeline as ZTF19acerbwo on June 20th, 2022. This outburst was previously

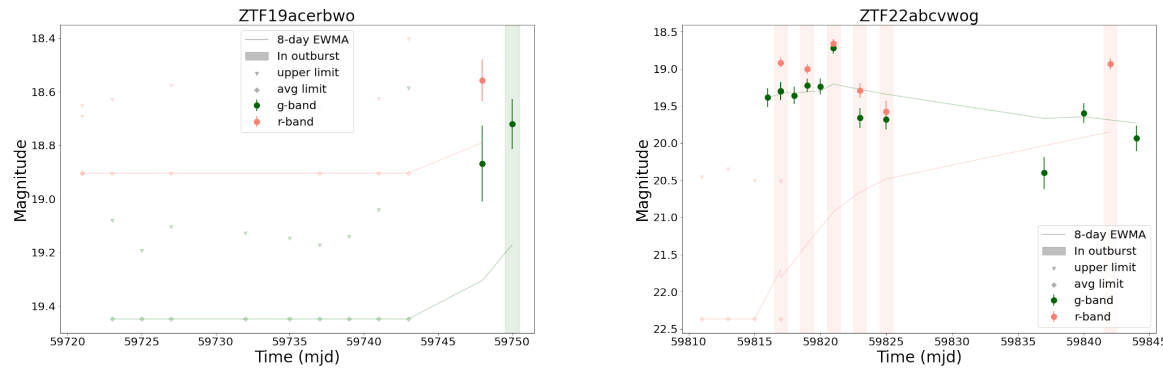

Figure 2.2: Two objects found in our live search. The left plot shows an outburst of MAXI J1957+032, a known LMXB. The right plot shows the outburst of Swift J1943.4+0228, an LMXB candidate not observed for 10 years. The red and green colors correspond to observations taken in the ztf-r and ztf-g bands respectively. The lightly plotted lines show the 8-day EMA and the vertical shading indicates observations meeting our outburst metric (these are described by pale grey in the legend).

observed and reported by MAXI on June 18th, 2022 (Negoro et al., 2022). Using the ZTF forced photometry service, we found this source was first observed by ZTF on the same day as the MAXI report (Wang et al., 2022). Since the source appeared to be already fading in optical past the followup capabilities of APO, we did not trigger further followup.

Swift J1943.4+0228

Swift J1943.4+0228 is an X-ray transient source first observed in outburst by *Swift* in April 2012 by the Burst Alert Telescope (BAT) (Krimm et al., 2013) and subsequently not detected again until it was detected to be in outburst by our pipeline on September 6, 2022 (MJD 59828) as ZTF22abcvwog after having begun an outburst on August 26th (MJD 59817). Ongoing monitoring revealed two more reflares back up to a brightness of $m_r \approx 18.5$ beginning on September 18th, 2022 (MJD 59840), each lasting for between 20-40 days. These reflares are visible in the forced photometry lightcurve in figure 2.3. We observed this outburst with the KOSMOS spectrograph (Martini et al., 2011) on the 3.5m telescope at APO and were unable to obtain a signal in 40 minutes of observation.

The original *Swift* detection and monitoring revealed a 2 month long decay period in the soft X-rays. We obtained a detection with *Swift* X-ray Telescope (XRT) of around $0.076 \pm 0.01\,\mathrm{counts\,s^{-1}}$ count rate, far below the previous 2012 XRT peak detection of $1.4 \pm 0.04\,\mathrm{counts\,s^{-1}}$, indicating that this event may be a failed outburst (Alabarta et al., 2021). Additionally, the hardness ratio of our detection was 2.82 ± 0.88, harder than the previous outburst, which reached 1.77 ± 0.08, as shown in the hardness intensity diagram in figure 2.4.

Using the catalog from Green et al. (2019), we estimate the distance to the system to be $1.2 \pm 0.3\,\mathrm{kpc}$. Combining this with our measured X-ray flux, we use WebPIMMs and a power

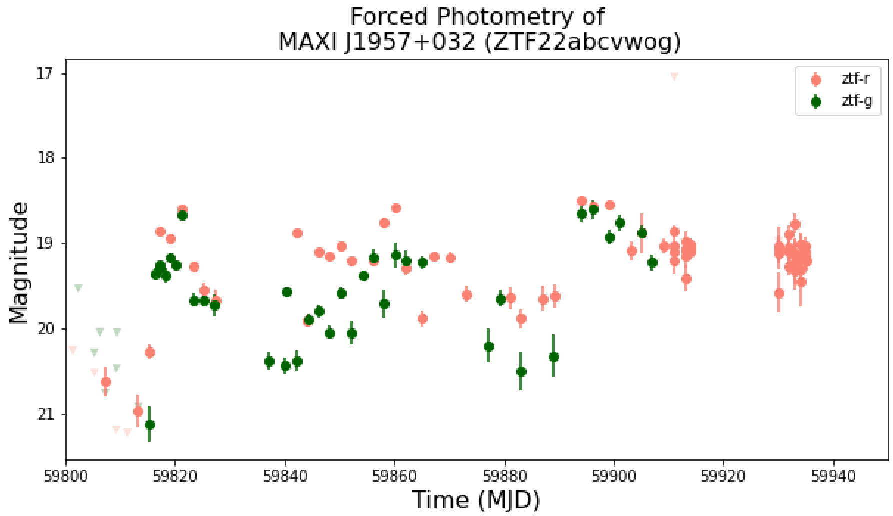

Figure 2.3: ZTF22abcvwog (Swift J1943.4+0228) lightcurve produced by the ZTF forced photometry service showing no previous detections by ZTF, as well as a reflares on MJD=59840 and MJD=59890.

law model of the source with photon index of 2 and column density of $1.9 \times 10^{21}\mathrm{cm}^{-2}$ (Rau et al., 2012) to estimate the luminosity of the source to be $1.7 \times 10^{33}\,\mathrm{ergs\,s^{-1}}$. The calculated luminosity of the 2012 ($1.4 \times 10^{34}\,\mathrm{ergs\,s^{-1}}$) and 2023 outbursts are more characteristic of a cataclysmic variable than an LMXB. However, the long intervals between activity and the X-ray lightcurve of the source, which took over two months to fade appeared similar to a hard-only outburst of an LMXB, making this source worth monitoring for future activity.

3.2 Archival Search Results

Running the archival search from June 1, 2018 to July 14th, 2022, we crosmatched 75,787 ZTF sources to objects in our combined X-ray catalog. Of these sources, 27952 were left after making the SIMBAD crossmatch cut. After requiring the reference magnitude of the candidate to be 15th mag or fainter and a galactic latitude of less than 15deg, there were 17966 and 7789 sources remaining, respectively.

We then made further cuts on lightcurve features. First, we required at least 4 observations in a single filter, in any 28-day stretch. This narrowed our sample down to 3730 sources. We also required at least 4 observations termed “in outburst”, with the EMA metric 2.1 greater than 0.25 at least 3 times in a 28-day period, resulting in 2584 candidates remaining. Finally, we required a Von Neumann statistic of at least 0.004 in at least one of the filters, a threshold that we selected after calculating this metric for known X-ray binary outbursts found in the live search, as well as XTE J1859+226 (ZTF21aagyzqr, Bellm, 2021a) and Swift J1357.2−0933 (ZTF19aanxwrq, Bellm, 2021b). Examples of lightcurves passing all cuts are given in figure 2.5.

After visual inspections and literature searches for lightcurves displaying characteristics of LMXB outbursting, we recovered 3 known LMXBs in the alert archives: XTE J1859+226

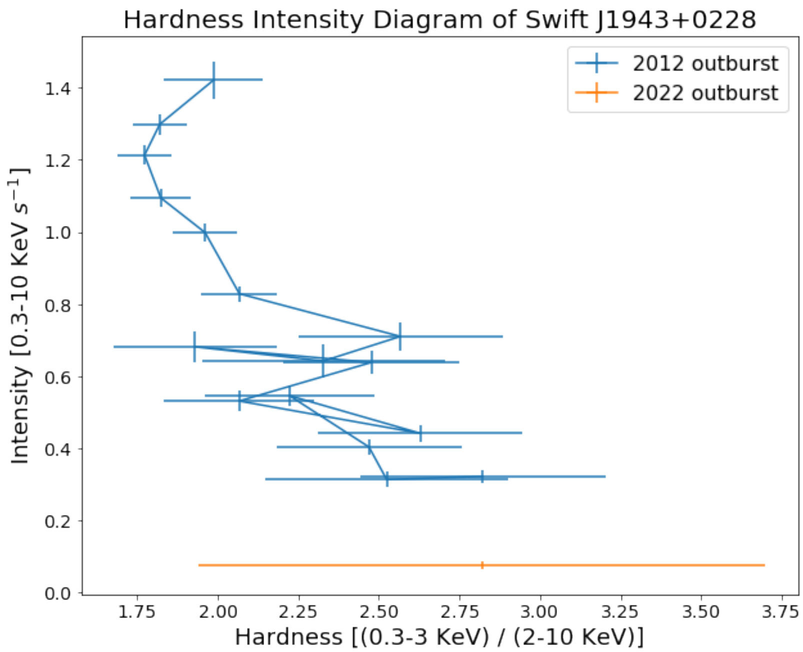

Figure 2.4: Hardness v. intensity of the 2012 and 2022 outbursts of Swift J1943.4+0228. It appears that the 2012 outburst never transitioned into the soft state. The 2022 outburst is barely detected and also harder than the 2012 outburst.

(ZTF21aagyzqr; Bellm, 2021a, Bellm et al., 2023), Swift J1911.2+0036 (ZTF18accedau), and MAXI J1807+132 (ZTF19abvioim; Shidatsu et al., 2019). One source from the live search, Swift J1911.2+0036, was also recovered in the archival search. We also discovered 3 sources (ZTF20abmxtnh, ZTF19acylwtd, and ZTF19aabgjuf) displaying short outbursts peaking above the limiting magnitude of ZTF; these are shown in figure 2.6 and discussed below.

Additionally, one known LMXB, Swift J1357.2−0933 (ZTF19aanxwrq), was excluded due to the galactic latitude cut.

3.3 ZTF20abmxtnh

This source is classified as a Type Ia supernova (SN2020qbw) in TNS (Dahiwale & Fremling, 2020). The location at galactic latitude 9.58°, as well as the relatively short period of time above the ZTF limiting magnitude enabled it to pass our cuts and to be flagged as a candidate. This source peaked at 18.73 mag in g-band and 18.83 mag in r-band two days later after the first ZTF observation. It was visible to ZTF over a period of roughly 3 months. The lightcurve shows distinct color evolution, with the r-band fading slower than g-band. The X-ray counterpart for this source was Swift 2SXPS J194138.3+423721. Upon examining the image cutouts, it appears likely that the g-band "quiescent" flux is actually contamination from the host galaxy.

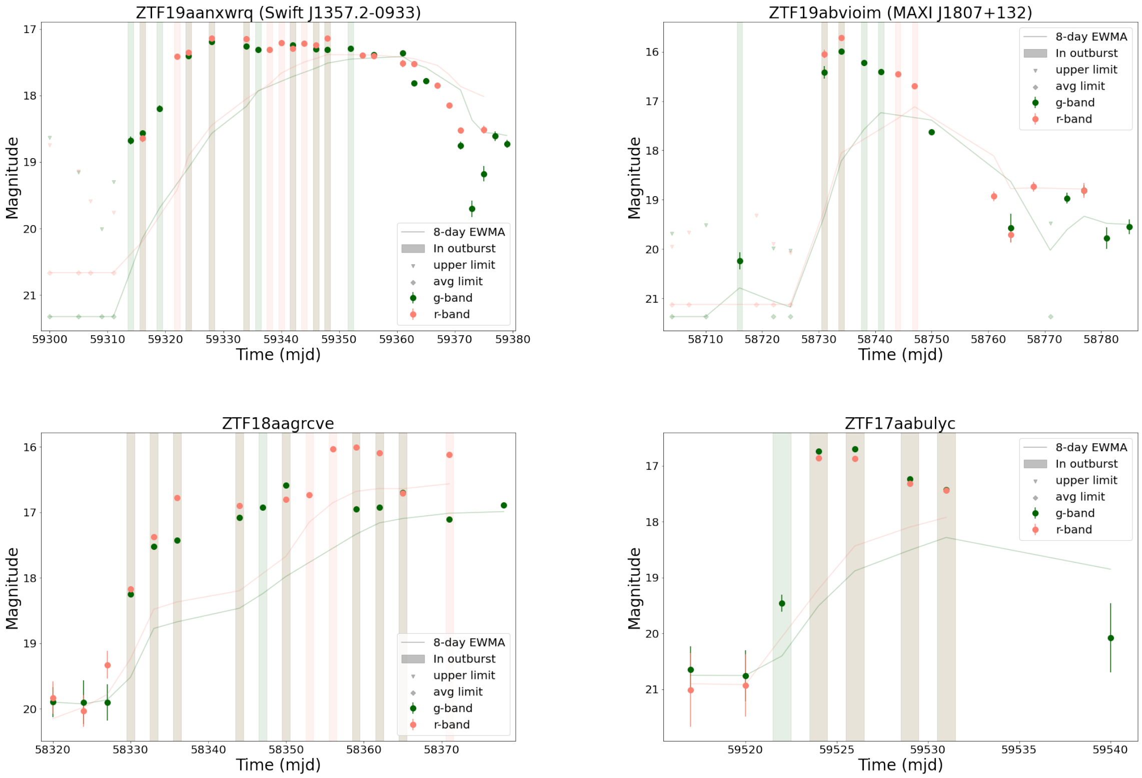

Figure 2.5: Examples of candidates found in the archival search. Both ZTF19aanxwrq and ZTF19abvioim are known LMXBs (Swift J1357.2−0933 and MAXI J1807.2+132). ZTF18aagrcve displays a rise and sustained outburst profile similar to that of LMXBs; however, a literature search revealed it to be a polar. ZTF17aabulyc is a cataclysmic variable, the short duration of outburst and large duty cycle from its photometric history confirm this.

3.4 ZTF19acylwtd

This source peaked at 17.11 mag in r-band and the total duration of the outburst was around 30 days. The quiescent magnitude of this source was measured by PS1 to be 20.06 ± 0.004 in the r-band and 21.20 ± 0.05 in the g band (Chambers et al., 2016). The X-ray counterpart for this source was Swift 1XPS J070927.3−110211. Using a distance of 5 kpc (Bailer-Jones et al., 2021), we estimate the X-ray luminosity between 0.5 and 7 keV of the source to be $2 \times 10^{33}\,\mathrm{ergs\,s^{-1}}$. Based on the quiescent magnitude and X-ray luminosity, this is likely a CV.

3.5 ZTF19aabgjuf

This source peaked at 17.95 mag in r-band and the total duration of the outburst lasted around 15 days. The quiescent magnitude of this source was measured by PS1 to be 20.26 ± 0.02 in the r band and 21.60 ± 0.07 in the g band (Chambers et al., 2016). Two other potential outbursts with two points in both r and g-band on the rise are seen on the edges of gaps in photometric data. The X-ray counterpart to this object was found by *Chandra*: CSC2 J205921.2+543035. We estimate the X-ray luminosity of this source to be 1×10^{32} erg s^{-1}, assuming a distance of 4 kpc. Based on the quiescent magnitude, recurrence times, and X-ray luminosity, this source is also likely a CV.

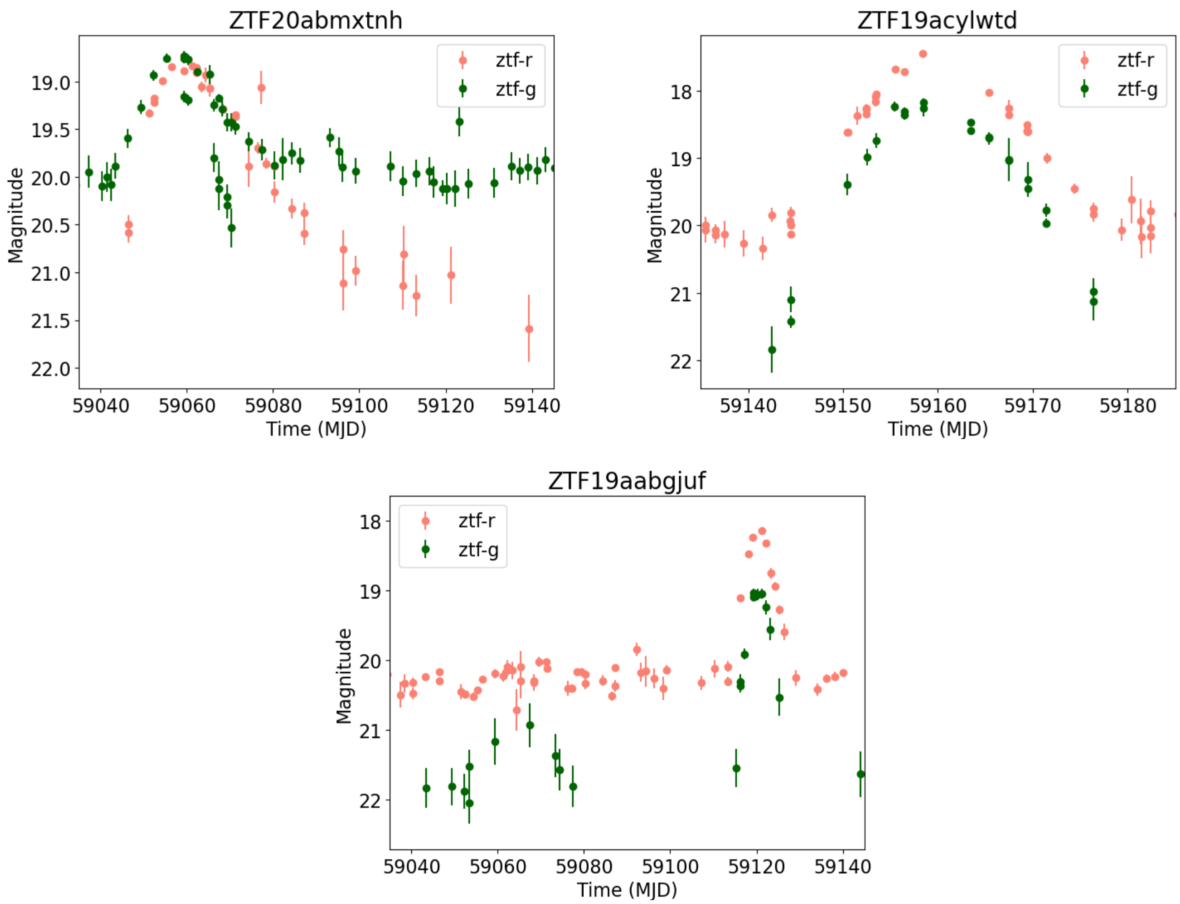

Figure 2.6: 3 sources displaying outbursts with quiescent magnitudes below the ZTF alert pipeline detection limit. These lightcurves were obtained using forced photometry and we relaxed the required signal to noise from 5 to 3.

4 Selection Effects and Estimating the Population of Galactic LMXBs

We estimated the proportion of expected outbursting systems discoverable by our pipeline by simulating a population of Galactic LMXBs with a bulge/disk/halo distribution (Grimm et al., 2002b) and subjecting the simulated population to a selection function approximating the cuts of our search. Each simulated object is assigned parameters such as recurrence

ZTF id	Source Name	Source Type	Date Detected (ZTF)	Peak Magnitude
ZTF19acerbwo	MAXI J1957+032	LMXB	Jun-20-2022	19.1
ZTF22abcvwog	Swift1943+0228	LMXB?	Aug-26-2022	18.5
ZTF19abvioim	MAXI J1807+132	LMXB	Sep-05-2019	15.7
ZTF21aagyzqr	XTE J1859+226	LMXB	Feb-04-2021	18.5
ZTF18accedau	Aql X-1	LMXB	May-05-2022	16.9
ZTF19aatqkhi	Swift J0636.6+3536	CV	Feb-06-2021	17.4
ZTF20abmxtnh	SN2020qbw	SN1a	Jul-16-2020	18.7
ZTF19acylwtd	–	CV	Oct-28-2020	17.5
ZTF19aabgjuf	–	CV	Sep-24-2020	18.4

Table 2.2: Sources examined in detail from the live and archival searches.

time, mean outburst duration, and duty cycle drawn from 45 sources from the WATCHDOG catalog from (Table 8; Tetarenko et al., 2016) of transient black hole X-ray binaries. [4] Using bootstrapping, we obtain a maximum likelihood estimate of the number of galactic LMXBs based on our observation of 4 outbursting objects. We do this by subsampling a number N of simulated objects, and passing the subsample through a selection function that replicates our pipeline, including limits due to the survey depth and area of ZTF, the exclusion of ZTF alerts without an X-ray counterpart, and the likelihood of an outburst during our 4 year search window.

4.1 ZTF Survey Cut

We used ZTF pointing data to determine the number of simulated objects within ZTF fields (38.9%) that were observed more than 100 times (37.8%). We calculated the extinction to each simulated position using three-dimensional dust maps (Green et al., 2019; Lallement et al., 2019), assumed a fiducial outburst brightness increase of 6 magnitudes based on BlackCAT outburst magnitudes and distances, and used the simulated distances and absolute magnitudes to calculate the apparent magnitudes of each source. Absolute magnitudes were simulated using the orbital period-magnitude relation from Casares (2018), and by sampling known orbital periods and perturbing them by up to 50%. Using a fiducial limiting magnitude of $m = 20.5$ for ZTF, we find that around 75% of outbursting systems reach a brightness greater than 20.5 mag. Additionally, we note that the galactic latitude cut ($|b| \leq 15\,\mathrm{deg}$) in the archival search excluded less than 4% of the simulated sources, although our model for the spatial distribution of LMXBs (Grimm et al., 2002b) may underestimate the number of LMXBs in the halo, due to natal kicks (Gandhi et al., 2020).

4.2 Cut on Sources with X-ray Counterparts

Our decision to require a crossmatch between each alert to a catalog of X-ray sources allows us to investigate a more tractable number of candidates. However, the aggressiveness of

[4] We excluded the two long term transient sources (SWIFTJ1753.5−0127 and GRS1915+105) and two sources with high mass companions (SAXJ1819.3−2525 and XTEJ0421+560).

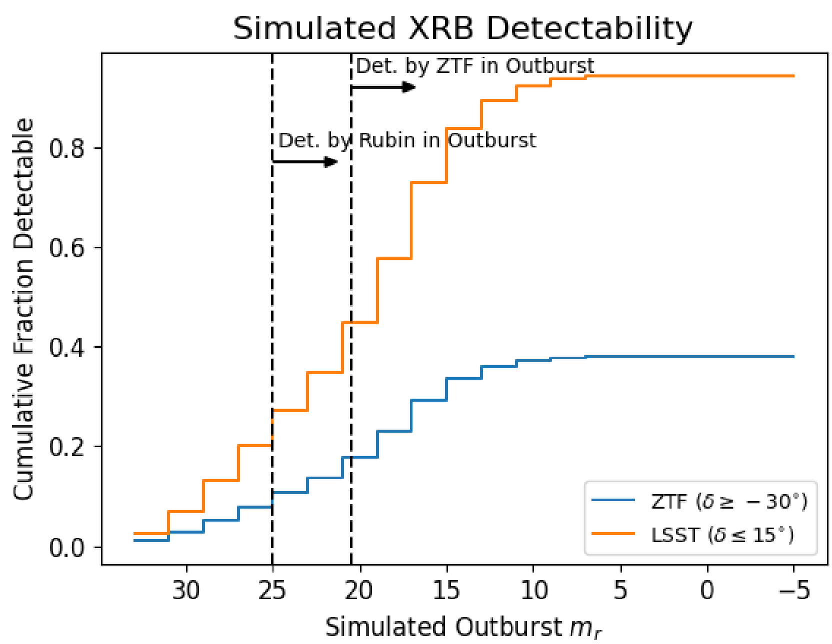

Figure 2.7: Cumulative fraction of simulated LMXBs discoverable by the ZTF and LSST surveys accounting for distance to each object, extinction using 3D dust maps (Green et al., 2019; Lallement et al., 2019), and location of the observatory. The single-image limiting magnitudes for ZTF and for Rubin are plotted as vertical dashed lines. Almost all simulated outbursting XRBs are observable by Rubin Observatory, while only about 39% are expected to be in the ZTF survey footprint.

this cut means that we may be excluding many sources that have never been detected by any X-ray survey. To obtain an order of magnitude estimate of the number of LMXBs potentially eliminated by this cut, we assumed a quiescent X-ray luminosity of $10^{31}\,\mathrm{ergs\,s^{-1}}$ and an outburst luminosity of $10^{38}\,\mathrm{ergs\,s^{-1}}$ and calculated the X-ray flux from each source in quiescence and outburst, using the simulated distances. We then used WebPIMMs to estimate the counts per second for each simulated source at quiescence and in outburst, while accounting for extinction. Finally, we estimated the percentage of sources expected at a signal to noise ratio of 5 for each of the catalogs in our crossmatch (table 2.1) by sampling the exposure times in each catalog and multiplying by the extinction-corrected flux to estimate the total counts detected per simulated source. We use η to represent the percentage of sources expected, for each of the 5 catalogs, for sources in both quiescent and outburst states.

While sources in outburst are almost always bright enough to be observed by each instrument, most sources are in the outburst state only a small fraction of time. This fraction, known as the duty cycle, is observed to be anywhere between less than 1% to over 50% (Tetarenko et al., 2016), with a median in the WATCHDOG database of black hole XRBs of 2.7% and a mean of 10%. We use Monte Carlo sampling to simulate whether each system is in outburst or quiescence and then use Monte Carlo sampling again to simulate whether the system is detected and cataloged, where η describes the probability of discovery. This sampling procedure is repeated for each of the 5 catalogs. A simulated source is tagged as passing this cut if it appears in any one of the catalogs. Using this method, we estimate that around 8.8% of galactic LMXBs are present in our unified X-ray catalog (see table 2.3).

By using sampled parameters from the WATCHDOG database, we are assuming that the outburst parameters (mean outburst duration, duty cycle, and recurrence time) of the known sources are representative of undiscovered LMXBs, including systems with neutron stars. This is unlikely because of observational biases–sources that are in outburst more often and more recently are more likely to be discovered. Additionally, many of the WATCHDOG sources have only one recorded outburst, meaning that the duty cycle and recurrence times are upper limits. To account for this, we also run this step of the selection function using the median duty cycle, which could be more representative of the galactic population. Using this method, we estimate that around 4.4% of galactic LMXBs are present in our unified X-ray catalog.

4.3 Outbursting LMXBs

We then estimate the proportion of LMXBs that undergo an outburst in any 4 year period using the WATCHDOG catalog of known black hole XRBs (Tetarenko et al., 2016), calculating the number of expected outbursts for each simulated object detectable in a $T = 4\,\mathrm{year}$ period using the recurrence time:

$$Expected(N_{outbursts}) = \frac{T + t_{outburst}}{t_{recurrence}} \tag{2.3}$$

where T is the length of the archival search (4 years). Since many of the WATCHDOG sources have recurrence times longer than 4 years, only a fraction of the sources will undergo a state change in our data. We can then calculate the probability of at least one outburst using the cumulative distribution function of the Poisson distribution with $\lambda = \mathbb{E}(N_{outbursts})$:

$$P_{outburst} = 1 - P(0) \tag{2.4}$$

Again using Monte Carlo sampling, we can simulate the sources that undergo at least one outburst during the 4 year period.

We assume the X-ray outburst parameters are representative of the optical outbursts. However, there is evidence that short optical outbursts can happen without a state change or full X-ray brightening, such as in misfired or failed outbursts (e.g., Alabarta et al., 2021; Baglio et al., 2022; Bellm et al., 2023) and possibly the outburst of Swift J1943+0228 reported in this paper. As a result our cut here may be too stringent, as systems may undergo optical outburst more frequently, particularly as activity without the substantial X-ray brightening needed to trigger X-ray monitors.

4.4 Estimate of the Galactic Population

Finally, we performed a Monte Carlo simulation to estimate the number of interacting LMXBs in the galaxy consistent with our observations. We do this by taking 10,000 samples of size N from our simulated dataset, passing them through the cuts described above, and finding the percentage of samples returning 4 sources.

Using the sampled outburst parameters, we estimate that 1.6% of sources in outburst are detectable. Accounting for the duration of our survey, we find that we detect 0.76% of the total population of LMXBs and obtain an estimate of the number of sources with a 95% confidence interval (CI) of 530^{+810}_{-320}. This estimate is lower than current estimates of the number of LMXBs in the galaxy. The 2016 BlackCAT survey (Corral-Santana et al., 2016) estimates a total of 1300 galactic BHXBs, implying around 4000 LMXBs with either black hole or neutron star primaries, assuming that there are roughly double the number of neutron star LMXBs as black hole XRBs (Bahramian & Degenaar, 2022).

If we substitute the median duty cycle instead of the sampling this parameter, we estimate that 0.79% of outbursts are detectable, meaning we detect 0.012% of the galactic population, giving to a total of 3390^{+3980}_{-1930} galactic LMXBs. This appears to be more in line with current estimates. However, because we have only 4 confirmed objects recovered by the pipeline, our results are accompanied by large uncertainties. The large difference between the two estimates is also due to the frequency of expected outbursts, with many fewer outbursts expected for an undiscovered population with the fiducial duty cycle.

4.5 Discovery of Outbursts in Optical vs. X-ray

While accretion outbursts of LMXB are intrinsically much energetic at X-ray wavelengths, the greater single epoch sensitivities of optical observatories means that the flux from many outbursting LMXBs first exceed the sensitivity limit of an optical survey than an all sky X-ray monitor. Using 28 black hole XRBs from the BlackCAT catalog (Corral-Santana et al., 2016) with peak X-ray flux counts, optical or IR (OIR) peak outburst magnitude, and distance estimates, we calculated both the X-ray and OIR luminosities, correcting for extinction.

We then fit a 2-component Gaussian mixture model to the resulting set of luminosities and sampled this model additional X-ray and OIR luminosities, which we combined with distances and extinctions to obtain a simulated set of outburst fluxes in both X-ray and OIR.

Taking a ZTF limiting AB magnitude of 20.5 and a single orbit MAXI sensitivity of 10 milliCrab between 2–30 keV, we calculated the relative sensitivities of these observatories to be 3.3×10^{-14} ergs s^{-1} cm^{-2} and 1.21×10^{-10} ergs s^{-1} cm^{-2}. We assume that if the OIR flux to X-ray flux ratio is greater than the MAXI to ZTF flux ratio, than the source will first exceed the sensitivity of ZTF before MAXI. Using this metric, we estimate 21% of outbursts would first be visible in the optical. This estimate is likely conservative: we assume that the ratio of optical flux to x-ray flux at the peak of the outburst is similar to the ratio during the rise, while models for accretion disk outbursts may suggest that the optical radiation begins to increase before the X-ray increase (Hameury, 2020; Russell et al., 2019). The Einstein Probe is currently slated for launch by the end of 2023 and carries an ASM with an order of magnitude sensitivity increase compared to current ASMs (Chen et al., 2022). Comparing this upcoming probe to LSST, and assuming a sensitivity 10x that of MAXI, we calculate that about 27% of outbursts would first be detectable to LSST in the optical.

Additionally we ran ZTF forced photometry on all outbursting LMXBs in the past 5 years with a known optical counterpart. Out of the 11 LMXBs with ZTF observations, we find that 5 of the sources (Swift J1858.6−0814, Swift J1357.2−0933, Aquila X-1, XTE J1859+226, MAXI J1807+132; see Figure 2.8) had at least one detection by ZTF before the time of first detection in X-ray, and that 3 of these sources (MAXI J1820+070, Swift J1910.2−0546, MAXI J1957+032; Figure 2.9) showed concurrent optical and x-ray outbursts. Three sources (4U 1730−22, MAXI J1816−195, IGR J17591−2342; Figure 2.10) showed no visible increase in optical brightness.

4.6 Optical Discovery of LMXB Outbursts in the Rubin Era

As shown in figure 2.7, due to the location of Palomar in the Northern Hemisphere as well as the moderate limiting magnitude of ZTF, we only expect $< 40\%$ of outbursting LMXBs to be present in ZTF data. We can estimate the expected proportion of outbursting systems discoverable by Rubin's LSST using survey cadence simulations (Bianco et al., 2022; The Rubin Observatory Survey Cadence Optimization Committee, 2023), plus our simulation of XRB positions following Johnson et al. (2019) and Grimm et al. (2002b). The location of Rubin Observatory in the Southern Hemisphere means that it will be much better positioned to observe the Galactic Bulge, and will observe approximately 86% of the outbursts. Using an XRB metric[5] and v3.0 of the LSST baseline observing cadence (The Rubin Observatory Survey Cadence Optimization Committee, 2023), we simulated 10,000 outbursts following a fast rise exponential decay template (Chen et al., 1997) and estimate that 43.3% of outbursts will be detectable in 10-year survey time of LSST by Rubin.

Much of the improvement (in the previous section we estimated our search using ZTF to detect 2.4% and 1.2% of all outbursts, depending on the assumptions of the distribution of the duty cycle of undiscovered objects) is due to the elimination of the X-ray counterpart cut, which eliminates between 91-96% of LMXBs. Using equation 2.3 we estimate 26% of

[5] https://github.com/lsst/rubin_sim/blob/main/rubin_sim/maf/maf_contrib/xrb_metrics.py

Observatory	Catalog	Sky Coverage	$\eta_{quiescent}$	$\eta_{outburst}$
Rosat	2RXS	100%	0.0025%	99.999%
XMM	XMMSL2	84%	0.013%	37.4%
Swift-XRT	2SXPS	9.1%	0.14%	100%
XMM	4XMM-DR10	3.0%	17.8%	100%
Chandra	CSC 2.0	1.3%	1.6%	99.2%

Table 2.3: Estimate of percentage of galactic LMXBs that are expected (η) in each of the major catalogs we crossmatch to.

systems to undergo at least one outburst in a ten year period. As a result, we expect LSST to discover outbursts from approximately 10% of all galactic LMXBs, i.e. roughly 400 objects.

Notably, most of the outbursts we observed and recovered in the live and archival searches were shorter (on order weeks) than typical outbursts which can last for months to years. The duration of our search of roughly 4 years means that we will preferentially observe sources with shorter duty cycles, which tend to correlate with shorter outburst duration.

5 Discussion

The previous section demonstrates that requiring a candidate to have a crossmatched X-ray source is a fairly stringent criteria. Our order of magnitude estimate of the percentage of LMXBs catalogued by one of the 5 X-ray surveys we crossmatch against is 4.4% to 8.9%, meaning our pipeline excludes more than 9 out of 10 potential candidates. One example of an LMXB candidate missed by both our live and archival searches is ZTF19acwrvzk (AT2019wey; Yao et al., 2021), which did not have a known X-ray counterpart at the time of detection. We also have implemented a pipeline without a crossmatching criteria, instead using EMAs of different exponential decay timescales to detect outbursting events, as well as additional timeseries features to make cuts on both the live alert stream, and the archival candidates.

The presence of only very faint hard X-ray emission associated with the optical flaring and reflaring of Swift J1943+0228 may be indicative of repeated failure of the heating front to propagate throughout the disk. If Swift J1943+0228 is indeed an LMXB, the previously detected 2012 outburst appears also to have never transitioned into the soft state. Tetarenko et al. (2016) found that around 39% of the outbursts present in the WATCHDOG catalog did not transition into the soft state and that these hard-only outbursts represent a substantial component of all events. Postulating that these hard-only outbursts represent sources that did not reach the required mass transfer rate to transition to the soft state, it is possible that these optical outbursts represent the lowest energy tails of these phenomena, where the outburst stalls before increased mass transfer leads to brightening in the hard state.

Because almost all XRB outbursts, even failed transition outbursts, are discovered due to X-ray brightening, untargeted searches at optical wavelengths of outbursts can provide a powerful complementary pathway to the discovery and characterization of LMXBs and their outbursts (e.g., Bellm et al., 2023). Due to their increased sensitivity to low luminosity and earlier activity, optical searches will offer a unique window into a population of outbursts that are not well understood. While we only have a few examples of this behavior in the ZTF data, the location and greater depth of LSST will enable observations of a greater number of LMXB outbursts, including observations earlier, closer to outburst onset, and allow us to build a robust sample of optical outbursts.

6 Appendix: X-ray and Optical Lightcurves of LMXB Outbursts

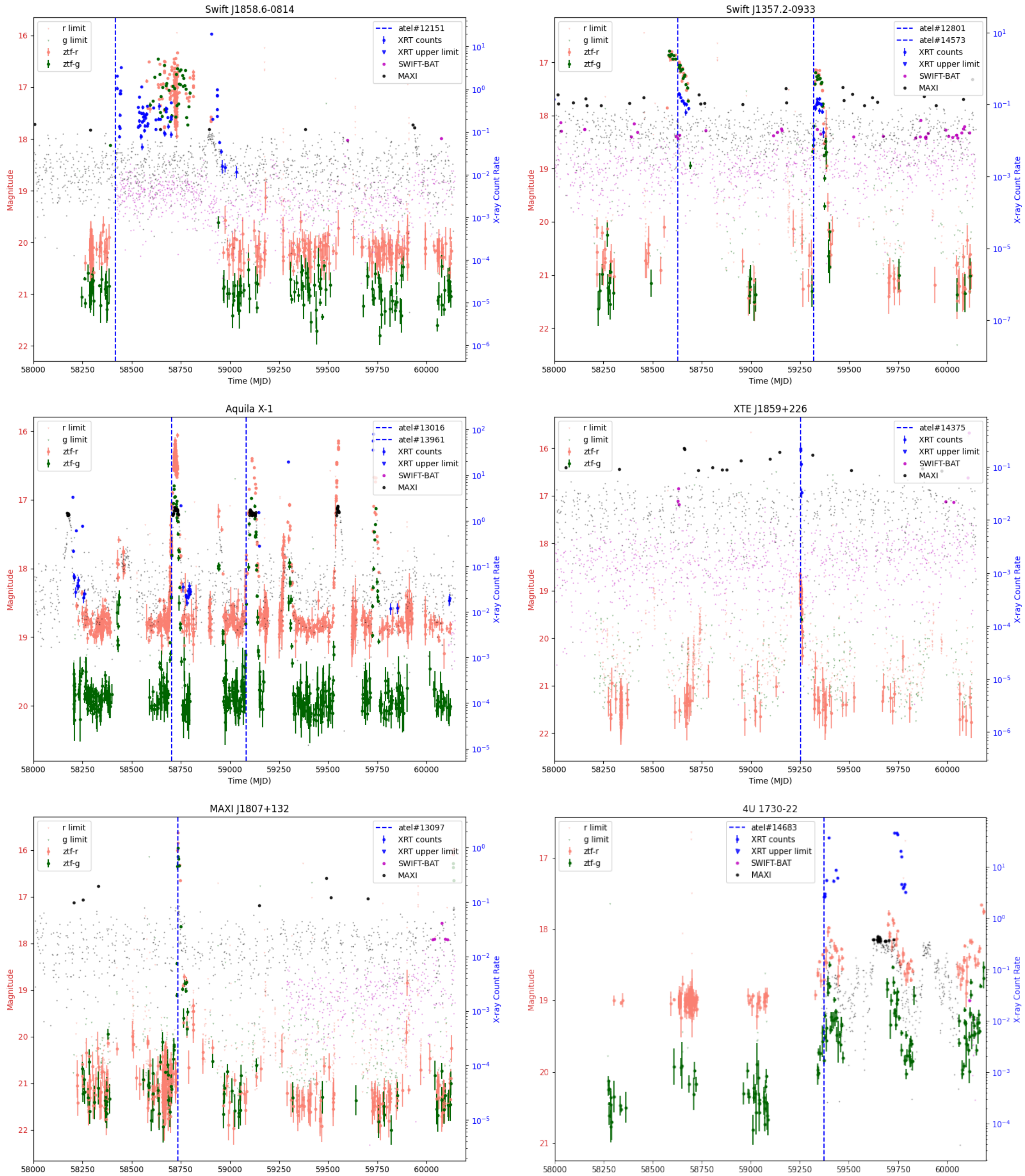

Figure 2.8: ZTF optical and X-ray lightcurves of LMXBs that have been reported in outburst since June 2018. These 6 sources all have at least one ZTF observation prior to the date and time of the first observation by an all-sky monitor as reported in the atel in the legend. The red and green points are ZTF magnitudes in r and g band. The blue points give counts between 2–10 keV as detected by Swift XRT. The back points give counts observed by Swift BAT (15–150 keV) and the purple points are MAXI observations (2–30 keV). Larger BAT and MAXI points are detections exceeding 3σ. Swift J1858.6-0814 was initially discovered in 2018 (Krimm et al., 2018), meaning this source could have been detected by ZTF as a then unknown LMXB before X-ray ASMs.

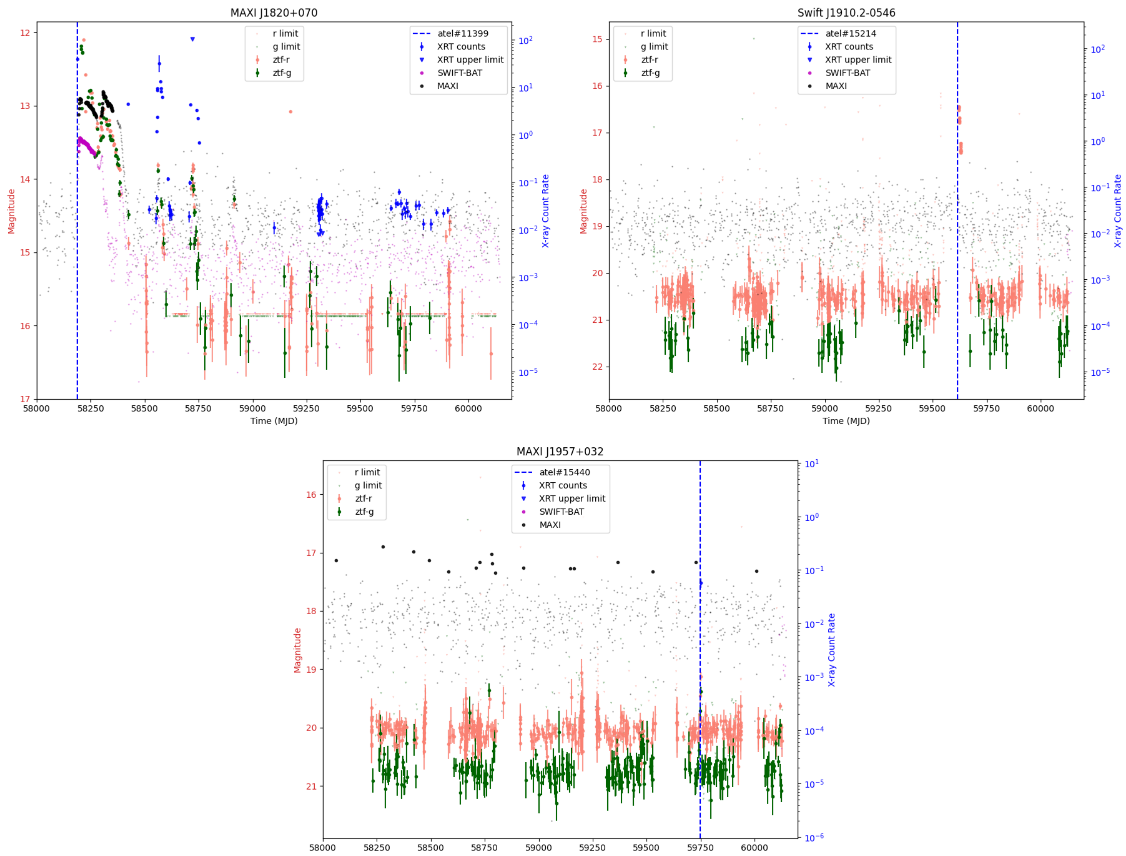

Figure 2.9: Optical and X-ray lightcurves of LMXBs that have gone into outburst since the beginning of ZTF. These 3 sources have simultaneous X-ray and ZTF data. The first discovery of MAXI J1820 was in the optical by ASAS-SN (Tucker et al., 2018); ZTF did not observe MAXI J1820 prior to the X-ray detections.

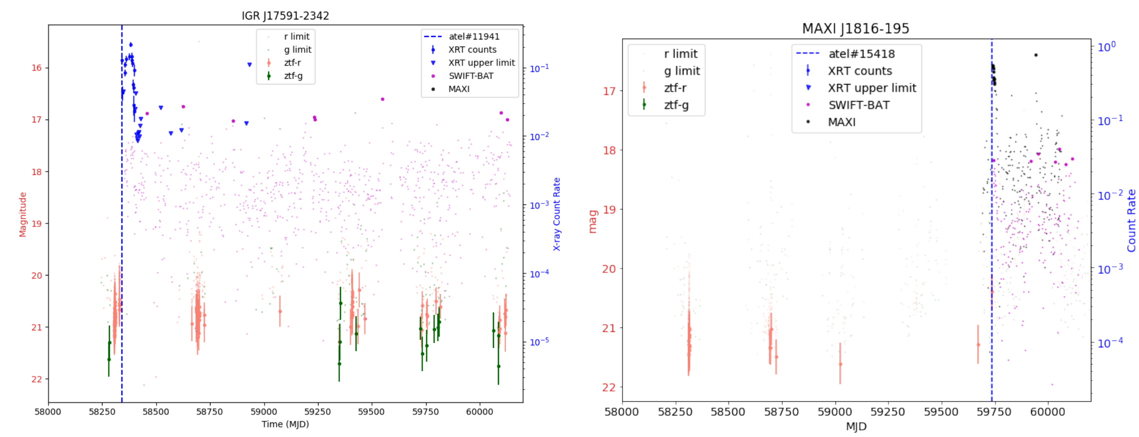

Figure 2.10: Optical and X-ray lightcurves of an LMXB that have gone into outburst since the beginning of ZTF. These sources display outbursts in X-ray but no available or inconclusive optical brightening in ZTF data. MAXI J1815-195 shows a single r-band point potentially in outburst. The position of this brightening corresponds to source 3 in atel #15479 (de Martino et al., 2022)

CHAPTER 3

SIMULATING THE GALACTIC POPULATION OF X-RAY BINARIES USING `COGSWORTH`

1 Background

Most massive stars are born not in isolation, but in binary or higher-order multiple systems (e.g., Duchêne & Kraus, 2013; Kroupa, 1995; Moe & Di Stefano, 2017; Offner et al., 2023; Oliva & Kuiper, 2020), making binary interaction an important part of the evolutionary process that produces neutron stars, black holes, and compact-object systems in astrophysics (e.g., de Mink et al., 2014; Podsiadlowski et al., 1992; Sana et al., 2012). Yet despite decades of work, binary stellar evolution and interaction remains highly uncertain, with open questions surrounding mass transfer, common-envelope evolution, angular-momentum loss, supernova kicks, and compact object (CO) formation.

Low-mass X-ray binaries (LMXBs) provide a potential test case for evaluating these uncertainties. LMXBs are systems with tightly bound orbits where a neutron star or black hole accretes from a lower-mass ($> 2\,M_{\odot}$) companion due to Roche lobe overflow (RLOF). Formation of LMXBs involves multiple poorly constrained evolutionary phases and therefore may be sensitive to the assumptions built into binary evolution models.

To form an LMXB, a system with a much more massive primary star evolves off the main sequence, leading to an interaction with the lower-mass companion. A common-envelope (CE) phase then is thought to shrink the orbit of the system, so that the binary survives the supernova that forms the CO and the associated natal kick (Ivanova et al., 2013; Kalogera & Webbink, 1998; Tauris & van den Heuvel, 2006). The orbit must tighten enough during the CE phase before the envelope is ejected, but the envelope must be ejected before the two stars merge completely. After the supernova, angular-momentum losses through magnetic braking and gravitational radiation can then drive the low-mass companion into Roche lobe overflow (RLOF), leading to accretion onto the CO, which forms an LMXB. RLOF can also be initiated if the low-mass companion evolves into the giant, or via the Kozai-Lidov interaction if the system is in a hierarchical triple (Naoz et al., 2016).

LMXBs form our only robust observed population of galactic stellar mass black holes, and along with millisecond pulsars form a sizable sample of interacting neutron stars. We have an observed population of LMXBs in the Milky Way from which we have spatial distributions, orbital periods, donor properties, and transient/persistent behavior (Avakyan et al., 2023; Fortin et al., 2024; Heinke et al., 2025; Tetarenko et al., 2016). Population synthesis therefore offers a powerful way to connect theory and observation, by evolving large ensembles of binaries under different physical prescriptions and asking which assumptions best reproduce the observed LMXB population. In this way, LMXBs serve not only as an interesting endpoint of massive binary evolution, but also as an empirical testbed for improving models of binary stellar evolution itself.

Previous studies of LMXB population synthesis have struggled to form BH-LMXBs, as a primary star with a mass great enough to form a BH, and a secondary less massive than around $1.5\,M_{\odot}$ may not have the energy to eject the envelope before merger under most prescriptions of CEE (e.g., Kiel & Hurley, 2006; Podsiadlowski et al., 2003). This "CE-bottleneck" leads to a smaller number of BH-LMXB systems in simulated populations relative to observations (Kalogera & Webbink, 1998; Kiel & Hurley, 2006). Under standard binary stellar evolution assumptions, population synthesis models underproduced galactic BH LMXBs by more than an order of magnitude, and just tuning the CE prescription was not enough to solve the problem and that modifications to other aspects of stellar evolution were needed to match the observations.

In one class of proposed solutions, the isolated binary pathway remains the primary LMXB formation channel, but envelope ejection becomes more efficient, either explicitly through a larger effective CE efficiency (α) or implicitly through stellar models that leave the primary with a less tightly bound envelope (Yungelson & Lasota, 2008). Kiel & Hurley (2006) also found that reducing helium-star wind mass loss substantially improves BH-LMXB production, because weaker winds leave progenitors in a state more conducive to later interaction. A closely related idea is that many present-day BH-LMXBs may descend not from binaries born with truly low mass secondaries, but from intermediate-mass X-ray binaries (IMXBs), whose more massive donors are better able to survive CE and later evolve to lower masses, although it appears the resulting donor stars can be too hot compared with the observed BH-LMXB population (Kiel & Hurley, 2006). Another proposed solution involving the standard CE channel argues that if many BHs form through failed supernovae, the BH progenitor stars can be less massive and their envelopes less tightly bound, meaning low mass companions are more likely to survive the CE phase (Wang et al., 2016).

A second family of solutions attempts to bypass the CE bottleneck altogether. One proposal is that BH-LMXBs can form from very wide binaries in dense galactic environments, where dynamical encounters gradually increase the eccentricity of orbit until the stars pass close enough for tides to shrink and circularize the orbit, eventually producing a close interacting system without a prior CE phase (Klencki et al., 2017; Michaely & Perets, 2016). Another explanation is that most LMXBs form in hierarchical triples where the Kozai-Lidov effect can drive the inner binary to a much tighter orbit (Naoz et al., 2016). These channels convert the CE problem into a dynamical problem instead. These diversity of explanations shows that there is still no single universally accepted solution to the BH-LMXB formation problem.

`cogsworth` (Wagg et al., 2025b) can create and evolve our populations of binary systems (Breivik et al., 2020, via `COSMIC`,) while tracking their positions and kinematics throughout the galaxy (Price-Whelan, 2017, via `Gala`,). `COSMIC` allows users to initialize populations of binary systems that are likely to form with specified components, such as compact objects, and then derive meaningful distributions on the parameters characterizing the binary and the stellar components. `Gala` enables the galactic evolution of orbits, including through a time-varying galactic potential. By combining the two, `cogsworth` can track populations of binary systems over the course of their evolution through the galaxy, which allows the calculation of observable parameters, such as flux and spatial distribution, with fewer assumptions about e.g. the fiducial distance and locations of these systems throughout the galaxy.

Binary population synthesis provides a framework for connecting the physics of binary evolution to the observed population of LMXBs. In these simulations, we begin with a distribution of binaries, sampling component stars from an initial mass function, and then evolve them through the main sequence, common-envelope evolution, supernovae, compact object formation, angular-momentum loss, and Roche-lobe overflow to predict the present-day properties of X-ray binaries under a chosen set of physical prescriptions governing the binary stellar evolution. Tools for doing this include the Binary Stellar Evolution code (BSE, Hurley et al., 2000), StarTrack (Belczynski et al., 2008), and `COSMIC` (Breivik et al., 2020).

These simulations are useful because simulated populations can be compared directly to real observables, such as numbers of LMXBs, the ratio between MS and BH LMXBs, the observed X-ray luminosity function (XLF), the orbital period distribution, the donor properties, and the number of persistent and transient systems. For example, Wang et al. (2016) used binary population synthesis of galactic BH-LMXBs and compared the predicted donor mass, donor temperature, and orbital period distributions to the observed sample. They then placed constraints on the supernova mechanism, the binding-energy parameter, the common-envelope efficiency, and the initial companion-mass distribution, and proposed that BH-LMXBs are easier to form if many black holes are born in failed supernovae. Repetto et al. (2017) approached the problem from a different angle by synthesizing BH and NS X-ray binaries and evolving them in the galactic potential, showing that the root-mean-square height above the galactic plane is a powerful observable for discriminating among compact object formation scenarios and for constraining natal kicks. When a model fails one or more of these tests bestween observed and predicted population properties, the discrepancy can inform revisions of the input physics, such as the CE efficiency, natal kicks, and stellar-wind mass loss.

Motivated by these considerations, in this chapter I use `cogsworth` to simulate the Galactic population of LMXBs. In section 2, I detail the methods for initializing our populations of binaries using `cogsworth`, as well as the binary stellar parameters I vary to examine their effects on the resulting LMXB population. In section 3, I detail the outcomes of the simulations in terms of the observables: spatial distribution of the LMXBs, fluxes and luminosities, and relative numbers compared to default parameters. In section 4, I compare our simulated results to observations of LMXBs and discuss the implications for different formulations of binary stellar evolution models, as well as any modifications needed to `COSMIC` for more robust population synthesis of LMXBs.

2 Methods

2.1 Population Synthesis and Binary Evolution

I first sampled an initial population of 2 million binary systems following the Kroupa (2001) initial mass function, using the star formation history from Sanders & Binney (2015). I specifically sample systems where at least one star is likely to become a neutron star or black hole. I then run binary stellar evolution with default `COSMIC` v3.7.2 binary evolution parameters. I also evolve the orbits of these systems in a galactic potential to obtain present day positions and kinematics.

I then take the same sample of binary systems and vary one binary stellar evolution parameter at a time in `COSMIC`. The full suite of parameters I vary can be found in table 3.1. In the following subsections I discuss how each parameter could have an effect on the numbers and types of X-ray binaries formed.

`kickflag`

The natal kick prescription, or `kickflag`, sets the particular natal kick prescription to use. The standard COSMIC kick distribution, with `kickflag` of 1, uses the Pfahl et al.

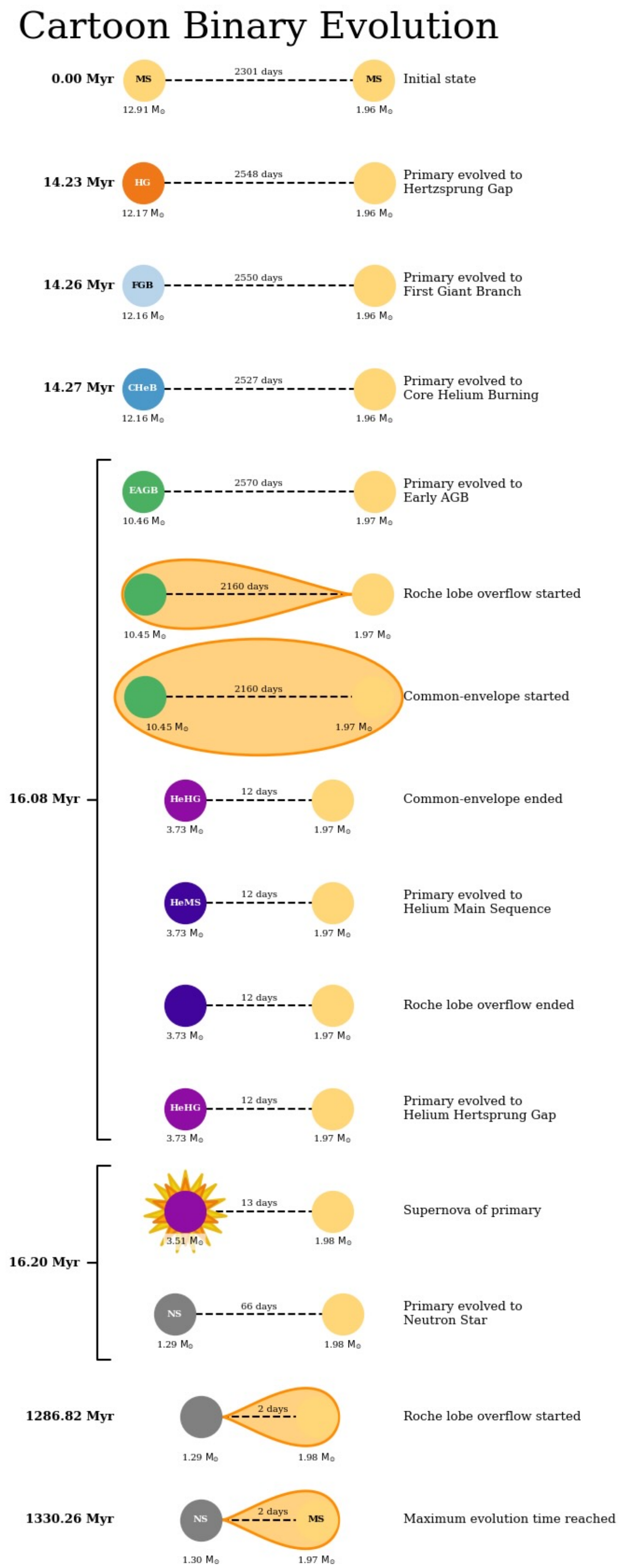

Figure 3.1: Canonical isolated formation of one simulated NS LMXB.

Table 3.1: COSMIC parameter variations used in this work.

`Parameter`	Description	Default	Varied Values
`kickflag`	Natal kick prescription selector	5	1
`alpha1`	Common-envelope efficiency parameter (α)	1.0	0.1, 0.2, 0.5, 2, 5, 10, 20, 50
`eddfac`	Max accretion rate is (`eddfac` $\times$ the Eddington rate)	10	0.1, 0.5, 1, 5, 20
`qcflag`	Critical mass-ratio prescription for unstable mass transfer / CE onset	1	0, 2, 3, 4, 5
`windflag`	Wind mass-loss prescription selector	3	0, 1, 2
`remnantflag`	Remnant-mass prescription selector for NS/BH formation	4	3
`LBV_flag`	Model for Luminous Blue Variable (LBV) mass loss	1	0, 2

(2002) prescription for handling natal kicks, with kicks for iron core collapse supernovae (FeCCSN) drawn from a Maxwellian distribution with $\sigma = 265\,\mathrm{km\,s^{-1}}$ and electron capture supernovae (ECCN) and ultra stripped supernovae (USSN) drawn from a Maxwellian with $\sigma = 20\,\mathrm{km\,s^{-1}}$. Kicks are also modulated in the case of black holes by fallback following Fryer et al. (2012). For our default case, I use a `kickflag` of 5, which uses the kick prescription in Disberg et al. (2025) for core collapse supernovae (CCSN).

Natal kicks are one of the strongest controls on XRB populations, since a strong kick can disrupt the binary system, widen the orbit, or lead to a more eccentric orbit. Stronger kicks can also lead to a puffier distribution of XRBs relative to the overall galactic distribution of stars. The strength of neutron star kicks compared to the modulated kicks due to fallback onto black holes can also change the fraction of NS-XRBs vs BH-XRBs.

`alpha1`

`alpha1` is the common-envelope efficiency (CE) parameter, which is the efficiency the orbital energy ejects the envelope at. I use a default value of `alpha1` = 1. At lower CE efficiencies, the system will tend to spend more time in the CE phase, leading to more mergers and fewer binaries that survive the CE phase. More moderate `alpha1` may be more effective at tightening the orbits into the close binary systems that form XRBs without excessive mergers. Higher `alpha1` can mean more surviving binaries, but the resulting systems may be too wide to start the Roche lobe overflow (RLOF) needed for LMXBs. However, if the donor star is massive, these wide binaries may still form wind-fed HMXBs.

`eddfac`

The `eddfac`, or Eddington-limit factor sects the maximum accretion rate onto the compact object relative to the Eddington limit of 1. The default value used is `eddfac` = 10, which aligns with the observed super-Eddington luminosities of transient LMXBs, where the short term mass transfer rate in outburst exceeds the Eddington limit in the high viscosity outburst state (King, 2002). A lower Eddington factor would mean lower accretion rates and lower luminosity systems.

qcflag

The qcflag selects the model to determine the critical mass ratio (q_{crit}) for the onset of unstable mass transfer and/or a common envelope during RLOF. Different prescriptions of qcflag have different criteria for the onset of CE from stable RLOF mass transfer, particularly for giant branch (GB) and AGB stars. The default qcflag of 1 uses the BSE prescription from Hurley et al. (2002), but follows the criteria from Hjellming & Webbink (1987) for GB and AGB stars. qcflag =0 follows all the BSE stability criteria from Hurley et al. (2002). qcflag =2 follows the criteria from Claeys et al. (2014), while qcflag =3 follows the same, but follows the criteria from Hjellming & Webbink (1987) for GB and AGB stars. Finally, qcflag =4 follows the StarTrack prescriptions from Belczynski et al. (2008), except for white dwarf donors, which follow Hurley et al. (2002), and qcflag =5 follows the stability criteria from Neijssel et al. (2019), where mass transfer from stripped stars is always assumed to be dynamically stable.

For LMXB formation, more restrictive stability criteria tend to produce more CE events, which can help increase the potential number of systems that undergo the orbital tightening needed to create LMXBs. In particular, the treatment of giant donors and especially helium-star donors is significant, since those phases are often necessary to produce the compact object component of an LMXB.

windflag

The windflag determines the stellar-wind model. A windflag of 0 uses the standard SSE/BSE model from Hurley et al. (2000), and windflag of 1 uses the StarTrack model from Belczynski et al. (2008). windflag = 3 adds metalicity dependence for O/B and Wolf Rayet stars (Vink & de Koter, 2005; Vink et al., 2001), and the default value of windflag = 3 is the same as 2, but includes LBV-like mass loss for giants and non-degenerate stars beyond the Humphreys-Davidson limit.

Stellar winds can shape the compact object progenitor in several ways. A strong stellar win can reduce stellar mass and core mass before collapse and the subsequent type of CCSN. Large mass loss can also widen the binary system and change when and whether Roche lobe overflow happens. Stronger winds that from the companion in wind-fed HMXBs can also increase the luminosities of those systems.

remnantflag

The remnantflag determines the remnant mass prescription used for NSs and BHs. The default value of remnantflag = 4 follows the delayed prescription from Fryer et al. (2012) and fills the mass gap between neutron stars and black holes. Setting remnantflag = 3 gives remnant masses following the rapid prescription from Fryer et al. (2012) and results in a mass gap between neutron stars and black holes.

The remnant mass model could potentially affect whether the produced compact object is a neutron star or black hole, and therefore the mass and fallback fraction of the compact object. This could lead to differences in the fraction of BH-XRBs as well as the overall number of XRB systems formed.

Table 3.2: Model counts, normalized counts, and ratios compared to default parameters for BH and NS LMXB populations over the entire history of the galaxy. Ratios are rounded to the nearest hundredth. Ratios below unity are shaded red and ratios above unity are shaded green.

Parameter	Value	Model Counts		Norm Counts		Ratios	
		BH	NS	BH	NS	BH ratio	NS ratio
kickflag	1	60	93	26307	40777	0.88	0.75
eddfac	0.1	10	122	4384	53492	0.15	0.98
	0.5	21	128	9207	56123	0.31	1.03
	1	32	105	14030	46038	0.47	0.85
	5	53	127	23238	55684	0.78	1.02
	20	58	113	25430	49546	0.85	0.91
qcflag	0	182	207	79800	90762	2.68	1.67
	2	12	74	5261	32446	0.18	0.60
	3	8	62	3507	27184	0.12	0.50
	4	144	238	63138	104354	2.12	1.92
	5	36	112	15784	49107	0.53	0.90
windflag	0	61	115	26746	50423	0.90	0.93
	1	24	104	10523	45600	0.35	0.84
	2	53	106	23238	46477	0.78	0.85
remnantflag	3	16	106	7015	46477	0.24	0.85
LBV_flag	0	49	109	21484	47792	0.72	0.88
	2	59	113	25869	49546	0.87	0.91
alpha1	0.1	61	27	26746	11838	0.90	0.22
	0.2	102	72	44723	31569	1.50	0.58
	0.5	56	116	24553	50861	0.82	0.94
	2	124	126	54369	55246	1.82	1.02
	5	192	177	84185	77608	2.82	1.43
	10	148	189	64892	82869	2.18	1.52
	20	72	128	31569	56123	1.06	1.03
	50	29	113	12715	49546	0.43	0.91
default	–	68	124	29815	54369	1.00	1.00

2.2 Evaluation of Outcomes

From the evolved populations, I then select the timesteps for systems containing either a NS or a BH, with a non-degenerate companion where the companion radius is greater than the Roche lobe radii. I then re-run stellar evolution at time resolution of 10 Myr by setting dtp = 0 to get a more detailed view of the mass transfer onto the compact object. Using the prescription for X-ray binary luminosity from Misra et al. (2023), I calculate the luminosity of the systems due to mass transfer onto the compact object. Setting a fiducial "Earth location" in the galactic plane 8 kpc from the galactic center, I also calculate simulated fluxes and galactic latitudes.

Our final set of simulations consists of the population of binaries that experienced an LMXB period across the history of the galaxy for the default parameters, and for each of the variations in the binary evolution parameters. Each LMXB population was created by evolving the same initial sample of binaries through different binary evolution parameters, allowing us to make direct comparisons on how each parameter affects the formation of LMXBs. `COSMIC` tracks the mass of total binaries and total single stars sampled from the IMF needed to create our sample of compact object binaries. I take the total of these stellar masses and divide into the total Milky Way stellar mass (Licquia & Newman, 2015, $5.7 \times 10^{10}\,\mathrm{M}_{\odot}$) to find a normalization factor needed to compare our numbers to the galactic numbers in the Milky Way.

3 Results

We defer a full statistical treatment on the observed numbers of LMXBs and distributions of all observables for future work (see 4.2. However, I compare our distributions from `cogsworth` to some summary statistics of the observed galactic population and run some basic statistical tests between the two. I use Tetarenko et al. (2016) for BH-LMXB outburst statistics on the luminosities of systems. I also refer to peak fluxes from Avakyan et al. (2023). I compare the galactic heights of the LMXBs to a random sample of stars from the same simulations, and calculate galactic latitude to compare to our observed distribution of LMXBs from (Fortin et al., 2024). I focus on these observables because they requre both the binary stellar evolution and galactic orbital evolution components, and thus use different measurements than previous population synthesis studies, which use fiducial values and distributions to place simulated LMXBs in the galaxy.

3.1 Relative Numbers of LMXBs Formed

Table 3.2 gives the total number of each type (NS or BH) of LMXB at formation for the default `COSMIC` parameters, as well as each variation tested. The model counts columns give the number present in the 2 million binary sample, while the norm counts columns multiply the model counts by a factor to account for the relative total stellar mass sampled compared to the total stellar mass of the Milky Way from Licquia & Newman (2015). Note that these numbers give the total number of systems created over the entire simulated lifetime of the galaxy in `cogsworth`.

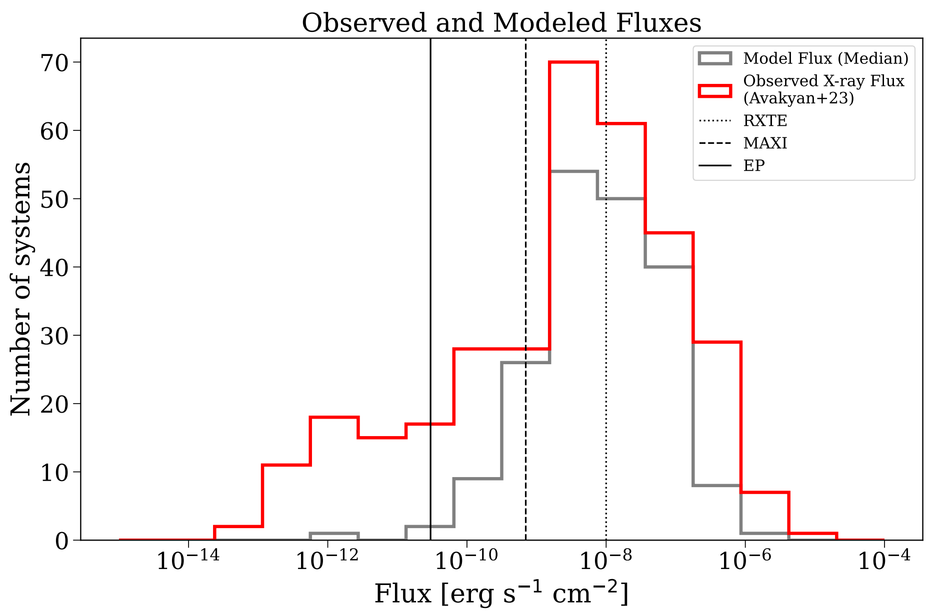

Figure 3.2: Observed X-ray fluxes and simulated X-ray fluxes from binary stellar evolution models. The vertical lines give the sensitivity limit from 3 different X-ray all sky monitors.

The ratios column shows how the number of LMXBs changes in each variation relative to the default parameters. Somewhat surprisingly, the simulations do not reproduce the CE bottleneck problem for this particular set of simulations, with the overall ratio of one BH-LMXB to two NS-LMXBs similar to our observed ratios (Corral-Santana et al., 2016). However, I do find certain regimes where the proportion of BH-LMXBs formed is quite low compared to NS-LMXBs. In particular, I find that low values of `eddfac`, `qcflag` of 2 and 3, `windflag` of 1, `remnantflag` of 3, and `alpha1` greater than 20 seem to result in this mismatched ratio of compact objects. I also find that proportionally fewer neutron stars are formed at low `alpha1` and while `qcflag` of 0 or 4 boosts both NS and BH formation, more BH systems are formed relative to NS systems. For discussions of potential reasons, see section 4.1

3.2 Flux and Luminosity

The plot of the flux and the luminosity of the simulated systems and the observed outburst fluxes and luminosities from X-ray observations is shown in figure 3.2. The histogram of observed fluxes is created using absorbed X-ray flux at soft X-ray bands from the XRBcats catalog (Avakyan et al., 2023), and the modeled flux is from the `cogsworth` simulations with default `COSMIC` parameters. For the modeled fluxes, I select the median flux during the LMXB phase of the binary.

Because `cogsworth` tracks the positions of the binary systems as their orbits evolve within a galactic potential, the distances and the fluxes I calculate are not based on fiducial distances and observations of the distributions of known LMXBs. I find that the simulations and the observations line up well for fluxes in excess of about $10^{-9}\,\mathrm{erg\,s^{-1}\,cm^{-2}}$. The observed

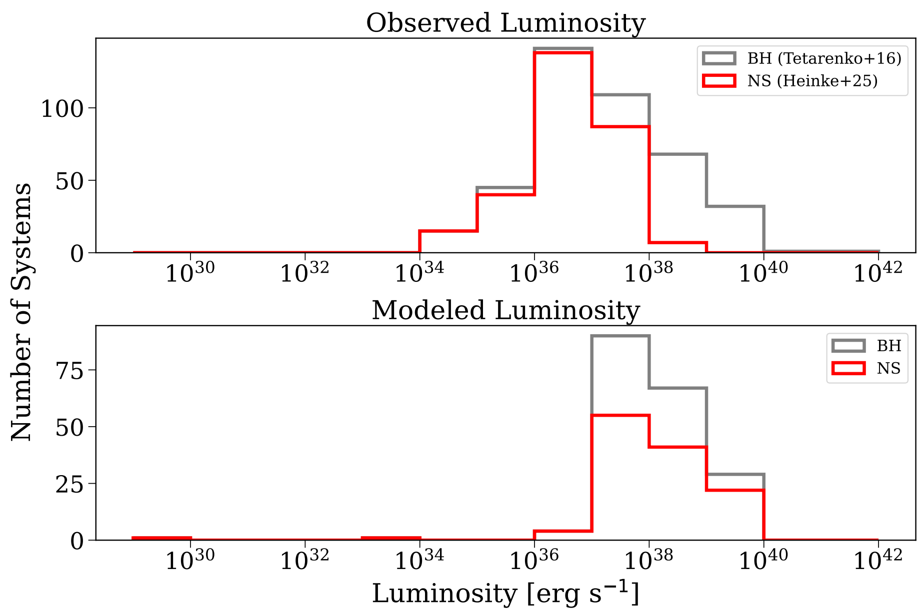

Figure 3.3: Top: Observed luminosity of outbursts from transient LMXBs. Bottom: simulated luminosity from running binary stellar evolution.

flux histogram shows a drop-off below the MAXI sensitivity limit, which is matched in the simulated fluxes. It is possible this is a coincidence, since there drop-off occures at the sensitivity limit of MAXI, and there may be selection bias unaccounted for. Additionally, the tail of histogram at fainter end shows a low flux population (i.e. $< 10^{-10}\,\mathrm{erg\,s^{-1}\,cm^{-2}}$) not present in the simulated population.

Figure 3.3 plots the histogram of observed peak luminosity of transient LMXBs in outburst (Heinke et al., 2025; Tetarenko et al., 2016) against the modeled median luminosity from the simulated systems, broken out by compact object. These plots appear similar to the histogram of flux. There appear to be very few simulated systems with median luminosity less than $\sim 10^{37}\,\mathrm{erg\,s^{-1}}$, which is why so few simulated systems are in the low flux tail end of the simulated fluxes. While the histograms are more aligned at the upper end of the luminosity range, there are roughly equal proportions of neutron stars and black holes in each bin for the modeled luminosity, but the observed luminosity of BH LMXBs tends to exceed the observed NS LMXBs.

3.3 Galactic Latitude and Spatial Distribution

Since many LMXBs do not have distance measurements, I compare the distribution of the galactic latitude of the full sample from Fortin et al. (2024) to the galactic latitudes of our simulated system, after taking the absolute value of the galactic latitude. The distributions are plotted in figure 3.4. To compare the distributions, I run a 2-sample KS test between the observed and modeled distribution with the null hypothesis that the two samples of galactic latitude are drawn from the same distribution. The p-value of the test was 0.213 meaning I did not reject the null hypothesis and conclude that the simulated galactic latitudes are

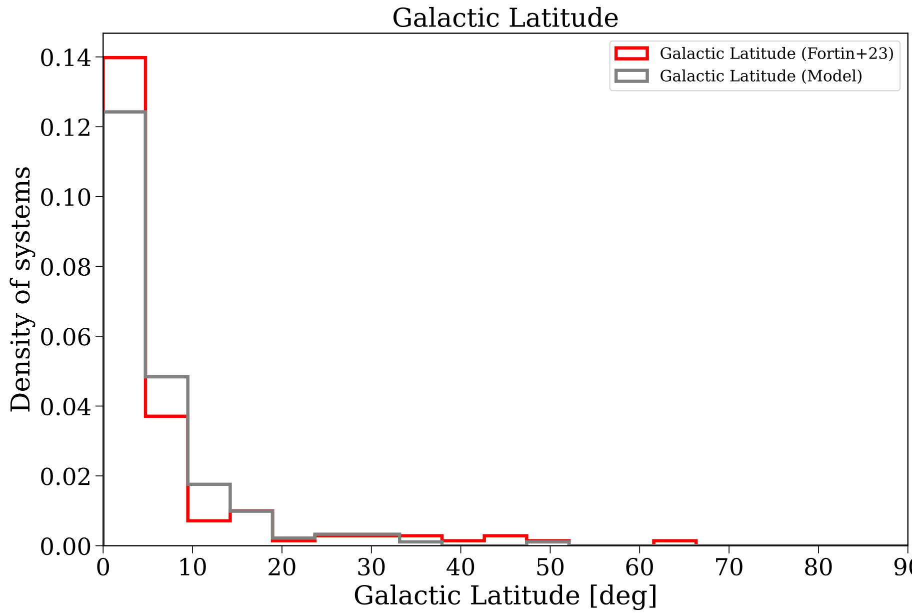

Figure 3.4: Galactic latitude of simulated and observed systems.

consistent with the observed ones.

4 Discussion

4.1 Differentiating Binary Evolution Parameter Values

Since the distributions of the observed parameters like flux and luminosity span orders of magnitude, and also are highly irregular, we use the permutation test to determine whether we can distinguish between the different outcomes for each variation of a parameter. For the evaluation of our binary stellar evolution models, I define a simple test by computing the difference between the median observed value (e.g. of flux) to the median simulated value. The permutation test is a nonparametric method that compares the test statistic when applied to our simulated and observed values, to the test statistic when applied to many random partitions of the same sizes of the combined set of values. The p-value of the test is found by calculating the proportion of random partitions that result in a test statistic as extreme as the originally observed statistic.

To quantify if we can evaluate the difference between the outcomes as measured by this test statistic at a significance of $p < 0.05$, I ran the permutation test between each variation of each parameter. The results are summarized in table 3.3. I find that there are two parameters that produce statistically significant differences in the median flux values: `eddfac`, and `qcflag`. These can also be seen visually in the vertical dotted lines in figure 3.5.

Table 3.3: Pairwise comparison tables for the p-values of permutations tests between simulations. The p-values less than 0.05 are shaded in green, and the default parameter is bolded.

(a) `eddfac`

	0.1	0.5	1	5	**10**	20
0.1	–	0.000	0.000	0.000	0.000	0.000
0.5	0.000	–	0.046	0.000	0.000	0.000
1	0.000	0.046	–	0.239	0.094	0.000
5	0.000	0.000	0.239	–	0.613	0.248
10	0.000	0.000	0.094	0.613	–	0.278
20	0.000	0.000	0.000	0.248	0.278	–

(b) `qcflag`

	0	**1**	2	3	4	5
0	–	0.950	0.021	0.974	0.045	0.695
1	0.950	–	0.046	0.983	0.089	0.729
2	0.021	0.046	–	0.368	0.007	0.025
3	0.974	0.983	0.368	–	0.481	0.853
4	0.045	0.089	0.007	0.481	–	0.143
5	0.695	0.729	0.025	0.853	0.143	–

4.2 Future Directions for `cogsworth` Simulations of LMXBs

Persistence vs Transient LMXB Behavior

LMXBs are known to be either persistent, showing high rates of accretion onto the compact object, or transient, where the system alternates between episodes of high mass transfer rate outbursts and low mass transfer rate quiesence, at a typical duty cycle of a few %s for known systems (Tetarenko et al., 2016). However, the LMXBs in `COSMIC` appear to be solely made up of persistent systems. A more accurate simulation would determine whether the mass transfer via Roche lobe overflow meets the criteria for stability, resulting in a transient, outbursting system. A majority of known LMXB systems are made up of transient systems, so it is important to capture the correct behavior of these systems. The stability criteria in Lasota (2001) equation (36) contains the threshold for accretion by a hot stable irradiated disk, like one that would be found surrounding the black hole of an LMXB.

Other Observables

Recent studies have isolated the peculiar velocity of systems of X-ray binaries (Zhao et al., 2023), and accounted for kinematic heating during their galactic orbital evolution to place a lower bound on the initial kick on the black hole at the time of formation (Nagarajan & El-Badry, 2025). Preliminary results show that many of the BH-LMXB systems have near zero kick, due to fallback. Some BH LMXB systems also form from black holes with a higher kick. This appears consistent with the result of Nagarajan & El-Badry (2025), which

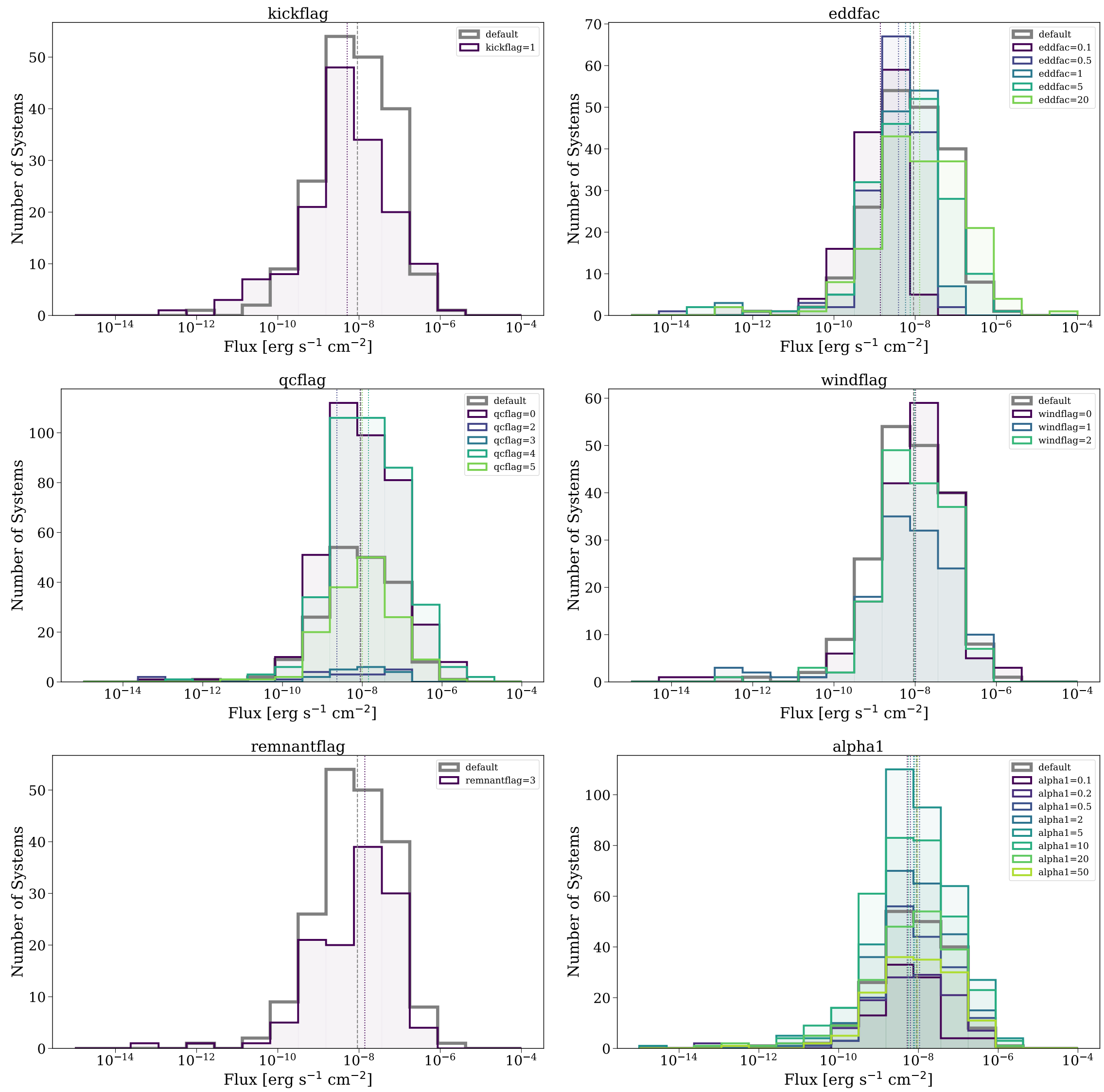

Figure 3.5: Histogram of simulated fluxes for variations of each binary stellar evolution parameter. The vertical dotted lines give the median flux, and the grey dashed line gives the median flux using default parameters.

found that some black hole binary systems show evidence of near zero kick ($\lesssim 10\,\mathrm{km\,s^{-1}}$), while others form with black holes that receive a significant kick ($\gtrsim 100\,\mathrm{km\,s^{-1}}$). A future statistical treatment of kicks and peculiar velocities may provide further and more robust confirmation of this result.

Other observables such as companion mass and orbital period have been used to evaluate population synthesis of LMXBs (Wang et al., 2016), including joint values of these parameters (e.g., Kiel & Hurley, 2006; Shao & Li, 2020). Future work should explore the parameter space that LMXBs form at and compare to the observed distributions of these features.

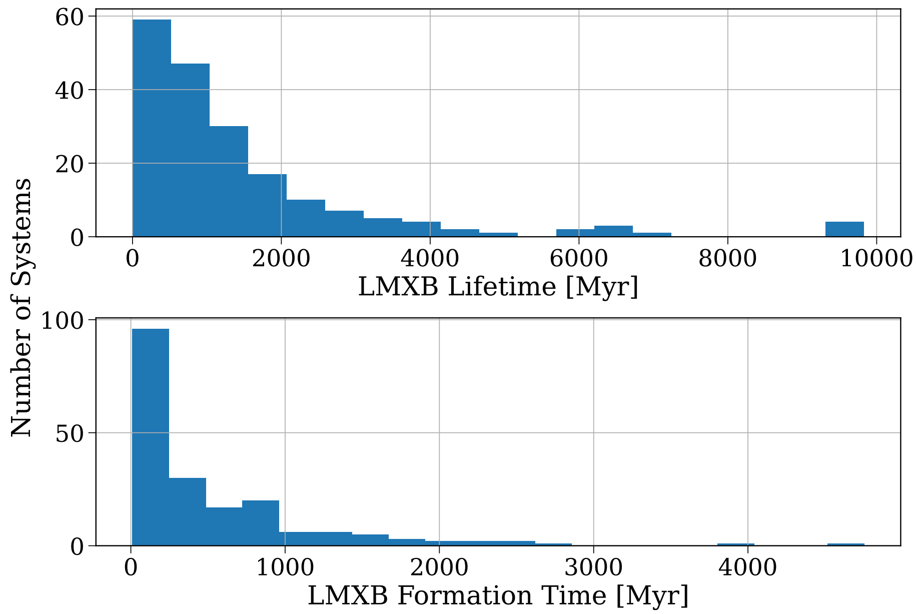

Figure 3.6: Lifetimes of simulated LMXBs, and the time of their formation in galactic time.

Unexplained Behavior in COSMIC

One particularly strange outcome from COSMIC was that during mass transfer, the primary would sometimes gain more mass than the secondary lost. This sometimes resulted in non-physical situations, such as the formation of a BH-LMXB from accretion induced collapse of a NS-LMXB for a companion with $< 1\,M_\odot$ (although accretion induced collapse of a NS LMXB into a BH LMXB has been found as an outcome of stellar evolution models (Siegel et al., 2023)). To restrict the impact of this on the analysis, I excluded BH LMXBs formed via this pathway. However, this makes analysis of a "present day" LMXB population impossible, since almost every simulated NS LMXB collapses into a BH LMXB, meaning the simulated NS LMXB lifetimes may be artificially shortened. The distribution of simulated LMXB lifetimes is given in figure 3.6, and the median simulated lifetime is slightly below 1 Gyr, which is shorter than the commonly accepted lifetime of $\gtrsim 1$ Gyr (Kar et al., 2024).

5 Conclusions and Future Work

I ran the first population synthesis study of galactic LMXBs using COSMIC for binary stellar evolution and find success in reproducing some key characteristics of the galactic LMXB population, such as the correct order of magnitude for the flux and luminosity distributions, the overall shape of the galactic height, and the ratio of NS LMXB to BH LMXB systems. Several formulations of binary stellar evolution were found to result in CE bottleneck, including certain formulations of the critical mass (qcflag) to begin mass transfer.

The simulated systems appear to reproduce the high end of the flux and luminosity distributions of LMXBs in outburst. However, the simulations fail to capture a lower luminosity series of systems. Further development of COSMIC may be necessary to capture the transient population of LMXBs, as there currently is no way to distinguish between persistent and transient systems, even though most galactic LMXBs are discovered due to their accretion disk outburst. Since the mass transfer rate in transient LMXBs is lower than in persistent LMXBs, this may also help explain the missing lower luminosity and flux systems. This may also prolong the lifetimes of the simulated LMXBs, which evolve past LMXBs more quickly than expected.

I find a simple test statistic, the difference between the median flux of two LMXB simulations, was sufficient to differentiate between the two binary stellar evolution models when the parameter varied was the eddfac or some values of qcflag. While the permutation test is robust to the irregular distributions that make up the flux and luminosity, a more nuanced test statistic should be formulated to better capture the differences between the distributions.

While anomalies in the mass transfer rates may complicate the latter three observables, future work should also examine the compact object kicks that result in the formation of LMXBs, as well as the orbital period of those systems, and the donor and compact object masses.

Acknowledgments

This work made use of the following software packages: astropy (Astropy Collaboration et al., 2013, 2018, 2022), matplotlib (Hunter, 2007), numpy (Harris et al., 2020), pandas (Wes McKinney, 2010), python (Van Rossum & Drake, 2009), scipy (Virtanen et al., 2020), COSMIC (Breivik et al., 2020), Cython (Behnel et al., 2011), gala (Price-Whelan, 2017), h5py (Collette, 2013), schwimmbad (Price-Whelan & Foreman-Mackey, 2017), seaborn (Waskom, 2021), and tqdm

This research made use of cogsworth and its dependencies (Wagg et al., 2025a,b)

Software citation information aggregated using The Software Citation Station (Wagg et al., 2025; Wagg & Broekgaarden, 2024).

CHAPTER 4

OPTICAL COUNTERPARTS TO X-RAY SOURCES IN LSST DP1

1 Introduction

The X-ray sky provides a window into high-energy processes in extreme environments across the universe. X-ray surveys offer an important way to discover a range of interesting and rare objects such as low mass X-ray binaries (LMXBs), high mass X-ray binaries (HMXBs), binary and isolated millisecond pulsars (MSPs), cataclysmic variables (CVs), as well as other objects like active stars, galaxies, AGN, and galaxy clusters. Over the last 25 years, missions such as *Chandra*, *XMM-Newton*, *Swift*, and *eROSITA* have revealed about a million sources, a small fraction of which have been classified with the aid of multiwavelength observations, while the majority remain unidentified.

Since the localization of X-ray sources is generally less precise than that of optical catalogs, the higher density of the latter often results in multiple optical sources falling within a single X-ray error circle. As a result, a variety of techniques have been developed to evaluate the strength of each potential match. One common technique is known as the likelihood ratio (LR) method, which estimates the probability that a given counterpart is the true match given the local stellar densities and distribution (Richter, 1975; Sutherland & Saunders, 1992). This is among the most widely adopted techniques, such as in the crossmatch between X-ray and optical sources in the ROSAT Bright source catalog and the USNO A-2 optical catalog (Rutledge et al., 2000), or the Chandra Galactic Bulge Survey (Wevers et al., 2016). More recently, Bayesian methods that incorporate priors and probabilities for probabilistic cross-identification have been developed (Budavári & Basu, 2016; Budavári & Szalay, 2008; Shi et al., 2019) and these methods have been also applied to the ROSAT all sky survey (Haakonsen & Rutledge, 2009). Some of these techniques, such as NWAY (Salvato et al., 2018) can evaluate multiple candidates or null matches across multiple catalogs jointly. In the past few years, Bykov et al. (2022) used machine learning techniques, training a neural network to perform an optical crossmatch of *eROSITA* sources in the Lockman Hole.

All of these techniques assume knowledge of the photometric priors, which is typically derived from known matched samples. However, the training and validation datasets for these models must be based on unambiguous matches (Salvato et al., 2018). In addition, many published crossmatches focus on a small area of the sky, such as the Lockman Hole Field, which display advantageous qualities, such as relative uniformity in density and absorption. Additionally, these methods assume that the depth in the X-ray sample used to develop the model is the same as for the X-ray catalog being crossmatched to. Quantities such as X-ray depth and absorption vary across the sky, making a reliable all-sky crossmatch difficult.

Compounding this fact, the upcoming Legacy Survey of Space and Time (LSST) by the Vera C. Rubin Observatory (Ivezić et al., 2019) will provide the deepest all-sky optical catalog to date. LSST will observe more than 18,000 sq. deg. of the southern sky in six broadband filters (u, g, r, i, z, y) to single-visit depths of 24.5 mag and co-added depths of 27.5 mag. A crossmatch between LSST and the latest X-ray all-sky surveys, such as *eROSITA*, has the potential to uncover vast numbers of rare objects. The high density of optical sources will make building a reliable set of unambiguous matches more difficult than ever. However, with roughly 3-4 days between visits, the cadence of LSST will enable an orthogonal approach towards evaluating potential optical counterparts, as each candidate will include not only color information, but time domain data as well. Many X-ray emitting objects are also transient or variable at optical wavelengths (see table 4.1) and we thus aim to leverage this fact to aid in the identification of optical counterparts.

To evaluate the difficulty of performing an X-ray/optical crossmatch at LSST depths, as well as the concept of using variability to aid in counterpart identification, we perform a crossmatch between a combined X-ray catalog of sources from several X-ray missions, and the first data preview from Rubin Observatory. The Rubin Observatory Data Preview (DP1; NSF-DOE Vera C. Rubin Observatory, 2025a), released June 30, 2025, is the first on sky "science-grade" dataset and the second of three data previews from LSST. It comprises about 2,000 exposures from seven fields captured with the LSST Commissioning Camera (LSSTComCam) in November and December 2024. DP1 includes raw and pipeline-processed visit images, visit-level source catalogs, co-added images with object catalogs, forced source catalogs, difference images and difference image analysis (DIA) catalogs, and other Science Support Products delivered via the Rubin Science Platform for early-science testing. This preview allows the community to validate the pipelines, explore real early data, and prepare for the full LSST survey.

In Section 2, we present the X-ray catalogs we selected and combined, as well as the contents of and data products we utilized in DP1. We also discuss challenges of performing the crossmatch to dense optical fields and how we utilize LSDB (Caplar et al., 2025) to perform the crossmatch. In Section 3, we present the crossmatched catalog and evaluate the most likely optical counterparts. In Section 4 compare to crossmatches to known sources in the DP1 fields, and examine where the most reliable matches fall in X-ray and optical feature space. In Section 5, we summarize our findings and look ahead to our expectations for LSST.

2 Methods

2.1 X-ray Catalog

We began by assembling a combined X-ray catalog from the most up-to-date releases for five X-ray catalogs: the *Chandra* source catalog (CSC2.1; Evans et al., 2024), the *XMM-Newton* serendipitous source catalog (4XXM-DR14; Webb et al., 2020b), the *XMM-Newton* slew survey catalog (XMMSL3; Saxton et al., 2008), the Swift-XRT point source catalog (2SXPS; Evans et al., 2020), and the *eROSITA* all-sky survey source catalog (eRASS DE DR1 (hereafter just eRASS1); Merloni et al., 2024). From each catalog, we selected the name, right ascension, declination, positional uncertainty, and broadband X-ray flux.

The column names for the broadband flux and positional uncertainty are listed in Table 4.2. In each case we choose the column that accounts for both systematic uncertainty and positional uncertainty from source detections. For *Chandra*, we take the major axis of the error ellipse as our uncertainty radius. We take this uncertainty and scale it to a 1σ error radius $R_{1\sigma}$. Then, assuming Gaussian errors, we multiply to get the 95% error radius $R_{95} = 1.96R_{1\sigma}$.

Since the energy range of the broadband flux is different for each instrument, we list the energies in Table 4.2, as well as an additional description of the flux pulled from the documentation for each catalog. The eRASS1 broadband flux was calculated by adding bands

Object Type	X-ray Mechanism	Optical Signature	Timescale
Flare Star	Coronal reconnection	Flares	Minutes–hours
Active Binary	Coronal reconnection	Ellipsoidal variations, eclipses	Hours–days
YSOs	Magnetic activity, accretion	Flares, bursts, dips	Hours–days
Cataclysmic Variable	White dwarf accretion	Outbursts, eclipses	Hours–days (outbursts)
Low Mass X-ray Binary	NS/BH accretion	Ellipsoidal variations, outbursts	Hours–days (orbital); weeks–months (outbursts)
High Mass X-ray Binary	NS/BH wind accretion	Pulsations, periodic brightening, super-orbital modulation	Hours–days (pulsations); days–years (orbital); weeks–months (super-orbital)
AGN / Quasar	Accretion disk corona around SMBH	Aperiodic variability	Days–years
TDE	Stellar disruption by BH	Power-law decay	Days–months
Galaxies	Bremsstrahlung, line emission, and X-ray binary accretion	–	–
Galaxy Clusters	Thermal bremsstrahlung	–	–

Table 4.1: Summary of X-ray emitting objects with their optical variability features and timescales.

1 to 5 for each X-ray source, provided the source is detected with DET_LIKE_P[band] ≥ 7, for a moderate strength detection in that band. The distribution of positional errors in each catalog are plotted in Figure 4.1.

We then performed a 1.5 degree conesearch around the center of each of the 6 DP1 fields we include in our crossmatch to isolate only the X-ray sources near these fields, yielding 10,307 sources. We then de-duplicated the catalogs by crossmatching between all pairs of X-ray catalogs to get all sources that fall within the 95% error circle for another source. For 1:1 matches, we assume the two sources are the same and keep the source with the smaller positional uncertainty. For sources with multiple matches, we keep only the sources from the catalog with the smaller positional uncertainty. This leaves 9248 sources. We finally impose a 15" limit on the 95% error radius, which eliminates outliers and leaves 9089 total sources.

Finally, we eliminate all sources that are never observed as part of DP1. The data processing pipelines divide the celestial sphere into tracts, with each tract covering approximately

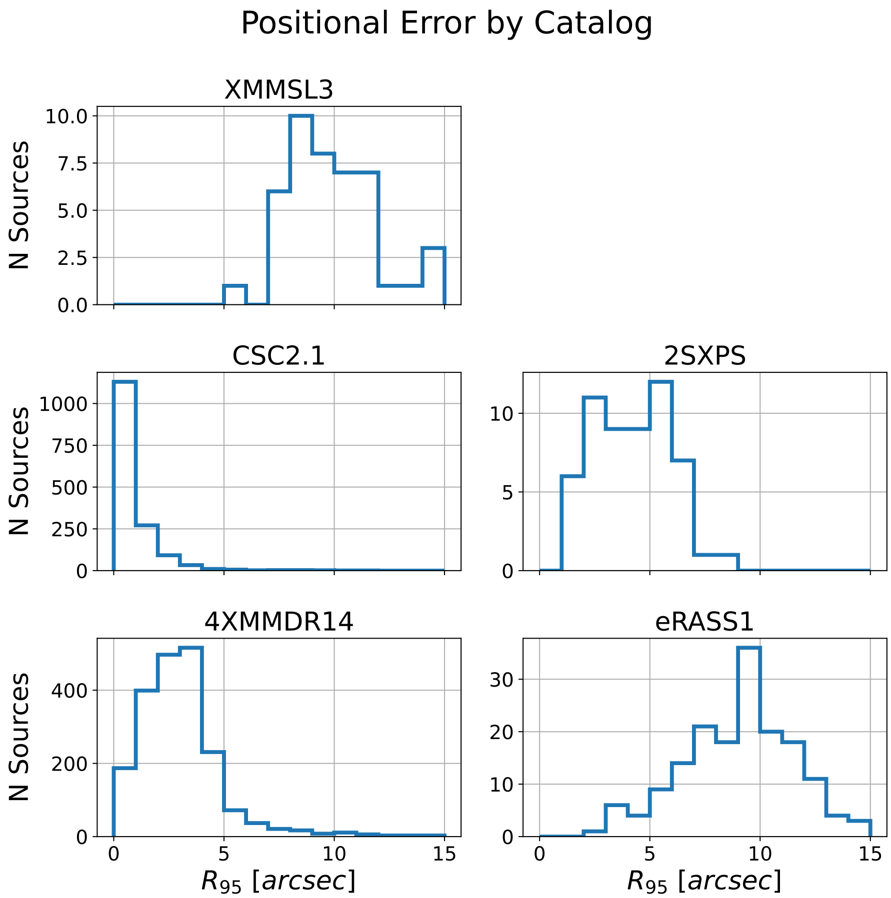

Figure 4.1: Histogram of R_{95} positional errors of all X-ray sources in DP1 observed fields by catalog.

2.8 deg^2. Each tract is then further divided into 100 equally sized patches in a 10 by 10 grid (NSF-DOE Vera C. Rubin Observatory, 2025a). We find the tract and patch of each position using the DP1 `skymap`, leaving a total of 4481 final sources in our X-ray catalog. The number of X-ray sources in each DP1 field, broken out by X-ray survey, is given in Figure 4.2.

2.2 Optical Catalog

The LSST Data Preview 1 (DP1) contains the first data collected by the Vera C. Rubin Observatory and offers the first look at the characteristics and capabilities of the data that will eventually be in LSST. The dataset consists of images taken by LSSTComCam between November 9 and December 12, 2024 and covers an area of approximately 15 sq. deg. We selected six of the fields observed by DP1: 47 Tucanae (47 Tuc), the Extended Chandra Deep Field South (E-CDF-S), the Euclid Deep Field (EDF-S), the Fornax Dwarf Spheroidal Galaxy (Fornax dSph), and two science validation fields, one at low galactic latitude (SV_95_-25) and one at low ecliptic latitude (SV_37_7) (NSF-DOE Vera C. Rubin Observatory, 2025a),

Catalog	Column	Significance / Range	Notes
CSC2.1	err_ellipse_r0	1.960σ (95%)	Major axis of the error ellipse
	flux_aper90_avg_b	0.5–7.0 keV	Background-subtracted, aperture-corrected, 90% ECF aperture
4XMMDR14	SC_POSERR	0.933σ (63%)	Weighted average of the total POSERR for source
	SC_EP_8_FLUX	0.2–12.0 keV	Mean, error-weighted combined band flux
XMMSL3	radec_err	1σ (68%)	Statistical error on source position from detection software
	flux_b8	0.2–12.0 keV	Total energy band flux
2SXPS	Err90	1.645σ (90%)	90% confidence radial position error on the source position
	PowFlux	0.3–10.0 keV	From power-law indicated by WhichPow
eRASS1	RADEC_ERR	1σ (68%)	Combined positional error, raw output from PSF fitting
	ML_FLUX_P[1..5]	0.2–8.0 keV	Sum of bands 1–5 where DET_LIKE_P[band] ≥ 7

Table 4.2: Positional uncertainty and flux column details for each X-ray catalog.

excluding the Seagull Nebula field which contains extensive nebulosity. These fields were observed repeatedly in the *ugrizy* bands over several nights. Observations were made in observing epochs on a given target field, with 5–20 visits in each of three loaded filters at a time. Each visit consists of one 30 second exposure covering approximately half a square degree.

The spatial distribution and coverage of the DP1 fields, and the temporal distribution of observations by field and filter can be found in the DP1 science paper (NSF-DOE Vera C. Rubin Observatory, 2025a, figures 4-6). The fields were not observed equally and in particular, the E-CDF-S field approaches 10 year survey depths. The number of visits per filter is given in Table 4.3. The cumulative imaging depth at S/N = 5 expressed as a limiting magnitude in each field exceeds 26th in the most observed regions in each field and is visualized in figure 3 of the *Rubin Observatory Plans for an Early Science Program* document (Guy et al., 2025).

For DP1 data, we adopt the Rubin convention of referring to a single-epoch detections within science images as a `Source` and the astrophysical object associated with a given detection as an `Object`. To draw this distinction, we refer to Rubin data products such as `Source`s and `Object`s in teletype for the remainder of the paper. In other words, every `Object` will usually have multiple associated `Source`s, with each `Source` corresponding to an observation in one single-epoch science image, also known as a `visit_image`. DP1 consists of five types of data products, which are described in detail in NSF-DOE Vera C. Rubin Observatory (2025a): images, catalogs, maps, metadata, and ancillary data products. We utilize the `Object` catalog (NSF-DOE Vera C. Rubin Observatory, 2025b), which contains 2,299,726

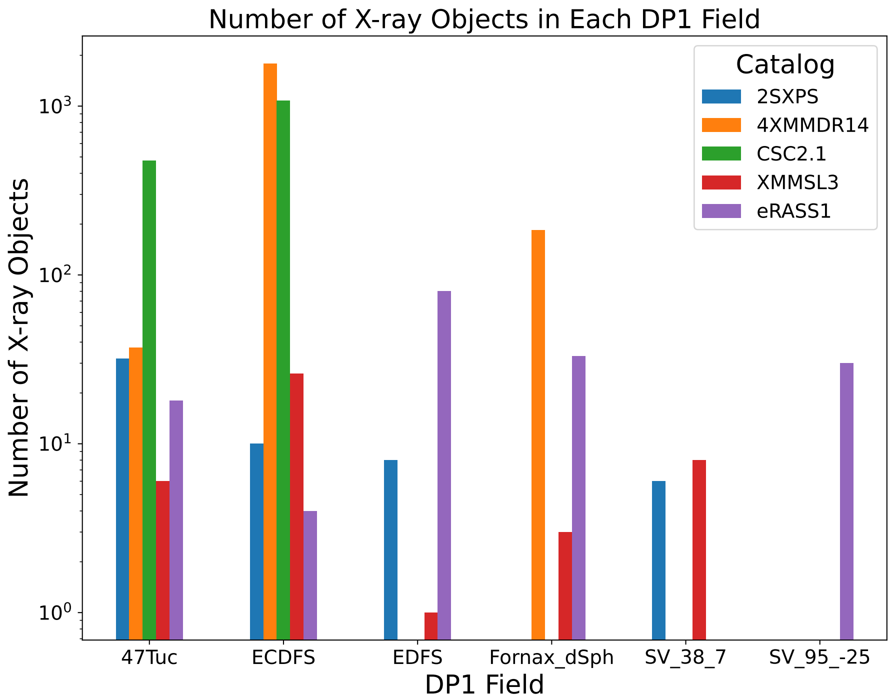

Figure 4.2: Number of X-ray sources by X-ray catalog in each DP1 field. The majority of X-ray sources are found in the Extended Chandra Deep Field - South (E-CDF-S), which is well observed by X-ray telescopes.

`Objects`—detections on `deep_coadd` images (NSF-DOE Vera C. Rubin Observatory, 2025c) made by stacking all available `visit_images` NSF-DOE Vera C. Rubin Observatory (2025d). To produce lightcurves and calculate time-series features, we require per-visit photometry. We use the `ForcedSource` catalog (NSF-DOE Vera C. Rubin Observatory, 2025e), which contains forced photometry at the position of detected `Objects` in each `visit_image`.

The Rubin difference image analysis (DIA) pipeline also detects sources in `difference_images` (NSF-DOE Vera C. Rubin Observatory, 2025f), known as `DiaSources` (NSF-DOE Vera C. Rubin Observatory, 2025g). By associating `DiaSources` at the same position, the DIA pipeline also builds `DiaObject` catalogs. We also crossmatch to this catalog, which contains 1,089,818 `DiaObjects` (NSF-DOE Vera C. Rubin Observatory, 2025h). The DIA pipeline bypasses the deblending step that fails in the densest crowded fields (Choi et al., 2025), such as inner regions of the 47 Tuc and Fornax dSph fields. Other studies have shown that matching to the `DiaObject` table can recover photometry from some of the denser fields (Wainer et al., 2025). More discussion of the `DiaObject` catalog match is found in 4.4.

DP1 catalogs are a proprietary data product with access specified by the LSST data rights policy (Blum & the Rubin Operations Team, 2020). Rubin data rights holders can run our code, available at Wang (2026), on the Rubin Science Platform (RSP) to replicate our analysis.

Target	u	g	r	i	z	y
47 Tuc	6	10	33	19	0	5
Rubin SV 38 7	0	44	55	57	27	0
Fornax dSph	0	5	26	13	0	0
E-CDF-S	53	230	257	177	177	30
EDF-S	20	61	90	42	42	20
Rubin SV 95 -25	33	86	97	29	60	11

Table 4.3: Number of visits by field for DP1.

2.3 Crossmatch to `Object` table

LSDB was developed by the LSST Interdisciplinary Network for Collaboration and Computing (LINCC) Frameworks project to enable scalable analysis of large catalogs (Caplar et al., 2025). We use the LSDB Hierarchical Adaptive Tiling Scheme (HATS) formatted DP1 `Object` catalog (Malanchev et al., 2025) and the LSDB crossmatch function to crossmatch the combined X-ray catalog to all `Objects` detected in the six DP1 fields. We set the match radius to 15″ and return up to the 10 closest matches for each X-ray source. We then eliminate all matches where the candidate optical counterpart does not fall within the 95% error radius of the X-ray source. We are left with 4513 candidate `Object` counterparts for 2314 unique X-ray sources.

Since we had narrowed down our catalog of X-ray sources by keeping all sources in tracts and patches observed by LSSTComCam, some of these sources are just past the outskirts of the DP1 fields and are not in the observed footprint. To further eliminate these sources, we find the convex hull, the smallest convex polygon that encloses all matches in each field. We then assume that sources interior to the convex hull were observed as a part of DP1 and are therefore optical nondetections. This eliminates 651 of the X-ray sources and leaves us with a final total of 3830 X-ray sources in the footprint of DP1.

Lastly, we repeat the crossmatching, adding 30″ to the declination of each X-ray source to obtain a random set of matched `Objects`, so we can compare our matches to a control sample of field objects.

2.4 Evaluation of crossmatch reliability

We calculate the reliability[1], which we define as the probability of finding no chance object closer to the X-ray source than the counterpart `Object` (Sutherland & Saunders, 1992). The expected number of background sources within the separation between the source and counterpart is:

$$Y = \pi d^2 \cdot N, \tag{4.1}$$

[1]The crossmatch reliability should not be confused with the Rubin-reported reliability score for `DiaSources`, which is a machine-learned probability that a given `DiaSource` is astrophysical in origin.

where item Y is the expected number of background sources, d is the separation between the source and counterpart, and N is the local background source density (Sutherland & Saunders, 1992). We calculate the background by counting the number of `Objects` in an annulus with an inner radius of the 4 σ X-ray error circle, $R_{4\sigma}$, and outer radius of $R_{8\sigma}$ around each counterpart. We obtained these radii by scaling up the $R_{1\sigma}$ calculated in Section 2.1. We set the inner radius to $R_{4\sigma}$ in order not to bias the number density by including the real counterpart. If there are no `Objects` in the annulus, we increase the outer radius by 10 arcsec until we have at least one. Assuming Poisson statistics, the reliability of the match is given by

$$\text{Reliability} = \Pr(0, Y) = e^{-Y}. \tag{4.2}$$

2.5 Quantifying variability

We also calculate the Stetson J index to quantify the variability of each potential counterpart (Stetson, 1996). Let the standardized residual for observation i be defined as

$$\delta_i = \sqrt{\frac{n}{n-1}} \cdot \frac{\nu_i - \bar{\nu}}{\sigma_i}, \tag{4.3}$$

where ν_i is the observed value (e.g., flux or magnitude), $\bar{\nu}$ is the weighted mean value, σ_i is the uncertainty in ν_i, and n is the total number of observations in the band. Since each LSSTComCam epoch consists of a single observation, we define the product P_i

$$P_i = \delta_i^2 - 1. \tag{4.4}$$

The Stetson J index is then defined as

$$J = \frac{1}{N} \sum_{i=1}^{N} \operatorname{sgn}(P_i) \cdot \sqrt{|P_i|}. \tag{4.5}$$

We calculate the Stetson J index in each band using the `psfFlux` and `psfFluxErr` columns from the forced source table for each `Objects`.

2.6 Value added crossmatches to SIMBAD, Milliquas, Gaia

After we obtained the crossmatch between DP1 `Objects` and our X-ray catalog, we also matched these `Objects` to several other catalogs to provide additional context to our matches and to build up a value-added catalog. We used LSDB to find all Gaia DR3 sources (Gaia Collaboration et al., 2023), within 0.5arcsec of the LSST DP1 objects. Since Gaia provides parallaxes and distances, we can use the data to distinguish between Galactic and extragalactic objects for some of the brighter `Objects`. We also find all DP1 sources within 2arcsec of any Gaia source brighter than 15th magnitude—these `Objects` are flagged because they may either be saturated, or have inconsistent photometry due to the nearby presence of a bright star.

We also crossmatched the positions of the optical LSST DP1 objects to the Million Quasar (Milliquas) catalog (Flesch, 2023), using radius of 1″ since most of the objects in the catalog are sourced from optical surveys with high precision, such as Gaia eDR3, DESI, and SDSS-DR18. We expect many of our matches in the E-CDF-S and EDF-S fields, which are away from the galactic plane, to be extragalactic, and this crossmatch will enable us to compare the properties of known active galaxies to our broader set of matches.

Lastly, we used astroquery (Ginsburg et al., 2019) to query any existing object type (otype) from SIMBAD (Wenger et al., 2000) within 1″ of the position of the `Object` location, and any associated photometry in the *ugri* and *V* bands. We then drop duplicate matches such that all remaining matches are between one SIMBAD source and one DP1 `Object`.

3 Results

3.1 Crossmatch results

A total of 4513 candidate `Objects` are found within the 95% error radius for 2314 unique X-ray sources, as some X-ray sources have multiple DP1 `Objects` within the R_{95}. Figure 4.3 shows the locations of all objects in the original combined X-ray catalog from Section 2.1 that were observed in the DP1 fields, as well as whether a counterpart was identified in DP1. 1600 X-ray sources did not have a counterpart in the DP1 `Objects` table. Many of the unmatched X-ray sources lie in the cores of 47 Tuc (466/567) or the Fornax dSph galaxy (129/220), where the LSST pipeline performance is reduced due to the high stellar density and there are no `Objects` detected. Additionally, 669 out of 2910 sources in the E-CDF-S field have no match in our crossmatched dataset. We find matches for all X-ray sources in the EDF-S field, the low galactic latitude science validation field (SV_95_-25), and the low ecliptic latitude field.

The magnitude distribution of the counterparts in each field can be seen in Figure 4.4. Taking fiducial limiting magnitudes of 21, 23, and 24 for Gaia (Gaia Collaboration et al., 2023), SDSS (York et al., 2000), and PanSTARRS (Kaiser, 2004), we find that 78%, 45%, and 27% of DP1 objects were fainter than these surveys, respectively, in all bands. This indicates that during the full survey, we should expect to vastly increase the number of X-ray counterparts.

The total numbers of matches broken out by field and instrument are given in Table 4.4. We also present the number of matches to external catalogs: Milliquas, Gaia, and SIMBAD, by field. We find a total of 444 matches between our DP1 `Objects` and the Milliquas catalog, 345 between our DP1 `Objects` and Gaia DR3, and 1046 unique matches between our DP1 `Objects` and SIMBAD.

3.2 Reliability of crossmatch

Next, we look at the reliability of crossmatch for the most likely counterpart for each unique X-ray source. The reliability is influenced both by the radius of separation between the X-ray source and DP1 match and the local density. As expected, the fields with the most constrained X-ray observations - those made by *Chandra* and *XMM-Newton* - have the highest proportion of high reliability matches.

Feature	Subset	Field						Total
		47 Tuc	E-CDF-S	EDF-S	Fornax dSph	SV 38_7	SV 95_-25	
X-ray sources	...	567	2910	89	220	14	30	3830
X-ray sources with `Object` match	2SXPS	0	8	8	0	6	0	22
	4XMMDR14	4	1279	0	2	0	0	1285
	CSC2.1	3	821	0	0	0	0	824
	XMMSL3	2	24	1	3	8	0	38
	eRASS1	10	4	76	27	0	28	145
	Total	19	2136	85	32	14	28	2314
X-ray sources with `DiaObject` match	...	91	810	64	71	10	21	1067
Any `Object` or `DiaObject` match	...	101	2241	89	91	14	30	2566
No `Object` or `DiaObject` match	...	466	669	0	129	0	0	1264
$\boldsymbol{N}_{\texttt{Object}}$ in R_{95}	...	75	3560	429	195	57	197	4513
$\boldsymbol{N}_{\texttt{DiaObject}}$ in R_{95}	...	249	1587	176	106	31	127	2276
Crossmatch reliability	$> 90\%$	8	1295	21	10	3	7	1344
`refExtendedness`	point-like (0)	7	379	23	14	1	8	432
	extended (1)	7	1617	53	16	10	11	1714
	unknown (NA)	5	140	9	2	3	9	168
External xmatches	Gaia	10	235	45	19	8	28	345
	Milliquas	2	434	3	0	5	0	444
	SIMBAD	1	1036	2	1	2	4	1046

Table 4.4: Breakdown of matches by field. The first section details the number of X-ray sources with DP1 `Object` matches (detections in `deep_coadds`) for each X-ray catalog, and the X-ray sources with matches to `DiaObjects` (detections in `difference_images`). Since some sources are only detected in either the `deep_coadds` or `difference_images`, as seen in Figure 4.3, we also present numbers of X-ray sources with any `Object` or `DiaObject` match, as well as those with no match. The second section gives the total numbers of `Objects` and `DiaObjects` found in the 95% error radius of any X-ray source—some sources having multiple matches. We also show the number of high reliability matches ($> 90\%$), the number of point-like vs. extended `Objects`, and the number of `Objects` with matches to external catalogs

Figure 4.5 plots the distribution of reliability in each field. We define a match where the probability of a chance association is less than 10%, i.e. the reliability $\geq 90\%$ to be a high-reliability match and we create a subset of 1344 matches meeting this criteria. The E-CDF-S field has the highest proportion of reliable matches, with a total of 1295, or 60.6% of all matches in that field. On the other hand, the proportion of reliable matches is much

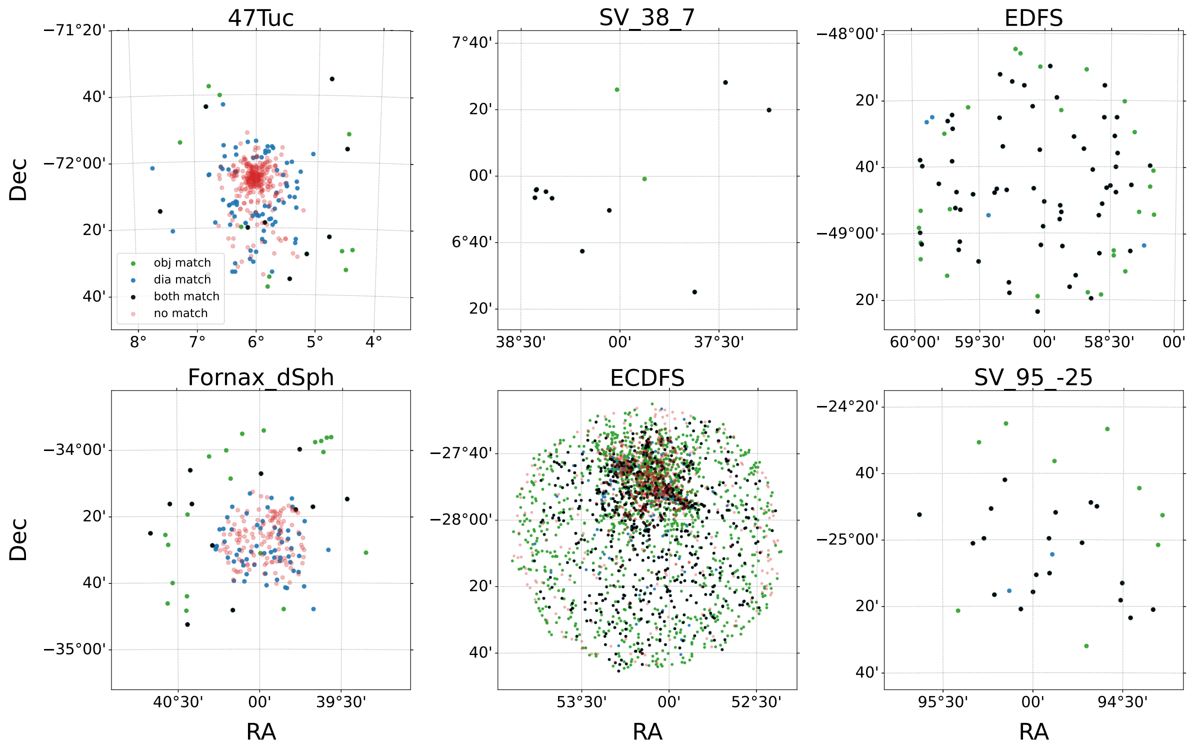

Figure 4.3: Spatial distribution of all X-ray sources in the combined X-ray catalog. Matches to `Objects` are colored green. We also crossmatched `diaObjects`, which are detections based on `difference_images`. X-ray sources only detected in the `DiaObject`catalog are plotted in blue and sources found in both catalogs are plotted in black. X-ray sources with no optical match in DP1 are plotted in red. Due to the crowdedness of the 47 Tuc and Fornax dSph fields, we have better success matching to the `DiaObject` table (see Section 4.4). Many of the unmatched sources are also in the cores of these two fields for the same reason.

lower in the EDF-S and the two science validation fields at between 21% and 25%.

The calculation of the reliability depends on an accurate measurement of the background source number density. This in turn assumes that the `Object` catalog has high completeness—otherwise the density will be underestimated and the reliability will be falsely high. Because we know that the two crowded fields 47 Tuc and Fornax dSph may not meet this requirement, we should treat the reliabilities calculated in these fields with caution.

We also find that due to the definition of our reliability criteria, the X-ray positional error and the local density of `Objects` has the greatest impact on reliability, with well localized sources in less crowded areas having the highest reliability scores. Figure 4.6 plots the fraction of X-ray sources with any counterpart in DP1, as well as the fraction of sources with a reliable counterpart. We see that the fraction of sources with a match and a reliable match tend to fall off with X-ray flux in non E-CDF-S fields. In these fields, most of the X-ray sources are from eROSITA and the XMM slew surveys, which are less sensitive and have comparatively poorer localizations when compared to sources in CSC2.1 and XMMDR14 catalogs, and there are very few sources fainter than $10^{-15}\,\mathrm{ergs^{-1}cm^{-2}}$. The uppermost

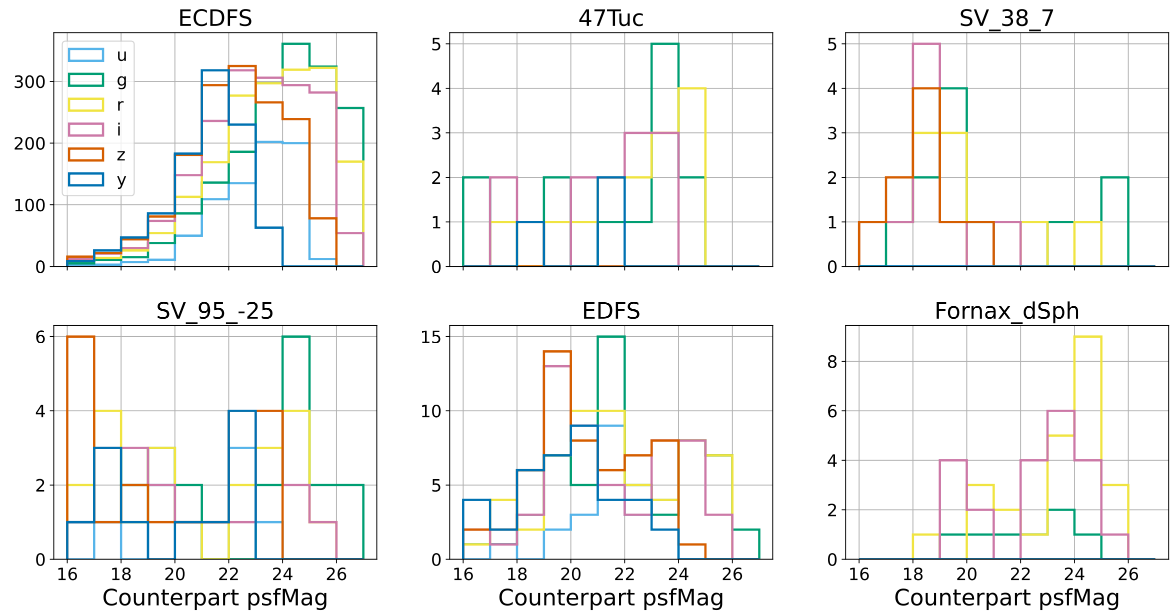

Figure 4.4: The magnitude distribution of the counts of candidate counterparts in each of the 6 fields, by band. Many of the crossmatched counterparts are fainter than the Gaia, PanSTARRS and SDSS limiting magnitudes. Only measurements where the SNR $\geq$ 5, where SNR = `psfFlux`/`psfFluxErr` are in the histograms.

subplot is dominated by matches in the E-CDF-S field, where most matches are to sources in the CSC2.1 and XMMDR14 catalogs, which are fairly well localized. This leads to an increase in sources with reliable matches at lower fluxes, as these sources tend also to be observed out of these catalogs.

4 Discussion

4.1 Comparison to E-CDF-S crossmatch in Luo et al. (2017)

Out of 1055 total objects in the E-CDF-S X-ray catalog in Luo et al. (2017), we find 777 counterparts in the `Object` catalog within the 2σ error radius and 900 counterparts in the 3σ error radius. Of the remaining 155 *Chandra* sources, 79 are only detected in bands with wavelength longer than LSST y-band, or have no optical or IR counterpart in the original study either. The final 75 sources with Hubble Space Telescope (HST) counterparts in either R or z band only contains 21 sources brighter than 24th magnitude. We also have one match (`LSST-DP1-O-611255759837095315`) to one of the 16 X-ray sources with no match in the original paper (No 896). We find that $log(F_X/F_{r\_psfFlux}) = -0.84 > -1$, and the DP1 `refExtendedness` parameter for this `Object` is 1, i.e. extended, which satisfies two of the criteria in the paper for an active galactic nucleus (AGN) classification.

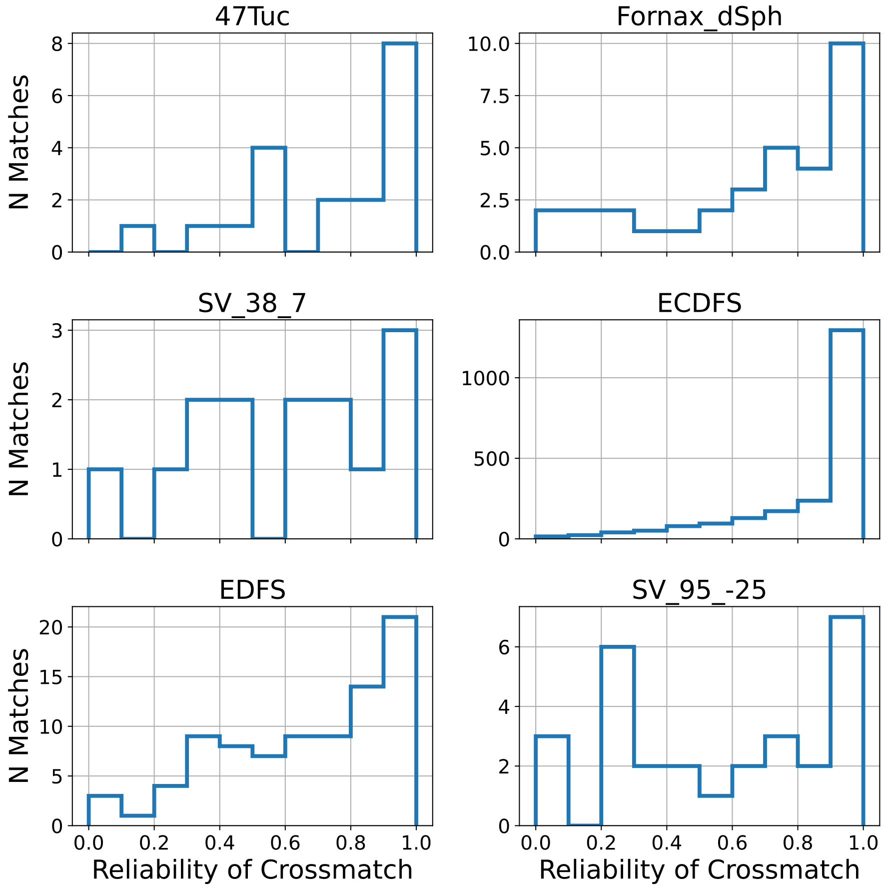

Figure 4.5: The reliability of crossmatch of the closest counterpart to each X-ray source, broken out by field. The reliability is the probability the counterpart is not a random association.

4.2 Variability

We also examine whether the Stetson J index has any relation to the reliability of the closest `Object` counterpart, to test our hypothesis that the optical counterparts to X-ray sources will tend to be more variable. As an example, we plot the lightcurve of high-reliability match with the largest r-band Stetson J in Figure 4.7. This turns out to be the SU UMa type cataclysmic variable CRTS J033349.8-282244 (Drake et al., 2014; Kato et al., 2017), which completed a full outburst cycle during commissioning observations, and was also found by Malanchev et al. (2025) in their variability search. We also plot the lightcurve of one AGN, 3D-HST 38237 in the Milliquas catalog, with a fairly large Stetson J. We note that for both objects, the intra-day variation in each band much greater than the estimated error, hinting at possible systematics in the PSF photometry of these bright objects.

Plotting the reliability of crossmatch against the Stetson J index in Figure 4.8, we find that there appears to be no strong association between these two metrics in the left subplot. Instead, our Stetson J appears correlated with the magnitude of the `Object`. Additionally, almost all objects brighter than 20th magnitude have Stetson $J > 1$. The intra-day variation

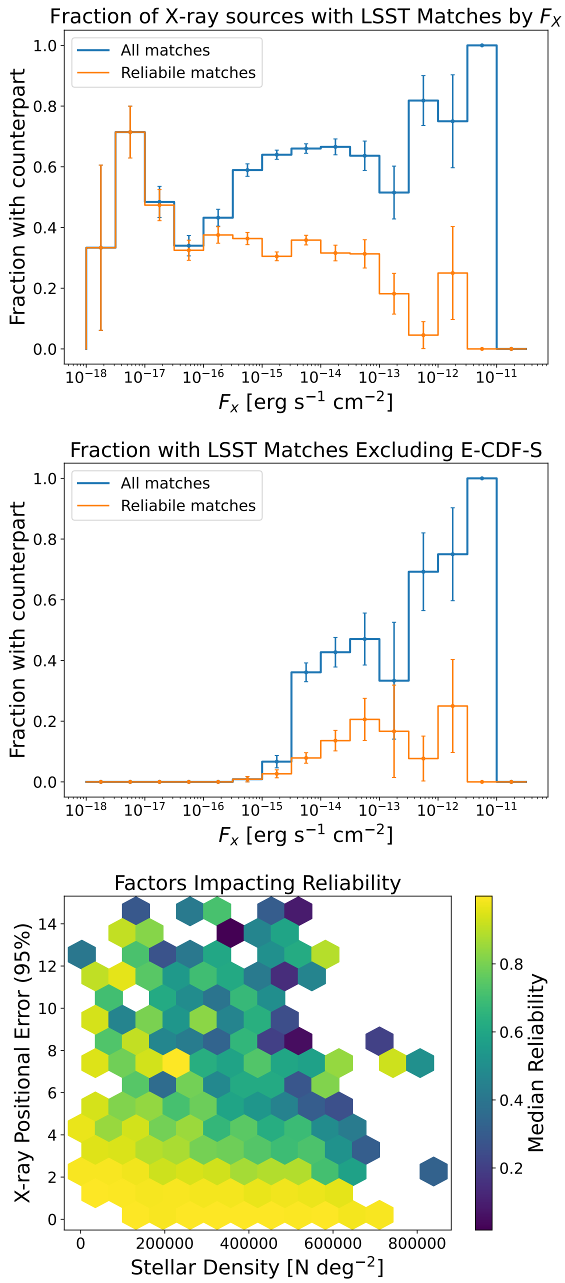

Figure 4.6: Top: The fraction of sources in each X-ray Flux bin with a match and with reliable match in the DP1 `Object` catalog. The error bars show the standard error. The fainter X-ray sources are dominated by sources from the CSC2.1, which are generally well localized, leading to an increase in fraction of sources with reliable matches. Middle: Excluding the E-CDF-S field, which is both the best observed by X-ray observatories and by DP1, we see that the fraction falls off strongly with absorbed X-ray flux. This is more indicative of what we expect a crossmatch to early Rubin (e.g. DR1) data may look like. Bottom: The main factors impacting our reliablity score are the X-ray positional error and the density of `Objects` around the X-ray source.

visible in each band in the lightcurves in figure 4.7 suggest that systematics may play a role in the larger Js at brighter magnitudes. We expect these sources to be fairly stable in brightness over the course of each set of same-band observations, which are observed in blocks of 5-20 visits, lasting a total of less than an hour each.

We perform a 2-sample KS-test with the null hypothesis that the distribution of Stetson J for field `Objects` is the same or greater than as the distribution of Stetson J for our matches. Due to the magnitude dependence of the Stetson J, we perform this test on samples for matches and field objects of magnitude 17 to 25 in bins of width 2 magnitudes. We also split the samples into *ugri* bands, for a total of 12 tests. We set our overall threshold $\alpha = 0.05$ for rejecting the null hypothesis and apply the Bonferroni Correction to obtain a per-test threshold of $\alpha/m = 0.0042$, where m is the number of hypotheses. We find that since we reject the null hypothesis for only two of these subsets at the $p < 0.0042$ level, so we have at best weak evidence that the matches are more variable than the field `Objects`.

We repeat the procedure above, comparing the distribution of Stetson J index for reliable matches against the distribution for matches that do not meet our reliability criteria. Here, we find that we reject the null hypothesis for only one of these subsets at the $p < 0.0042$ level, so we again have minimal evidence that the reliable matches are more variable than the unreliable matches.

The dense cadence of the commissioning observations means the Stetson Js are most sensitive to variability on timescales of seconds to days, since the majority of the DP1 observations will be on these timescales. This differs from much of the expected longer variability timescales of most X-ray counterparts, particularly AGN (see table 4.1), which we expect to make up the vast majority of our counterparts.

The optical variability of an AGN is commonly quantified with the (noise-subtracted) structure function (SF), which describes how the typical magnitude change grows with the time lag Δt between two observations. For a light curve in magnitudes $m(t)$ with measurement uncertainties σ_{noise}, we take the definition of the structure function by di Clemente et al. (1996):

$$\mathrm{SF}(\Delta t) \equiv \sqrt{\frac{\pi}{2} \left\langle \big(m(t+\Delta t) - m(t)\big) \right\rangle^2 \; - \; \langle \sigma_{\mathrm{noise}} \rangle^2}, \tag{4.6}$$

where $\langle \cdot \rangle$ denotes an average over all pairs of epochs separated by Δt. The factor $\frac{\pi}{2}$ is included assuming that both the intrinsic variability and the observational noise follow Gaussian distributions. Intuitively, $\mathrm{SF}(\Delta t)$ is the intrinsic root-mean-square magnitude difference on timescale Δt, after accounting for photometric noise.

De Cicco et al. (2022) used 3.3 years of VLT Survey Telescope (VST) COSMOS data to quantify AGN optical variability at LSST depths. The maximum baseline for *Object*s in the DP1 dataset with a reliable counterpart to a known AGN is 32 days. Using the structure functions obtained from their data, we would expect a difference of around 0.1 magnitudes for a 32 day time difference.

To evaluate the expected Stetson J statistic, we used 100 mock AGN lightcurves from Fagin et al. (2025) observed with a daily cadence for 32 days at fiducial uncertainty of 5 mmags to calculate a median Stetson J of 3. While this number is low, it also differs significantly from our observed sample, where only 10% of our reliable matches to AGN have a Stetson J greater than 3. However, by changing the fiducial uncertainty to 0.03 mag, we find a similar simulated distribution of Stetson J as our observed sample.

Using the same mock AGN lightcurves, we also simulated full 10 year lightcurves with observations at LSST Wide Fast Deep (WFD) cadence from the v5.0.0_10yrs baseline, incorporating Rubin errors using the Rubin Operations Simulator (OpSim) (Reuter et al., 2016). The median r-band Stetson J over this baseline is 18.0, and the median Stetson J after one year is 13.0. Thus the upcoming LSST survey will probe nearly the full range of variability timescales, and so similar analyses may be more informative in the future, including after the release of DR1.

4.3 Plots in optical-X-ray parameter space

A full classification of all the X-ray sources with DP1 counterparts is beyond the scope of this paper. However, we take advantage of our crossmatch to the Milliquas catalog and our SIMBAD queries to show where a sample of objects of known object type lie in our optical-X-ray parameter space. In Figure 4.9, we make two sets of two plots each. On the left, we plot "control samples" of classified objects. On the right, we plot all matched DP1 `Object`s that have a reliability greater than 90%.

The top left subplot shows our 444 `Object` sample of matches to the Milliquas catalog in the i-magnitude / X-ray broadband flux plane, similar to figure 3 in Hasinger (2008). Our results are consistent, with most sources falling between the lines of constant X-ray to optical flux ratio of $\log(F_X/F_{opt}) \pm 1$, where F_{opt} is the optical flux over all available *ugrizy* bands. For sources with fluxes between 10^{-14} and $10^{-12}\,\mathrm{erg\,s^{-1}\,cm^{-2}}$. Below $10^{-14}\,\mathrm{ergs^{-1}cm^{-2}}$ it appears some of the AGN in our sample have smaller $\log(F_X/F_{opt})$. We also see much more scatter in the top right plot, even though we expect most of the sources to be extragalactic as well.

The bottom left subplot shows the log flux ratio $\log(F_X/F_{opt})$ against the color. We choose to plot $g-i$ color, and plot the empirical cut from Rodriguez (2024) onto our subplot using the following transformation:

$$y = -0.079 + 1.184x + 0.2218x^2 - 0.1013x^3 \tag{4.7}$$

where y is LSST $g-i$ color and x is Gaia $BP-RP$, for x between approximately -1 and 2 (Gwyn, 2024). This cut and diagram, termed the X-ray Main Sequence, is a useful tool for separating Galactic X-ray sources into stellar and compact object regions. Although the vast majority of our sources are extragalactic, we plot our Milliquas matches plus a handful of known Galactic stars and one cataclysmic variable (CRTS J033349.8-282244). We note that this CV was actually in outburst (see Figure 4.7), and we calculate the optical flux and color in quiescence by selecting the forced photometry before and after the outburst. The known stars fall on the opposite side of the cut as the CV. We also see that the quasi-stellar objects (QSOs) are much bluer and have a higher flux ratio than the AGN.

On the bottom right, we again plot the matched DP1 `Object`s that have a reliability greater than 90% in the same parameter space. On color, we have the `refExtendedness`, a measure of whether the DP1 `Object` is point-like (0) or extended (1). These classifications are roughly meant to correspond to star-like and galactic sources. However, from our sample of known sources, we find that this is not always dependable, as QSOs are classified as point-like about 1/3 of the time (77/221). We also notice that our CV is classified as an"extended"

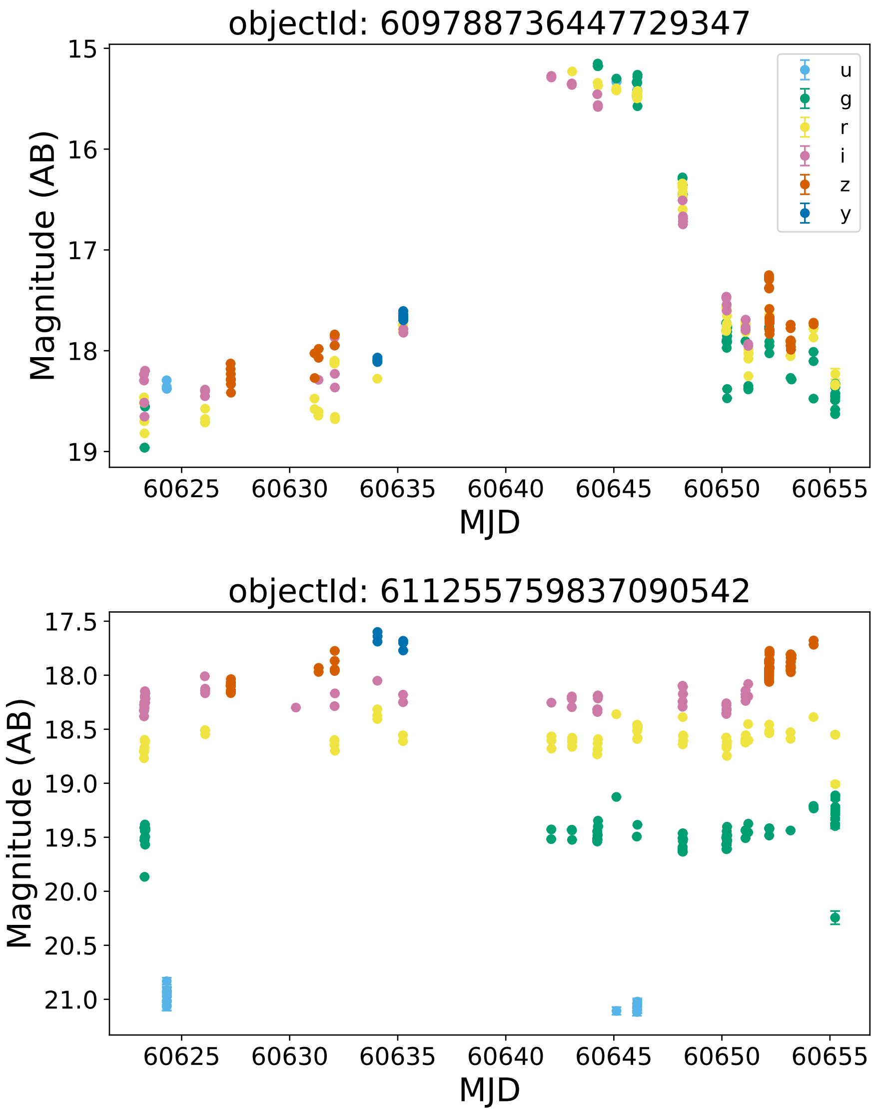

Figure 4.7: Example lightcurves of our counterparts. The top plot shows the SU UMa type cataclysmic variable CRTS J033349.8-282244, which was observed in outburst. This `Object` had a r-band Stetson J of 450, highest out of all of our high-reliability matches. The bottom plot shows the AGN 3D-HST 38237, an AGN with a r-band Stetson J of 24.

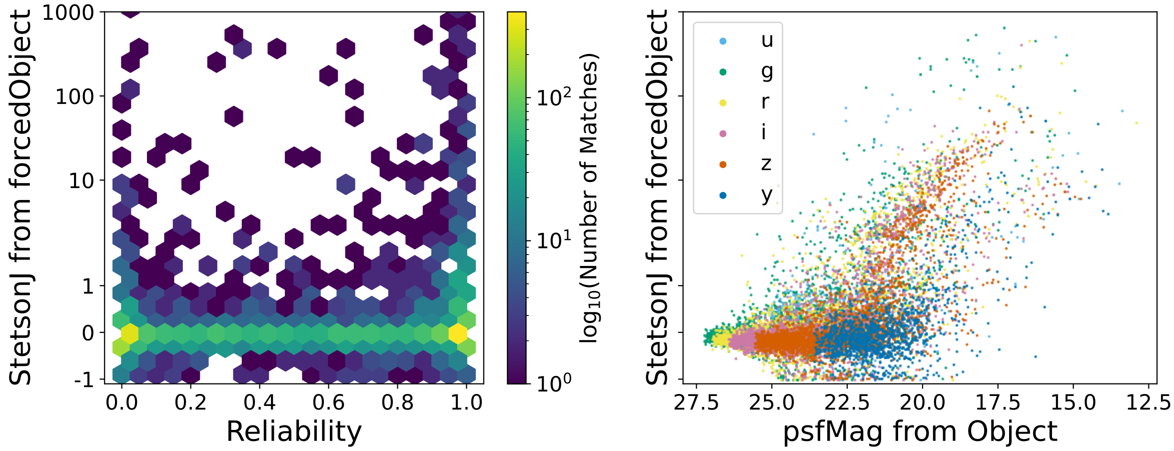

Figure 4.8: There may be a slight association between the reliability of a crossmatch and the Stetson J index of the object, as seen in the histogram on the left. The Stetson J appears to increase with a subset of brighter `Object`s, shown by the spur in the right plot. A possible explanation for the spur is a systematic underestimate of the photometric error. We use a symmetric logarithmic (symlog) scale for the y-axis.

source as well. For future followup, we would begin by selecting the set of sources in the upper right of the plot with point-like `refExtendedness` and in fields other than E-CDF-S and EDF-S for investigation as potential accreting systems.

4.4 `difference_images` and crossmatch to the `DiaObject` catalog

DP1 also contains catalogs of detections by the Difference Image Analysis pipeline (DIA) in the `difference_images`. Detections on individual `difference_images` are known as `DiaSources` and the difference image analysis pipeline associates `DiaSources` together to create a catalog of `DiaObjects`, the equivalent to the `Object` table for difference image analysis. We expect transients and variables to show up in the `DiaObject` catalog and thus this is another way to assess whether an `Object` is variable. Similar to the `ForcedSource` catalog, DP1 also includes a `ForcedSourceOnDiaObject` (NSF-DOE Vera C. Rubin Observatory, 2025i) catalog containing forced photometry on the `visit_images` at the location of each `DiaObject`. Additionally, the `DiaSource` catalog contains all photometry of each `DiaSource` that is associated with a given `DiaObject`.

We crossmatch the locations of all the X-ray sources to the `DiaObject` catalog and find 2276 candidate `DiaObjects` for 1067 unique X-ray sources. 815 X-ray sources have counterparts in both the `Object` and `DiaObject` catalogs, although we cannot confirm that the `DiaObject` and `Object` are the same astronomical object for all 815 sources. Thus, of the 3830 X-ray sources in the combined X-ray catalog, 2566 have at least one match between the `Object` and `DiaObject` tables. We note that many X-ray sources in the 47 Tuc and Fornax dSph fields only have matches to the `DiaObject` catalog.

Since there is no `difference_image` equivalent to a co-added image, we calculate the error-weighted mean magnitude in each band of every `DiaObject` using the `psfMag` and

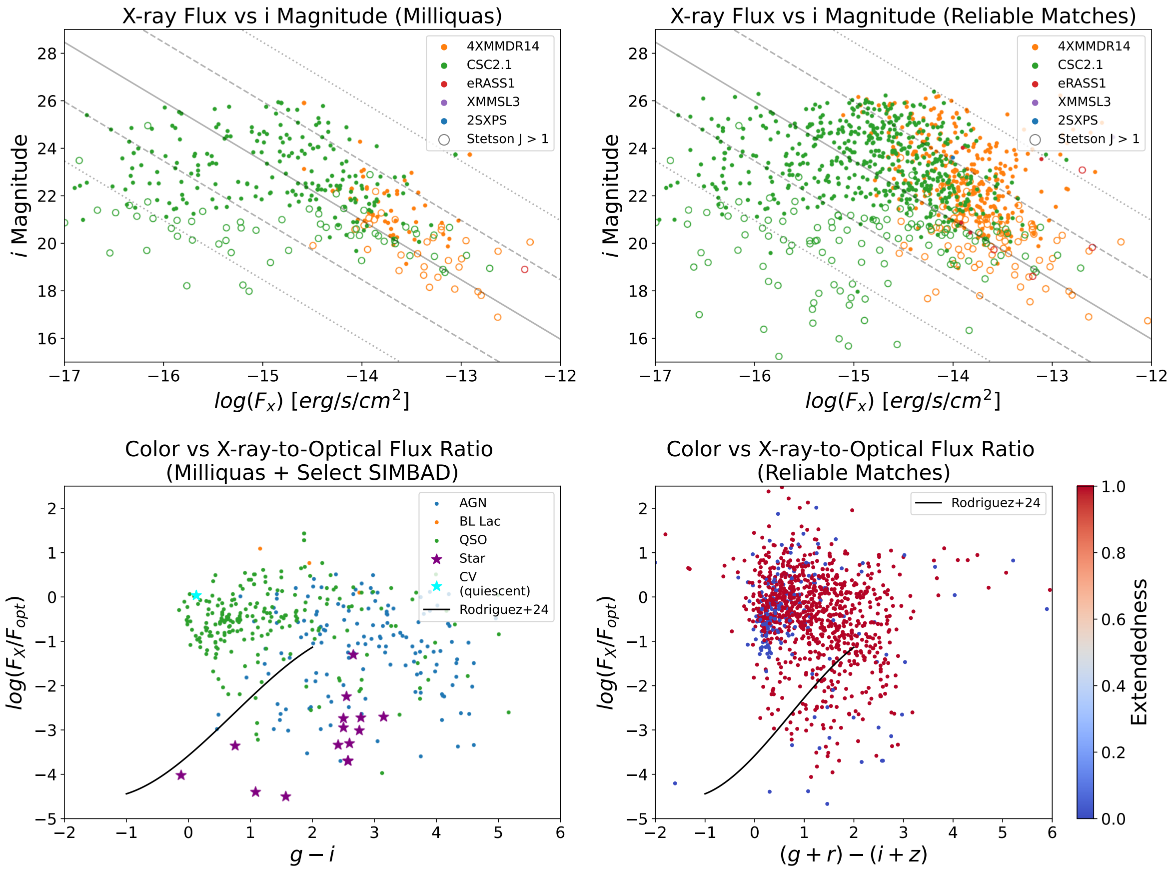

Figure 4.9: TOP: On the left, we plot the X-ray flux vs i-band magnitude, only for objects with matches to the Milliquas catalog. The solid grey line delineates $\log(F_X/F_{opt}) = 0$, and the dashed and dotted lines are at log flux ratios of ±1 and ±2 respectively. Most of the X-ray bright galaxies fall between ±1, as expected for AGN. We expect many of the matches with $\log(F_X/F_{opt}) < -1$ to be galaxies. The right plot shows all matches with reliability $> 90\%$, a total of 1344 `Objects`, on the same axes. The open circles show matches with some optical variability as defined by Stetson J; however, it appears there is a strong correlation between optical magnitude and Stetson J as mentioned previously. BOTTOM: We plot the X-ray-to-optical flux ratio against color. The left plot contains matches to Milliquas, plus some stars from SIMBAD and Gaia, and one CV (CRTS J033349.8-282244). The right plot again shows all matches with reliability $> 90\%$ on the same axes. Extendedness measures whether the matched DP1 `Object` is point-like (0) or extended (1). We use color transformations as defined in our Equation 4.7 to plot the empirical cut from Rodriguez (2024).

psfMagErr columns in the ForcedSourceOnDiaObject table as the per-band photometry of each DiaObject.

5 Conclusions

We performed a crossmatch between a consolidated catalog of all objects in the DP1 fields in five X-ray catalogs to DP1 Objects and diaObjects. Our results demonstrate that we are able to find many candidate counterparts with high reliability. Many of the candidate counterparts are fainter than Gaia, PanSTARRs, and SDSS limiting magnitudes. We find that 2566 out of 3830, or roughly 67% of our X-ray sources have a match in one of the DP1 catalogs. After examining the X-ray to optical flux ratios of these matches, we do not follow up any of these sources at the present. A list of X-ray sources with optical non-detections, which may also be of interest for future followup, can be found in the linked GitHub.

Many previous studies with deeper X-ray to optical crossmatches focus on a specific field such as E-CDF-S (Luo et al., 2017), the Lockman Hole (Bykov et al., 2022; Salvato et al., 2018), or the galactic bulge (Wevers et al., 2016). The LSST DP1 dataset contains six fields with very different density, observing depth, and coverage by X-ray catalogs, and we attempted to apply the same crossmatching procedure to each field. We find that many of our crossmatches are reliable in fields that are well observed by X-ray missions, i.e. the E-CDF-S field and that in this field, the percentage of X-ray objects with a reliable counterpart does not seem to depend on its X-ray flux. In the non-crowded fields where we expect the completeness of the Object catalog to be high, we find that at roughly 20% of our matches met our criteria for reliability when the X-ray flux exceeds $10^{-13}\,\mathrm{ergs^{-1}cm^{-2}}$, and steadily drops off to zero for the faintest sources in these fields, at $10^{-15}\,\mathrm{ergs^{-1}cm^{-2}}$. Observations in these fields are primarily from eROSITA, and are limited by the sensitivity and the positional error of the eRASS1 data.. In the crowded fields 47 Tuc and Fornax dSph, the majority of matches are found only on diaObjects, which bypass the deblending on co-add image step of the pipeline. We expect that it will be feasible to build up the large datasets of reliable optical-X-ray matches across the LSST all-sky survey to extract the local magnitude and sky density by magnitude distributions needed to implement and train more sophisticated crossmatching models but that this will require much larger survey area than the current DP1 fields. For example, Euclid Collaboration et al. (2025) use an X-ray emitter prior in their crossmatch between X-ray sources and Euclid data based on a machine learning algorithm.

The variability quantified by the Stetson J index does not appear to strongly correlate with the reliability of the crossmatch in the DP1 data, and it remains inconclusive whether increased optical variability can indicate a higher likelihood counterpart, despite our expectation that should be the case. As the Rubin data processing continues to be improved we will check back to see if this effect persists. Additionally, the continuous cadence of the commissioning observations mean the Stetson Js are most sensitive to variability on timescales of seconds to days, since the DP1 observations were on these timescales. This differs from much of the expected longer variability timescales of most extragalactic X-ray counterparts. However, the upcoming LSST full survey will probe nearly the full range of variability timescales and we plan to redo this analysis in the future once the survey is underway.

Overall, while challenges remain, the DP1 data shows promise for X-ray optical association. Continued improvements to the Rubin Science Pipelines and in-kind programs, particularly those dedicated to crowded-field stellar photometry, are expected to deliver even better results in future data previews and data releases. These broader datasets should permit the utilization of more advanced statistical and machine learning based crossmatching techniques that can that will enable comprehensive classifications of X-ray sources and searches for rare and exotic new objects.

CHAPTER 5

CONCLUSIONS

The purpose of this thesis is to outline our efforts to advance our understanding of the galactic population of low mass X-ray binaries from both a theory and observational perspective. For observations, I focus specifically on how the advance in time domain astronomy has enabled the discovery of LMXB outbursts with optical observations, despite the much higher density of objects of comparable brightness in the sky when compared to X-ray observations.

In Chapter 2, I cover my search for optical outbursts of LMXBs in the Zwicky Transient Facility (ZTF) alert stream. Using a small sample of 5 discovered outbursts during four years of ZTF data, I infer a galactic population consistent with a much larger sample of X-ray discovered LMXBs. The limiting magnitude of a single frame taken by ZTF is around 40 times brighter than a single frame LSST image, while the bi-nightly cadence of ZTF is a quicker than the 3-night cadence of LSST's wide fast deep survey. I look ahead to how increased sensitivity, the survey area, and the cadence of LSST can lead to the discovery of up to 400 LMXB outbursts over the 10 year survey baseline.

In Chapter 3, I use `cogsworth` to simulate a population of 2 million binary systems, which resulted in the formation of a few hundred LMXBs. I then vary the configuration of the binary stellar evolution models used by `COSMIC` to evolve the systems to see how this impacts the number and properties of LMXBs created. I find that some combinations of parameters reproduce the CE bottleneck and result in the creation of many fewer BH LMXBs when compared to NS LMXBs. I also found the simulations to reproduce the brighter end of fluxes, as well as the distribution of systems in galactic latitude. Further work is needed to compare the kicks, companion masses, and orbital periods between the simulations and known systems.

In Chapter 4, I look at the first publicly released Rubin dataset, DP1. I perform a crossmatch between all objects discovered in DP1 and a comprehensive catalog of X-ray sources, which are comparatively less dense and not as well localized when compared to the optical. I demonstrate that outside of fields that are well observed by X-ray observatories with high resolution, such as Chandra, most X-ray sources can be matched to several optical objects in LSST. This means that more sophisticated methods for crossmatching that involve priors for these multiwavelength sources are needed.

It is our hope that the number of LMXBs by discovered by Rubin will augment our existing sample considerably, particularly by increasing our known sample of LMXBs undergoing failed transition outbursts, or are otherwise fainter in the X-rays. By increasing the sample of both systems and outbursts, we may learn more about both the physics of accretion, and also the physics of binary stellar evolution.

BIBLIOGRAPHY

Alabarta, K., Altamirano, D., Méndez, M., et al. 2021, MNRAS, 507, 5507, doi: 10.1093/mnras/stab2241

Archibald, A. M., Stairs, I. H., Ransom, S. M., et al. 2009, Science, 324, 1411, doi: 10.1126/science.1172740

Armas Padilla, M., Wijnands, R., Degenaar, N., et al. 2014, MNRAS, 444, 902, doi: 10.1093/mnras/stu1487

Arur, K., & Maccarone, T. 2017, in American Astronomical Society Meeting Abstracts, Vol. 229, American Astronomical Society Meeting Abstracts #229, 344.05

Astropy Collaboration, Robitaille, T. P., Tollerud, E. J., et al. 2013, A&A, 558, A33, doi: 10.1051/0004-6361/201322068

Astropy Collaboration, Price-Whelan, A. M., Sipőcz, B. M., et al. 2018, AJ, 156, 123, doi: 10.3847/1538-3881/aabc4f

Astropy Collaboration, Price-Whelan, A. M., Lim, P. L., et al. 2022, ApJ, 935, 167, doi: 10.3847/1538-4357/ac7c74

Avakyan, A., Neumann, M., Zainab, A., et al. 2023, arXiv e-prints, arXiv:2303.16168, doi: 10.48550/arXiv.2303.16168

Baglio, M. C., Saikia, P., Russell, D. M., et al. 2022, The Astrophysical Journal, 930, 20, doi: 10.3847/1538-4357/ac63ad

Bahramian, A., & Degenaar, N. 2022, arXiv e-prints, arXiv:2206.10053, doi: 10.48550/arXiv.2206.10053

Bailer-Jones, C. A. L., Rybizki, J., Fouesneau, M., Demleitner, M., & Andrae, R. 2021, AJ, 161, 147, doi: 10.3847/1538-3881/abd806

Balbus, S. A., & Hawley, J. F. 1991, ApJ, 376, 214, doi: 10.1086/170270

—. 1998, Reviews of Modern Physics, 70, 1, doi: 10.1103/RevModPhys.70.1

Behnel, S., Bradshaw, R., Citro, C., et al. 2011, Computing in Science Engineering, 13, 31, doi: 10.1109/MCSE.2010.118

Belczynski, K., Kalogera, V., Rasio, F. A., et al. 2008, ApJS, 174, 223, doi: 10.1086/521026

Bellm, E. C. 2016, PASP, 128, 084501, doi: 10.1088/1538-3873/128/966/084501

—. 2021a, The Astronomer's Telegram, 14372, 1

—. 2021b, The Astronomer's Telegram, 14539, 1

—. Priv. Communication, Private communication/Email, Private communication

Bellm, E. C., Kulkarni, S. R., Graham, M. J., et al. 2019a, PASP, 131, 018002, doi: 10.1088/1538-3873/aaecbe

Bellm, E. C., Kulkarni, S. R., Barlow, T., et al. 2019b, PASP, 131, 068003, doi: 10.1088/1538-3873/ab0c2a

Bellm, E. C., Wang, Y., van Roestel, J., et al. 2023, ApJ, 956, 21, doi: 10.3847/1538-4357/acf37c

Bernardini, F., Russell, D. M., Shaw, A. W., et al. 2016, ApJ, 818, L5, doi: 10.3847/2041-8205/818/1/L5

Bhattacharya, D., & van den Heuvel, E. P. J. 1991, Phys. Rep., 203, 1, doi: 10.1016/0370-1573(91)90064-S

Bianco, F. B., Ivezić, Ž., Jones, R. L., et al. 2022, ApJS, 258, 1, doi: 10.3847/1538-4365/ac3e72

Blum, R., & the Rubin Operations Team. 2020, Vera C. Rubin Observatory Data Policy, Data Management Operations Controlled Document RDO-013, Vera C. Rubin Observatory. https://ls.st/RDO-013

Boller, T., Freyberg, M. J., Trümper, J., et al. 2016, A&A, 588, A103

Breivik, K., Coughlin, S., Zevin, M., et al. 2020, ApJ, 898, 71, doi: 10.3847/1538-4357/ab9d85

Budavári, T., & Basu, A. 2016, AJ, 152, 86

Budavári, T., & Szalay, A. S. 2008, ApJ, 679, 301

Bykov, S. D., Belvedersky, M. I., & Gilfanov, M. R. 2022, Astronomy Letters, 48, 653, doi: 10.1134/S1063773722110044

Caplar, N., Beebe, W., Branton, D., et al. 2025, arXiv e-prints, arXiv:2501.02103, doi: 10.48550/arXiv.2501.02103

Casares, J. 2016, ApJ, 822, 99, doi: 10.3847/0004-637X/822/2/99

—. 2018, MNRAS, 473, 5195, doi: 10.1093/mnras/stx2690

Casares, J., & Jonker, P. G. 2014, Space Sci. Rev., 183, 223, doi: 10.1007/s11214-013-0030-6

Casares, J., & Torres, M. A. P. 2018, MNRAS, 481, 4372, doi: 10.1093/mnras/sty2570

Chambers, K. C., Magnier, E. A., Metcalfe, N., et al. 2016, arXiv e-prints, arXiv:1612.05560, doi: 10.48550/arXiv.1612.05560

Charles, P. A., & Coe, M. J. 2003, arXiv e-prints, astro, doi: 10.48550/arXiv.astro-ph/0308020

—. 2006, in Compact stellar X-ray sources, ed. W. H. G. Lewin & M. van der Klis, Vol. 39, 215–265

Chen, W., Shrader, C. R., & Livio, M. 1997, ApJ, 491, 312, doi: 10.1086/304921

Chen, Y., Sun, X., Li, Z., et al. 2022, Appl. Opt., 61, 8813, doi: 10.1364/AO.469433

Choi, Y., Olsen, K. A. G., Carlin, J. L., et al. 2025, arXiv e-prints, arXiv:2507.01343, doi: 10.48550/arXiv.2507.01343

Claeys, J. S. W., Pols, O. R., Izzard, R. G., Vink, J., & Verbunt, F. W. M. 2014, A&A, 563, A83, doi: 10.1051/0004-6361/201322714

Collette, A. 2013, Python and HDF5 (O'Reilly)

Coppejans, D. L., Körding, E. G., Knigge, C., et al. 2016, MNRAS, 456, 4441, doi: 10.1093/mnras/stv2921

Corral-Santana, J. M., Casares, J., Muñoz-Darias, T., et al. 2016, A&A, 587, A61, doi: 10.1051/0004-6361/201527130

Dahiwale, A., & Fremling, C. 2020, Transient Name Server Classification Report, 2020-2302, 1

De Cicco, D., Bauer, F. E., Paolillo, M., et al. 2022, A&A, 664, A117, doi: 10.1051/0004-6361/202142750

de Martino, D., D'Avanzo, P., Ambrosino, F., et al. 2022, The Astronomer's Telegram, 15479, 1

de Mink, S. E., Sana, H., Langer, N., Izzard, R. G., & Schneider, F. R. N. 2014, ApJ, 782, 7, doi: 10.1088/0004-637X/782/1/7

Dekany, R., Smith, R. M., Riddle, R., et al. 2020, PASP, 132, 038001, doi: 10.1088/1538-3873/ab4ca2

di Clemente, A., Giallongo, E., Natali, G., Trevese, D., & Vagnetti, F. 1996, ApJ, 463, 466, doi: 10.1086/177261

Disberg, P., Gaspari, N., & Levan, A. J. 2025, A&A, 700, A75, doi: 10.1051/0004-6361/202554349

Done, C., Gierliński, M., & Kubota, A. 2007, A&A Rev., 15, 1, doi: 10.1007/s00159-007-0006-1

Drake, A. J., Djorgovski, S. G., Mahabal, A., et al. 2009, ApJ, 696, 870, doi: 10.1088/0004-637X/696/1/870

Drake, A. J., Gänsicke, B. T., Djorgovski, S. G., et al. 2014, MNRAS, 441, 1186, doi: 10.1093/mnras/stu639

Dubus, G., Hameury, J. M., & Lasota, J. P. 2001, A&A, 373, 251, doi: 10.1051/0004-6361:20010632

Dubus, G., Lasota, J.-P., Hameury, J.-M., & Charles, P. 1999, Monthly Notices of the Royal Astronomical Society, 303, 139, doi: 10.1046/j.1365-8711.1999.02212.x

Ducci, L., Mereghetti, S., Hryniewicz, K., Santangelo, A., & Romano, P. 2019, A&A, 624, A9, doi: 10.1051/0004-6361/201834390

Duchêne, G., & Kraus, A. 2013, ARA&A, 51, 269, doi: 10.1146/annurev-astro-081710-102602

Duev, D. A., Mahabal, A., Masci, F. J., et al. 2019, MNRAS, 489, 3582, doi: 10.1093/mnras/stz2357

Euclid Collaboration, Roster, W., Salvato, M., et al. 2025, arXiv e-prints, arXiv:2503.15316, doi: 10.48550/arXiv.2503.15316

Evans, I. N., Primini, F. A., Glotfelty, K. J., et al. 2010, ApJS, 189, 37

Evans, I. N., Evans, J. D., Martínez-Galarza, J. R., et al. 2024, ApJS, 274, 22, doi: 10.3847/1538-4365/ad6319

Evans, P. A., Page, K. L., Osborne, J. P., et al. 2020, ApJS, 247, 54, doi: 10.3847/1538-4365/ab7db9

Fagin, J., Chan, J. H.-H., Best, H., et al. 2025, ApJ, 988, 59, doi: 10.3847/1538-4357/addabc

Farr, W. M., Sravan, N., Cantrell, A., et al. 2011, ApJ, 741, 103, doi: 10.1088/0004-637X/741/2/103

Flesch, E. W. 2023, The Open Journal of Astrophysics, 6, 49, doi: 10.21105/astro.2308.01505

Förster, F., Cabrera-Vives, G., Castillo-Navarrete, E., et al. 2021, AJ, 161, 242

Fortin, F., Kalsi, A., García, F., Simaz-Bunzel, A., & Chaty, S. 2024, A&A, 684, A124, doi: 10.1051/0004-6361/202347908

Fryer, C. L., Belczynski, K., Wiktorowicz, G., et al. 2012, ApJ, 749, 91, doi: 10.1088/0004-637X/749/1/91

Gaia Collaboration, Vallenari, A., Brown, A. G. A., et al. 2023, A&A, 674, A1, doi: 10.1051/0004-6361/202243940

Gandhi, P., Rao, A., Charles, P. A., et al. 2020, MNRAS, 496, L22, doi: 10.1093/mnrasl/slaa081

Ginsburg, A., Sipőcz, B. M., Brasseur, C. E., et al. 2019, AJ, 157, 98, doi: 10.3847/1538-3881/aafc33

Goodwin, A. J., Russell, D. M., Galloway, D. K., et al. 2020, MNRAS, 498, 3429, doi: 10.1093/mnras/staa2588

Graham, M. J., Kulkarni, S. R., Bellm, E. C., et al. 2019, PASP, 131, 078001, doi: 10.1088/1538-3873/ab006c

Green, G. M., Schlafly, E., Zucker, C., Speagle, J. S., & Finkbeiner, D. 2019, ApJ, 887, 93, doi: 10.3847/1538-4357/ab5362

Grimm, H.-J., Gilfanov, M., & Sunyaev, R. 2002a, A&A, 391, 923, doi: 10.1051/0004-6361:20020826

Grimm, H. J., Gilfanov, M., & Sunyaev, R. 2002b, A&A, 391, 923, doi: 10.1051/0004-6361:20020826

Guy, L. P., Bechtol, K., Bellm, E., et al. 2025, Rubin Observatory Plans for an Early Science Program, Technical Note RTN-011, Vera C. Rubin Observatory. https://rtn-011.lsst.io/

Gwyn, S. 2024, Mapping Gaia magnitudes to LSST bands, LSST Community Forum. https://community.lsst.org/t/mapping-gaia-magnitudes-to-lsst-bands/8927/2

Haakonsen, C. B., & Rutledge, R. E. 2009, ApJS, 184, 138

Hameury, J. 2020, Advances in Space Research, 66, 1004, doi: https://doi.org/10.1016/j.asr.2019.10.022

Harris, C. R., Millman, K. J., van der Walt, S. J., et al. 2020, Nature, 585, 357, doi: 10.1038/s41586-020-2649-2

Hasinger, G. 2008, A&A, 490, 905, doi: 10.1051/0004-6361:200809839

Heinke, C. O., Bahramian, A., Degenaar, N., & Wijnands, R. 2015, MNRAS, 447, 3034, doi: 10.1093/mnras/stu2652

Heinke, C. O., Zheng, J., Maccarone, T. J., et al. 2025, ApJS, 279, 57, doi: 10.3847/1538-4365/ade99a

Hjellming, M. S., & Webbink, R. F. 1987, ApJ, 318, 794, doi: 10.1086/165412

Holt, S. S., Kaluzienski, L. J., Boldt, E. A., & Serlemitsos, P. J. 1979, ApJ, 233, 344, doi: 10.1086/157395

Hunter, J. D. 2007, Computing in Science and Engineering, 9, 90, doi: 10.1109/MCSE.2007.55

Hurley, J. R., Pols, O. R., & Tout, C. A. 2000, MNRAS, 315, 543, doi: 10.1046/j.1365-8711.2000.03426.x

Hurley, J. R., Tout, C. A., & Pols, O. R. 2002, MNRAS, 329, 897, doi: 10.1046/j.1365-8711.2002.05038.x

Ivanova, N., Justham, S., Chen, X., et al. 2013, A&A Rev., 21, 59, doi: 10.1007/s00159-013-0059-2

Ivezić, Ž., Kahn, S. M., Tyson, J. A., et al. 2019, ApJ, 873, 111, doi: 10.3847/1538-4357/ab042c

John, C., De, K., Lucchini, M., et al. 2024, MNRAS, 535, 2633, doi: 10.1093/mnras/stae2432

Johnson, M. A. C., Gandhi, P., Chapman, A. P., et al. 2019, MNRAS, 484, 19, doi: 10.1093/mnras/sty3466

Jonker, P. G., Bassa, C. G., Nelemans, G., et al. 2011, ApJS, 194, 18, doi: 10.1088/0067-0049/194/2/18

Kaiser, N. 2004, in Society of Photo-Optical Instrumentation Engineers (SPIE) Conference Series, Vol. 5489, Ground-based Telescopes, ed. J. M. Oschmann, Jr., 11–22, doi: 10.1117/12.552472

Kalogera, V., & Webbink, R. F. 1998, ApJ, 493, 351, doi: 10.1086/305085

Kar, A., Ojha, P., & Bhattacharyya, S. 2024, MNRAS, 535, 344, doi: 10.1093/mnras/stae2346

Kato, T., Isogai, K., Hambsch, F.-J., et al. 2017, PASJ, 69, 75, doi: 10.1093/pasj/psx058

Kiel, P. D., & Hurley, J. R. 2006, MNRAS, 369, 1152, doi: 10.1111/j.1365-2966.2006.10400.x

King, A. R. 1998, MNRAS, 296, L45, doi: 10.1046/j.1365-8711.1998.01652.x

—. 2002, MNRAS, 335, L13, doi: 10.1046/j.1365-8711.2002.05745.x

King, A. R., & Ritter, H. 1998, MNRAS, 293, L42, doi: 10.1046/j.1365-8711.1998.01295.x

Klebesadel, R. W., Strong, I. B., & Olson, R. A. 1973, ApJ, 182, L85, doi: 10.1086/181225

Klencki, J., Wiktorowicz, G., Gładysz, W., & Belczynski, K. 2017, MNRAS, 469, 3088, doi: 10.1093/mnras/stx842

Kochanek, C. S., Shappee, B. J., Stanek, K. Z., et al. 2017, PASP, 129, 104502, doi: 10.1088/1538-3873/aa80d9

Krimm, H. A., Holland, S. T., Corbet, R. H. D., et al. 2013, ApJS, 209, 14, doi: 10.1088/0067-0049/209/1/14

Krimm, H. A., Holland, S. T., Corbet, R. H. D., et al. 2013, The Astrophysical Journal Supplement Series, 209, 14, doi: 10.1088/0067-0049/209/1/14

Krimm, H. A., Barthelmy, S. D., Cummings, J. R., et al. 2018, The Astronomer's Telegram, 12151, 1

Kroupa, P. 1995, MNRAS, 277, 1522, doi: 10.1093/mnras/277.4.1522

—. 2001, MNRAS, 322, 231, doi: 10.1046/j.1365-8711.2001.04022.x

Lallement, R., Babusiaux, C., Vergely, J. L., et al. 2019, A&A, 625, A135, doi: 10.1051/0004-6361/201834695

Lasota, J.-P. 2001, New A Rev., 45, 449, doi: 10.1016/S1387-6473(01)00112-9

—. 2023, arXiv e-prints, arXiv:2311.16013, doi: 10.48550/arXiv.2311.16013

Law, N. M., Kulkarni, S. R., Dekany, R. G., et al. 2009, PASP, 121, 1395, doi: 10.1086/648598

Levine, A. M., Bradt, H., Cui, W., et al. 1996, ApJ, 469, L33, doi: 10.1086/310260

Licquia, T. C., & Newman, J. A. 2015, ApJ, 806, 96, doi: 10.1088/0004-637X/806/1/96

Liu, Q. Z., van Paradijs, J., & van den Heuvel, E. P. J. 2007, VizieR Online Data Catalog: Catalogue of Galactic low-mass X-ray binaries (Liu+, 2007), VizieR On-line Data Catalog: J/A+A/469/807. Originally published in: 2007A&A...469..807L, doi: 10.26093/cds/vizier.34690807

Luo, B., Brandt, W. N., Xue, Y. Q., et al. 2017, ApJS, 228, 2, doi: 10.3847/1538-4365/228/1/2

Maccarone, T. J., Gallo, E., & Fender, R. 2003, MNRAS, 345, L19, doi: 10.1046/j.1365-8711.2003.07161.x

Malanchev, K., DeLucchi, M., Caplar, N., et al. 2025, arXiv e-prints, arXiv:2506.23955, doi: 10.48550/arXiv.2506.23955

Martini, P., Stoll, R., Derwent, M. A., et al. 2011, PASP, 123, 187, doi: 10.1086/658357

Masci, F. J., Laher, R. R., Rusholme, B., et al. 2019, PASP, 131, 018003, doi: 10.1088/1538-3873/aae8ac

Matheson, T., Stubens, C., Wolf, N., et al. 2021, AJ, 161, 107

Matsuoka, M., Kawasaki, K., Ueno, S., et al. 2009, PASJ, 61, 999, doi: 10.1093/pasj/61.5.999

Menou, K., Hameury, J.-M., Lasota, J.-P., & Narayan, R. 2000, MNRAS, 314, 498, doi: 10.1046/j.1365-8711.2000.03357.x

Mereminskiy, I., Medvedev, P., Semena, A., et al. 2020, The Astronomer's Telegram, 13571, 1

Merloni, A., Lamer, G., Liu, T., et al. 2024, A&A, 682, A34, doi: 10.1051/0004-6361/202347165

Michaely, E., & Perets, H. B. 2016, MNRAS, 458, 4188, doi: 10.1093/mnras/stw368

Misra, D., Kovlakas, K., Fragos, T., et al. 2023, A&A, 672, A99, doi: 10.1051/0004-6361/202244929

Moe, M., & Di Stefano, R. 2017, ApJS, 230, 15, doi: 10.3847/1538-4365/aa6fb6

Möller, A., Peloton, J., Ishida, E. E. O., et al. 2021, MNRAS, 501, 3272

Nagarajan, P., & El-Badry, K. 2025, PASP, 137, 034203, doi: 10.1088/1538-3873/adb6d6

Naoz, S., Fragos, T., Geller, A., Stephan, A. P., & Rasio, F. A. 2016, ApJ, 822, L24, doi: 10.3847/2041-8205/822/2/L24

Negoro, H., Iwakiri, W., Kawakubo, Y., et al. 2022, The Astronomer's Telegram, 15440, 1

Neijssel, C. J., Vigna-Gómez, A., Stevenson, S., et al. 2019, MNRAS, 490, 3740, doi: 10.1093/mnras/stz2840

Neilsen, J., & Degenaar, N. 2023, arXiv e-prints, arXiv:2304.05412

Niwano, M., Murata, K. L., Ito, N., Yatsu, Y., & Kawai, N. 2023, MNRAS, 525, 4358, doi: 10.1093/mnras/stad2561

Nordin, J., Brinnel, V., van Santen, J., et al. 2019, arXiv e-prints

NSF-DOE Vera C. Rubin Observatory. 2025a, The Vera C. Rubin Observatory Data Preview 1, doi: 10.71929/rubin/2570536

—. 2025b, Legacy Survey of Space and Time Data Preview 1: object dataset type [Data set], NSF-DOE Vera C. Rubin Observatory, doi: 10.71929/RUBIN/2570324

—. 2025c, Legacy Survey of Space and Time Data Preview 1: deep_coadd dataset type, NSF-DOE Vera C. Rubin Observatory, doi: 10.71929/RUBIN/2570313

—. 2025d, Legacy Survey of Space and Time Data Preview 1: visit_image dataset type [Data set], NSF-DOE Vera C. Rubin Observatory, doi: 10.71929/RUBIN/2570311

—. 2025e, Legacy Survey of Space and Time Data Preview 1: object_forced_source dataset type [Data set], NSF-DOE Vera C. Rubin Observatory, doi: 10.71929/RUBIN/2570326

—. 2025f, Legacy Survey of Space and Time Data Preview 1: difference_image dataset type [Data set], NSF-DOE Vera C. Rubin Observatory, doi: 10.71929/RUBIN/2570312

—. 2025g, Legacy Survey of Space and Time Data Preview 1: dia_source dataset type [Data set], NSF-DOE Vera C. Rubin Observatory, doi: 10.71929/RUBIN/2570316

—. 2025h, Legacy Survey of Space and Time Data Preview 1: dia_object dataset type [Data set], NSF-DOE Vera C. Rubin Observatory, doi: 10.71929/RUBIN/2570318

—. 2025i, Legacy Survey of Space and Time Data Preview 1: dia_object_forced_source dataset type [Data set], NSF-DOE Vera C. Rubin Observatory, doi: 10.71929/RUBIN/2570320

Offner, S. S. R., Moe, M., Kratter, K. M., et al. 2023, in Astronomical Society of the Pacific Conference Series, Vol. 534, Protostars and Planets VII, ed. S. Inutsuka, Y. Aikawa, T. Muto, K. Tomida, & M. Tamura, 275, doi: 10.48550/arXiv.2203.10066

Oliva, G. A., & Kuiper, R. 2020, A&A, 644, A41, doi: 10.1051/0004-6361/202038103

Papitto, A., & de Martino, D. 2022, in Astrophysics and Space Science Library, Vol. 465, Astrophysics and Space Science Library, ed. S. Bhattacharyya, A. Papitto, & D. Bhattacharya, 157–200, doi: 10.1007/978-3-030-85198-9_6

Papitto, A., Ferrigno, C., Bozzo, E., et al. 2013, Nature, 501, 517, doi: 10.1038/nature12470

Patterson, M. T., Bellm, E. C., Rusholme, B., et al. 2019, PASP, 131, 018001

Pfahl, E., Rappaport, S., & Podsiadlowski, P. 2002, ApJ, 573, 283, doi: 10.1086/340494

Pirbhoy, S. F., Baglio, M. C., Russell, D. M., et al. 2020, The Astronomer's Telegram, 13451, 1

Podsiadlowski, P., Joss, P. C., & Hsu, J. J. L. 1992, ApJ, 391, 246, doi: 10.1086/171341

Podsiadlowski, P., Rappaport, S., & Han, Z. 2003, MNRAS, 341, 385, doi: 10.1046/j.1365-8711.2003.06464.x

Postnov, K. A., & Yungelson, L. R. 2014, Living Reviews in Relativity, 17, 3, doi: 10.12942/lrr-2014-3

Price-Whelan, A. M. 2017, The Journal of Open Source Software, 2, doi: 10.21105/joss.00388

Price-Whelan, A. M., & Foreman-Mackey, D. 2017, The Journal of Open Source Software, 2, doi: 10.21105/joss.00357

Priedhorsky, W. C., & Holt, S. S. 1987, Space Sci. Rev., 45, 291, doi: 10.1007/BF00171997

Priedhorsky, W. C., & Verbunt, F. 1988, ApJ, 333, 895, doi: 10.1086/166798

Rau, A., Nardini, M., & Greiner, J. 2012, The Astronomer's Telegram, 4054, 1

Rau, A., Kulkarni, S. R., Law, N. M., et al. 2009, PASP, 121, 1334, doi: 10.1086/605911

Reig, P., & Fabregat, J. 2015, A&A, 574, A33, doi: 10.1051/0004-6361/201425008

Remillard, R. A., & McClintock, J. E. 2006, ARA&A, 44, 49, doi: 10.1146/annurev.astro.44.051905.092532

Repetto, S., Igoshev, A. P., & Nelemans, G. 2017, MNRAS, 467, 298, doi: 10.1093/mnras/stx027

Reuter, M. A., Cook, K. H., Delgado, F., Petry, C. E., & Ridgway, S. T. 2016, in Society of Photo-Optical Instrumentation Engineers (SPIE) Conference Series, Vol. 9911, Modeling, Systems Engineering, and Project Management for Astronomy VI, ed. G. Z. Angeli & P. Dierickx, 991125, doi: 10.1117/12.2232680

Richter, G. A. 1975, Astronomische Nachrichten, 296, 65, doi: 10.1002/asna.19752960203

Ritter, H., & Kolb, U. 2003a, A&A, 404, 301, doi: 10.1051/0004-6361:20030330

—. 2003b, A&A, 404, 301, doi: 10.1051/0004-6361:20030330

Rodriguez, A. C. 2024, PASP, 136, 054201, doi: 10.1088/1538-3873/ad357c

Russell, D. M., Fender, R. P., Hynes, R. I., et al. 2006, MNRAS, 371, 1334, doi: 10.1111/j.1365-2966.2006.10756.x

Russell, D. M., Bramich, D. M., Lewis, F., et al. 2019, Astronomische Nachrichten, 340, 278, doi: 10.1002/asna.201913610

Rutledge, R. E., Brunner, R. J., Prince, T. A., & Lonsdale, C. 2000, ApJS, 131, 335

Saikia, P., Russell, D. M., Pirbhoy, S. F., et al. 2023, The Astrophysical Journal, 949, 104, doi: 10.3847/1538-4357/acc8cc

Salvato, M., Buchner, J., Budavári, T., et al. 2018, MNRAS, 473, 4937, doi: 10.1093/mnras/stx2651

Sana, H., de Mink, S. E., de Koter, A., et al. 2012, Science, 337, 444, doi: 10.1126/science.1223344

Sanders, J. L., & Binney, J. 2015, MNRAS, 449, 3479, doi: 10.1093/mnras/stv578

Sanna, A., Bult, P., Ng, M., et al. 2022, MNRAS, 516, L76, doi: 10.1093/mnrasl/slac093

Saxton, R. D., Read, A. M., Esquej, P., et al. 2008, A&A, 480, 611, doi: 10.1051/0004-6361:20079193

Shahbaz, T., Russell, D. M., Zurita, C., et al. 2013, MNRAS, 434, 2696, doi: 10.1093/mnras/stt1212

Shakura, N. I., & Sunyaev, R. A. 1973, A&A, 24, 337

Shao, Y., & Li, X.-D. 2020, ApJ, 898, 143, doi: 10.3847/1538-4357/aba118

Shi, X., Budavári, T., & Basu, A. 2019, ApJ, 870, 51

Shidatsu, M., Negoro, H., Nakajima, M., et al. 2019, The Astronomer's Telegram, 13097, 1

Siegel, J. C., Kiato, I., Kalogera, V., et al. 2023, ApJ, 954, 212, doi: 10.3847/1538-4357/ace9d9

Smith, K. W., Williams, R. D., Young, D. R., et al. 2019, Research Notes of the American Astronomical Society, 3, 26

Spergel, D., Gehrels, N., Baltay, C., et al. 2015, arXiv e-prints, arXiv:1503.03757, doi: 10.48550/arXiv.1503.03757

Stappers, B. W., Archibald, A. M., Hessels, J. W. T., et al. 2014, ApJ, 790, 39, doi: 10.1088/0004-637X/790/1/39

Stetson, P. B. 1996, PASP, 108, 851, doi: 10.1086/133808

Sutherland, W., & Saunders, W. 1992, MNRAS, 259, 413, doi: 10.1093/mnras/259.3.413

Tauris, T. M., & van den Heuvel, E. P. J. 2006, in Compact stellar X-ray sources, ed. W. H. G. Lewin & M. van der Klis, Vol. 39, 623–665, doi: 10.48550/arXiv.astro-ph/0303456

Tetarenko, A. J., Casella, P., Miller-Jones, J. C. A., et al. 2021, MNRAS, 504, 3862, doi: 10.1093/mnras/stab820

Tetarenko, B., Dubus, G., Lasota, J.-P., Heinke, C., & Sivakoff, G. 2018, Monthly Notices of the Royal Astronomical Society, 480, 2, doi: 10.1093/mnras/sty1798

Tetarenko, B. E., Lasota, J. P., Heinke, C. O., Dubus, G., & Sivakoff, G. R. 2018, Nature, 554, 69, doi: 10.1038/nature25159

Tetarenko, B. E., Sivakoff, G. R., Heinke, C. O., & Gladstone, J. C. 2016, ApJS, 222, 15, doi: 10.3847/0067-0049/222/2/15

The Rubin Observatory Survey Cadence Optimization Committee. 2023, Survey Cadence Optimization Committee's Phase 2 Recommendations, ls.st/PSTN-055

Tonry, J., Denneau, L., Heinze, A., et al. 2019, Transient Name Server Discovery Report, 2019-2553, 1

Tonry, J. L., Denneau, L., Heinze, A. N., et al. 2018, PASP, 130, 064505, doi: 10.1088/1538-3873/aabadf

Tucker, M. A., Shappee, B. J., Holoien, T. W. S., et al. 2018, ApJ, 867, L9, doi: 10.3847/2041-8213/aae88a

van Paradijs, J., & McClintock, J. E. 1995, in X-ray Binaries, ed. W. H. G. Lewin, J. van Paradijs, & E. P. J. van den Heuvel, 58–125

Van Rossum, G., & Drake, F. L. 2009, Python 3 Reference Manual (Scotts Valley, CA: CreateSpace)

Vink, J. S., & de Koter, A. 2005, A&A, 442, 587, doi: 10.1051/0004-6361:20052862

Vink, J. S., de Koter, A., & Lamers, H. J. G. L. M. 2001, A&A, 369, 574, doi: 10.1051/0004-6361:20010127

Virtanen, P., Gommers, R., Oliphant, T. E., et al. 2020, Nature Methods, 17, 261, doi: 10.1038/s41592-019-0686-2

Wagg, T., Breivik, K., Renzo, M., & Price-Whelan, A. 2025a, The Journal of Open Source Software, 10, 7400, doi: 10.21105/joss.07400

Wagg, T., Breivik, K., Renzo, M., & Price-Whelan, A. M. 2025b, ApJS, 276, 16, doi: 10.3847/1538-4365/ad8b1f

Wagg, T., Broekgaarden, F., Van-Lane, P., Wu, K., & Gültekin, K. 2025, TomWagg/software-citation-station: v1.4, v1.4, Zenodo, doi: 10.5281/zenodo.17654855

Wagg, T., & Broekgaarden, F. S. 2024, arXiv e-prints, arXiv:2406.04405. https://arxiv.org/abs/2406.04405

Wagg, T., Broekgaarden, F. S., de Mink, S. E., et al. 2022, ApJ, 937, 118, doi: 10.3847/1538-4357/ac8675

Wainer, T. M., Davenport, J. R. A., Bellm, E. C., et al. 2025, arXiv e-prints, arXiv:2507.03228, doi: 10.48550/arXiv.2507.03228

Wang, C., Jia, K., & Li, X.-D. 2016, MNRAS, 457, 1015, doi: 10.1093/mnras/stw101

Wang, Y. 2026, ykwang1/DP1_Xray_public: Optical Counterparts to X-ray sources in LSST DP1 (rev. 1), v1.1, Zenodo, doi: 10.5281/zenodo.18665437

Wang, Y., & Bellm, E. C. 2022, The Astronomer's Telegram, 15600, 1

Wang, Y., Bellm, E. C., Crossland, A., et al. 2024, ApJ, 962, 91, doi: 10.3847/1538-4357/ad0fe4

Wang, Y., Bellm, E. C., & Jaodand, A. 2022, The Astronomer's Telegram, 15455, 1

Wang, Y. D., Bellm, E. C., Hynes, R. I., et al. 2026, ApJS, 284, 13, doi: 10.3847/1538-4365/ae5247

Warwick, R. S., Saxton, R. D., & Read, A. M. 2012, A&A, 548, A99

Waskom, M. L. 2021, Journal of Open Source Software, 6, 3021, doi: 10.21105/joss.03021

Webb, N. A., Coriat, M., Traulsen, I., et al. 2020a, A&A, 641, A136

—. 2020b, A&A, 641, A136, doi: 10.1051/0004-6361/201937353

Wenger, M., Ochsenbein, F., Egret, D., et al. 2000, A&AS, 143, 9, doi: 10.1051/aas:2000332

Wes McKinney. 2010, in Proceedings of the 9th Python in Science Conference, ed. Stéfan van der Walt & Jarrod Millman, 56 – 61, doi: 10.25080/Majora-92bf1922-00a

Wevers, T., Hodgkin, S. T., Jonker, P. G., et al. 2016, MNRAS, 458, 4530, doi: 10.1093/mnras/stw643

Wiktorowicz, G., Wyrzykowski, Ł., Chruslinska, M., et al. 2019, ApJ, 885, 1, doi: 10.3847/1538-4357/ab45e6

Yao, Y., Kulkarni, S. R., Burdge, K. B., et al. 2021, ApJ, 920, 120, doi: 10.3847/1538-4357/ac15f9

York, D. G., Adelman, J., Anderson, Jr., J. E., et al. 2000, AJ, 120, 1579, doi: 10.1086/301513

Yuan, W., Zhang, C., Chen, Y., & Ling, Z. 2022, in Handbook of X-ray and Gamma-ray Astrophysics, ed. C. Bambi & A. Sangangelo, 86, doi: 10.1007/978-981-16-4544-0_151-1

Yuan, W., Zhang, C., Feng, H., et al. 2015, arXiv e-prints, arXiv:1506.07735, doi: 10.48550/arXiv.1506.07735

Yungelson, L. R., & Lasota, J.-P. 2008, A&A, 488, 257, doi: 10.1051/0004-6361:200809684

Zhao, Y., Gandhi, P., Dashwood Brown, C., et al. 2023, MNRAS, 525, 1498, doi: 10.1093/mnras/stad2226